12-2017

Skeletal Biomechanics and Response to Mechanical Load: A Comparative Approach in the Mouse and Chukar Partridge

Kari A. Verner
Purdue University

Recommended Citation

Verner, Kari A., "Skeletal Biomechanics and Response to Mechanical Load: A Comparative Approach in the Mouse and Chukar Partridge" (2017). *Open Access Dissertations*. 1651.
https://docs.lib.purdue.edu/open_access_dissertations/1651

SKELETAL BIOMECHANICS AND RESPONSE TO MECHANICAL LOAD: A COMPARATIVE APPROACH IN THE MOUSE AND CHUKAR PARTRIDGE

by

Kari A Verner

A Dissertation

Submitted to the Faculty of Purdue University

In Partial Fulfillment of the Requirements for the degree of

Doctor of Philosophy

Weldon School of Biomedical Engineering
West Lafayette, Indiana
December 2017

THE PURDUE UNIVERSITY GRADUATE SCHOOL
STATEMENT OF COMMITTEE APPROVAL

Dr. Russell Main, Chair
    Department of Basic Medical Sciences
Dr. Eric Nauman
    Weldon School of Biomedical Engineering
Dr. Matthew Allen
    Indiana University School of Medicine
Dr. Sarah Calve
    Weldon School of Biomedical Engineering
Dr. Joseph Wallace
    Weldon School of Biomedical Engineering

Approved by:
    Dr. George Wodicka
        Head of the Graduate Program

To the little bay Arabian mare who inspired me to go on this crazy journey, Aleena Baskin.

ACKNOWLEDGMENTS

Foremost, I would like to express gratitude to my adviser Dr. Russell Main for taking a chance on an undergraduate student from across the country for what started as a summer research program, and now five years later has resulted in this dissertation. Thank you for your continued support, guidance, and training throughout this experience.

I would also like to thank my committee members: Dr. Eric Nauman, Dr. Sarah Calve, Dr. Matthew Allen, and Dr. Joseph Wallace. Through stimulating courses, insightful comments on my work and encouragement throughout, each of you has helped to make me a better biomedical engineer.

To the lab members of the PMBAM lab, past and present, thank you. You all have helped to shape my work and my graduate school experience as a whole in a positive way, and I will forever appreciate the comradery you provided on a daily basis.

My sincere thanks also goes to Dr. Scott Prahl and Dr. Cynthia Gregory, as well as the entire team at OMLC and OBEI, who provided me an opportunity to join them as an intern, and graciously trained and supported a young engineer interested in science. Those positive experiences encouraged me to continue pursuing the path that has led to this point.

To my parents, Daryl and Barb Jenson, thank you for supporting my crazy idea to move across the country and get a Ph.D. Your moral and emotional support throughout this experience has been unending, and for that I am so grateful.

And finally, to the guy I met on day 1 of my journey here at Purdue and now get to call my husband, Ryan. Your endless love and support have gotten me through the good and bad times of this crazy journey. I’m so excited to see how our path continues as the Drs. Verner!

TABLE OF CONTENTS

LIST OF TABLES

LIST OF FIGURES

ABSTRACT

Author: Verner, Kari, A. PhD
Institution: Purdue University
Degree Received: December 2017
Title: Skeletal Biomechanics and Response to Mechanical Load: A Comparative Approach in the Mouse and Chukar Partridge
Major Professor: Russell Main

Dynamic mechanical loading plays an important role in regulating bone geometry and strength. A healthy skeleton adapts to the bone tissue strain profile and magnitude of loads it experiences on a daily basis in order to maintain reasonable safety factors. In skeletal diseases, such as osteoporosis, a bone's ability to adapt and maintain structural integrity in response to increased mechanical strains is apparently impaired, which allows skeletal resorption to progress unabated and could eventually lead to mechanical failure. In order to develop better treatments for bone wasting diseases, it is important to understand the mechanobiology of how the healthy skeleton responds to mechanical load. The non-invasive, axial compressive murine tibial loading model has been used extensively to study skeletal adaptation, but sole use of rodent models propagates a large gap in understanding skeletal sensitivity and response to load across terrestrial vertebrate groups. The avian skeleton exhibits several features that make it unique compared to the mammalian rodent skeleton, and these differences could affect how the avian skeleton responds to mechanical load relative to the rodent skeleton.

To begin expanding our understanding of skeletal sensitivity across vertebrate species, we developed a novel non-invasive avian tibiotarsal (TBT) loading model using the chukar partridge to complement the use of the murine tibial loading model. For both the mouse and the bird, relatively similar increases in strain stimuli via experimentally applied loads were determined through a combination of *in vivo* strain gauging and finite element models. The cross-sectional strain distributions during locomotion and experimental loading were further characterized in the bird TBT after validating the use of planar strain theory for cortical bone loaded in bending. In response to several weeks of experimentally applied loading, the mouse tibia adapted its geometry and mass. In contrast, the birds adapted their cross-sectional geometry without complementary increases in bone mass while suppressing normal endocortical bone growth. Lastly, in order to study cortical bone's response to mechanical load without the potentially confounding effects of varied systemic factors across species, we developed a novel isolated cortical bone culture model that can be mechanically loaded *in vitro*. We validated that osteocytes in a murine tibial bone segment maintained adequate survival over a five day culture period, and comprehensively characterized the load induced strain profile. Overall, this work takes novel steps to develop and validate comparative *in vivo* and *in vitro* models for comparatively assessing skeletal sensitivity across terrestrial vertebrate species. Continued work in this direction will enhance our understanding of how a healthy skeleton is regulated to maintain adequate bone strength.

1. INTRODUCTION

The skeleton is a fascinating mechanical structure that has the ability to adapt its bone-specific architecture to optimize structure for daily function, and it can also repair itself when mechanical failure does occur. Although bone's ability to adapt to mechanical loads was identified over a hundred years ago [1], theories regarding the necessary stimuli and the cellular and genetic mechanisms responsible for controlling bone mass and quality properties are continuously updated as researchers learn more through studies employing animal models and experimentally applied mechanical loading techniques. While many rules for bone adaptation have been suggested [2-6], the molecular and cellular pathways capable of coordinating whole-bone changes in mass and morphology are still not completely understood.

1.1 Basic Bone Biology

Bone is a multiscale material with functions beyond providing mechanical support to the body. Two types of bone exist: cortical bone, which is the dense outer shell of all bones and carries the majority of a load, and cancellous bone, which is primarily found in the marrow cavity of the epiphyses and metaphyses of long bones and in all vertebrae, and is comprised of a 'sponge-like' network of individual trabeculae that act to redirect load to the surrounding cortical shell. Cortical bone is composed of a Haversian system, also called osteons, often containing vascular channels, surrounded by concentric layers of lamellae that look similar to tree rings. Cancellous bone is composed of hemi-osteons surrounded by lamellae. While most bone deposited after skeletal maturity under normal conditions is lamellar, rapidly forming and highly disorganized woven bone is created for quick repair of fracture or in response to inflammation, as well as during growth for many mammals and birds. Compositionally, bone is 65% mineral, 25% organic, and 10% water, and these proportions are highly related to the entire bone's specific mechanical behavior [1]. Bone's other functions include hematopoiesis, mineral exchange, and as an endocrine organ mediating phosphate and energy metabolism.

Bone possesses three primary cell types, osteoclasts, osteoblasts, and osteocytes, which are activated to perform either bone modeling or remodeling. Osteoclasts are recognized by their multi-nucleation and are primarily involved in mineralized bone resorption, which is essential for bone modeling and remodeling. They undergo apoptosis when bone resorption is complete. Osteoblasts originate from mesenchymal progenitors likely activated by either bone matrix proteins or the Wnt signaling pathway [2] and are responsible for bone formation through bone matrix protein secretion and bone mineralization. As newly mineralized bone is laid down, some osteoblasts become embedded into the new bone matrix and further differentiate into osteocytes. The remaining osteoblasts either become bone lining cells or die by apoptosis. Osteocytes are the most abundant cells in bone and are distributed regularly throughout mineralized bone. Osteocytes, encased in small fluid-filled spaces called lacunae, exhibit dendritic processes that extend out from the cell body through microscopic fluid-filled canals that connect lacunae called canaliculi, creating a lacunar-canalicular network that extends throughout the entire bone volume. It is currently believed that interstitial fluid flow through the lacunar-canalicular network leads to mechanical load-induced pressure gradients in the bone matrix makes which acts as a stimulus to osteocytes[3]. The network of osteocytes throughout the bone matrix makes them ideal mechanosensory cells capable of sensing not only mechanical load, but also damage, and then signaling for the appropriate response [4]. Bone modeling occurs in order to shape bone or increase bone mass and can occur on periosteal, endosteal, or trabecular bone surfaces. Modeling can be either formative through osteoblasts, or resorptive through osteoclasts. Bone remodeling is activated in order to renew bone and can occur intracortically, as well as on periosteal, endosteal, and trabecular surfaces. Remodeling requires osteoclasts and osteoblasts to work together in what are known as bone multicellular units; osteoclasts resorb bone followed by osteoblast-mediated new bone formation at the same location. Bone adaptation involves a precise combination of formative/resorptive modeling and remodeling to achieve the resulting gross changes in morphology.

1.2 Skeletal Disease

Several factors can reduce bone’s ability to adapt and maintain structural integrity in response to increased mechanical strains, which allows skeletal resorption to progress unabated and could eventually lead to mechanical failure. Skeletal diseases can be characterized by decreased bone quality and quantity resulting from poor regulation of skeletal metabolism. Bone health is extremely dependent on adequate bone turnover because modeling and remodeling aid in mineral metabolism, renew the skeleton by repairing micro-damage, and more generally maintain adequate bone strength to resist daily loading events. If bone turnover rates are insufficient, micro-cracks could accumulate over time and eventually coalesce to form a more serious fracture. Conversely, if bone turnover rates are too high, bone volume will slowly decrease due to the negative bone balance that occurs during remodeling. Osteoporosis is the most common bone metabolic disorder. The National Institutes of Health Consensus Development Panel on Osteoporosis defines it as “a skeletal disorder characterized by compromised bone strength predisposing the skeleton to an increased risk of fracture [5].” It is clinically characterized by a gradual reduction over time of bone mineral density and bone mass due to imbalanced bone modeling/remodeling. Although some degree of bone loss is expected with age, decreases in bone mineral density (BMD) greater than even one standard deviation below the young adult reference mean significantly increases a person’s chance for sustaining fragility fractures. There is not a single known cause for osteoporosis, and risk factors range from age, race, and genetic factors, to lifestyle choices [6]. In the year 2000, the panel reported that 10 million people had already been diagnosed with osteoporosis, and 18 million were osteopenic, which puts them at high risk for developing osteoporosis [5]. Approximately $10-15 billion dollars are spent annually on in-patient treatment alone for osteoporotic fractures, which most commonly occur at cortico-cancellous sites such as the femoral head, vertebrae, and distal radius [7]. While postmenopausal women are the most common sufferers of this disorder, the condition of osteoporosis also affects men [8], astronauts in conditions of microgravity [9, 10], and patients on long-term bed rest or with paralysis [11, 12].

The second most common skeletal disease is Paget disease of bone (PDB) [13]. This disease typically affects older adults and is characterized by focal lesions with increased coupled osteoclastic and osteoblastic activity that can present in any bone. The lesions most commonly cause pain, but depending on their location can also lead to bone deformities, gait abnormalities, neurologic symptoms, or increased incidence of fracture. The precise cause of PDB is unknown, although several studies have suggested involvement of certain genetic mutations [14] and environmental factors [15].

There are currently no treatments that can cure osteoporosis, PDB, or other bone turnover-related diseases. Nutritional supplementation of calcium and vitamin D to insure adequate availability in the body is typically the first intervention [16]. Pharmacologic treatments include anti-catabolic and anabolic drugs that, in general, aim to directly affect the bone remodeling process. Anti-catabolic drugs, such as bisphosphonates, estrogen, and selective estrogen receptor modulators (SERMS), have been used most frequently [17-21]. Anti-catabolic treatments act to inhibit osteoclast activity or formation to suppress remodeling and further bone loss. There is only one FDA-approved anabolic pharmacological treatment currently available, teriparatide, which has an identical amino acid sequence to endogenous PTH, and can therefore bind to the same receptor, stimulating bone apposition without bone resorption [22]. Although several current treatments exist and have shown to successfully decrease fracture incidence, the majority aim to prevent further bone loss but cannot return bone to a pre-disease state, and often carry negative side effects.

Since bone quality maintenance is so important for skeletal health, understanding how modeling and remodeling are activated and controlled is critical for developing treatments that aim to restore proper balance and prevent further bone degradation. Since one of the skeleton’s primary functions is to serve as the load bearing mechanical structure for the body, loss of skeletal integrity can lead to rapid decrease in quality of life. The forces perceived by the skeleton act as inputs to which this highly dynamic organ regulates its strength appropriately. By assessing the tissue-, transcriptomic-, and cellular-level skeletal response to experimentally applied mechanical load, we gain insight into how the skeleton is naturally regulated, which can then inform how we can potentially modulate it during states of disease when normal osteoregulation is unsuccessful.

1.3 Characterizing a Bone’s Mechanical Environment

It was initially proposed that bone’s adaptive response is directly related to the mechanical forces it experiences on a daily basis [23]. Therefore, a major continuous effort exists to characterize the loads and strains experienced by a bone so that they may be related to the identified adaptive effects. Understanding the stimulus is critical to evaluating skeletal sensitivity as well.

The most direct method used to assess how mechanical forces are transmitted through a bone is to measure bone strain by surgically attaching strain gauges to bone surfaces. The strain gauge method involves surgically exposing suitable bone surface(s) and attaching wired strain gauge(s). Strain gauges measure the resulting deformation of a bone when it is loaded and can provide real-time, *in vivo* information about a bone surface's mechanical environment at the location of the gauge throughout a subject's gait or load cycle. This method has been used to characterize the physiological strain environment in a wide variety of animals including, but not limited to, turkeys [24], chicks [25], horses [26, 27], sheep [28], dogs [29], rats [30], and mice [31]. Eventually, it was recognized that peak strains during rigorous locomotion are similar (-2000 to -3000 με) for all species and a variety of bones studied [32]. While loading events engendering peak strains typically occur only a few times each day, low magnitude loading events occur constantly throughout the day [33]**.** These findings suggest that limb bones as whole structures are designed to maintain similar safety factors across species.

Strain gauges have also been used to determine the necessary loads to induce specific bone strains during artificial loading, a technique that is used frequently in studies. Despite the enormous benefits strain gauges provide to the field, a few considerations and limitations must be recognized. Since the gauges are attached surgically, there is always a possibility for post-operative lameness, and the wires must be contained under the skin and exit at some point to connect to external equipment. Both could affect the subject's gait and the resulting strain, but these issues would be less critical when load is applied artificially through a mechanical apparatus. The largest limitation is that each gauge can only provide strain information for the surface area to which it is attached. While it is recognized that three rosette strain gauges spaced equally around a cross section of bone can adequately characterize the local strain environment at that level of the bone [24, 26], the number and type of gauge(s) that can be used is dependent on the bone surface and size at the location of interest. For instance, the mouse tibia is used frequently for adaptation studies, but only one single element gauge can be placed *in vivo* on the medial midshaft due to the small bone size and shape [34].

1.4 Computational Modeling Approach to Characterizing Bone Strains

Finite element analysis (FEA), while strictly a computational technique, offers the unique capability of predicting a variety of parameters such as stress and strain throughout the entire bone, including the endocortical surface and cancellous bone volumes [35]. This technique may, in fact, be the only method capable of suggesting the possible strain environment for cancellous bone since non-invasive, *in vivo* strain measurements are not currently possible. Development of the computer model has advanced from projecting an image of the bone and digitizing the bone's surfaces using a stylus [36] to reconstructing high resolution microcomputed tomography (μCT) images of the bone via computer programs to create very accurate three dimensional models [35, 37-39]. Models can be validated by comparing *in vivo* strain measurements to model-predicted strain values at the gauge site(s) of the same specimen. The level of validation is dependent on the amount of strain information gathered *in vivo*. The size of the mouse tibia, for instance, limits *in vivo* strain data to one single element gauge, yet measured strains at that gauge correlated closely to the FE-calculated peak strains in the midshaft cortical bone [39]. The well-defined load-application points of the functionally-isolated ulnar loading technique [36] and the four-point bending technique [40] are ideal for defining load and boundary conditions in FEMs, but by iteratively adjusting the load and boundary conditions and validating the results with *in vivo* strain measurements, the conditions of axial loading techniques can be approximated successfully [38]. Many models have assumed homogenous values of Young's Modulus and Poisson's Ratio, values characterizing the stiffness and elasticity, respectively, of a material, although heterogeneity of tissue mechanical properties has been shown to have the largest (positive) effect on the predicted cancellous strain environment [39]. The ability to characterize whole bone tissue-level strain will allow comparisons between patterns of bone formation and resorption and the local strain environment at cortical and cancellous bone sites [41, 42].

1.5 Experimental Models of Skeletal Adaption

Determining the sensitivity and multi-scale response of the skeleton to mechanical load stimuli is important to understanding how the mechanobiology naturally maintains bone quality, and how it could be potentially be modulated pharmacologically to prevent or reverse bone loss during diseased states. Exercise as a mechanical stimulus has proven to successfully increase bone density in humans and animal models, although the skeletal benefits slowly decline after cessation of the regimen [43-46]. While the benefits of exercise to the skeleton in humans and animal models are well recognized, physical activity as a method of mechanically loading the skeleton to study bone's adaptive response has many limitations including lack of a contralateral control limb, difficulties characterizing the resulting strain environment, and inability to tightly control load parameters, all of which are extremely important for understanding the resulting skeletal response. Experimentally applied loading allows much tighter control over more parameters of the load. Previous studies have used the ulna or tibia from animal models such as the turkey, rat, and mouse, and have employed a few different loading methods including functional isolation, four-point bending, and axial compressive loading. Currently, axial compressive loading of the mouse tibia is used most frequently because it is noninvasive and induces a strain environment in the bone that more closely emulates physiologic conditions compared to the other methods [34], although all methods have provided significant insight into skeletal adaptation. The highly controllable load parameters of these methods allowed revelations into bone's sensitivity and resulting adaptive response to parameters such as load magnitude, rate, frequency, number of cycles, and study duration. The load must be applied dynamically in order to be osteogenic [47]. Applied loading engendering strains from sub- to supraphysiologic levels produces a linear dose response relationship with the amount of new bone formed [24, 30, 47-50], except for loads engendering physiologic-level strains to which the bone is already adapted [51]. The load-induced signal for adaptation will saturate after a certain number of consecutive load events [50]. Increasing the strain rate [52, 53] or frequency [54] while maintaining identical load levels causes proportional increases in bone formation. Incorporating rest periods both between each load in a loading bout [55], and separating a set number of loading cycles into bouts throughout the day, makes the applied load more osteogenic for cortical bone than applying that set number of loading cycles consecutively [56-58]. Despite load parameter optimization, increasing age has a negative effect on skeletal responsiveness to mechanical stimuli [59-61].

1.6 Assessing Tissue-level Skeletal Response to Load

Tissue-level skeletal adaptation is typically identified by changes in bone geometry and/or density relative to the non-loaded contralateral control limb as measured by micro-computed tomography (μCT) or histology. Typical cortical bone measures from μCT include maximum and minimum moments of inertia (I_{max}, I_{min}), cortical bone area (Ct.Ar), cortical thickness (Ct.Th), and bone mineral density (BMD). Several studies have reported that bone curvature decreased as a result of loading through location specific bone formation and resorption [30, 52] which would decrease bending strains at the midshaft and correlate to increases in moment of inertia. Similarly, increases in Ct.Ar, Ct.Th, or BMD would increase bone strength and resistance to bending and reduce the strain induced relative to the applied load. If flourochromes are injected to the subject during the experimental loading study, fluorescence will incorporate as new mineral is deposited. After completion of the loading study, histomorphometry can be used to measure the active mineralizing surface (MS), mineral apposition rate (MAR) and bone formation rate (BFR)[62]. Unlike morphometry measures from μCT, multiple flourochrome injections throughout the study can be used to determine the skeletal response throughout the course of loading rather than just the final adaptive outcome, as well as the specific surfaces where mineral was deposited.

1.7 Genetic Regulation of the Skeletal Response to Mechanical Load

Understanding the genetic mechanisms responsible for osteoregulation during skeletal adaptation is critical for the development of pharmacologic treatments for bone loss conditions when external loading is an insufficient stimulus for bone maintenance. One of the first signaling pathways recognized as important in bone cell mechanotransduction was the cyclooxygenase (COX)-prostaglandin E_2 (PGE_2) response; while load-induced bone formation was only partially inhibited by blocking both *constitutive* (COX-1) and *inducible* (COX-2) cyclooxygenase, completely blocking COX-2 resulted in almost no bone formation [63] with a greater effect on the endocortical versus periosteal surfaces [64]. Also, blocking COX-2 after load application did not suppress new bone formation, further suggesting that the COX-2 pathway is part of the very early adaptive response [64]. The canonical Wnt signaling pathway has also been implicated as key for bone cell mechanotransduction. Wnt signaling occurs through low-density lipoprotein receptor-related protein-5 or -6 (LRP5/6) and a heptahelical frizzled (FZD) receptor complex in osteocytes that, when activated, prevents proteosomal degradation of β-catenin, a transcription factor associated with several genes that enhance osteogenesis and reduce resorption, therefore allowing increased transcription of bone formation associated genes [65]. Loading increases activation of the Wnt pathway and Wnt/β-catenin target genes of a whole bone, which is further enhanced in LRP-5 G171V transgenic mice, a mutation which causes greater activation of the Wnt pathway, as well as non-transgenic animals treated with a canonical Wnt pathway activator [66]. Deletion of functional LRP5 prevents an osteogenic response to load [67, 68]. Sclerostin, produced by the osteocyte and encoded by the *SOST* gene, binds to the LRP5/6 receptors and inhibits the Wnt signaling pathway, but is down-regulated by mechanical load which then allows the Wnt pathway to activate[69, 70]. In addition to *SOST*, osteocytes also express the Wnt inhibitors DKK1 and sFRP1, which prevent osteoblast differentiation and LRP5/6-Wnts binding

[71]. Mechanical load also stimulates the nitric oxide (NO) signaling pathway, which has been shown to be critical for an osteogenic response [72, 73]. Up-regulation of *c-fos*, transforming growth factor-β (TGF-β) and insulin-like growth factor-I (IGF-I) during the early periosteal osteogenic response cause cell proliferation and increased synthesis of growth factors [74]. Known osteoblast-specific genes that up-regulate in response to load in order to increase bone formation include the osteoblast precursor Col1a1 and alkaline phosphatase (Alp)[75, 76].

Bone cells responsible for instigating a response to mechanical load as well as general modeling/remodeling are also controlled by systemic factors including several hormones and growth factors [77]. Parathyroid hormone (PTH) is involved in regulating calcium homeostasis by inducing bone turnover. Intermittently elevated levels of PTH reduce sclerostin synthesis and increase osteoblast numbers, ultimately enhancing the bone formation rate without coupled prior resorption typical in bone turnover [78, 79]. The effects are further enhanced when coupled with mechanical load [80]. Calcitonin inhibits osteoclast formation and promotes apoptosis, preventing bone resorption, while also inhibiting osteocyte and osteoblast apoptosis [81, 82]. Elevated glucocorticoid levels have a negative effect on bone mineral density by causing osteocyte and osteoblast apoptosis, and over time can lead to osteoporotic levels of bone loss [83-85]. Growth hormone and IGF-I increase bone formation by stimulating osteoblast activity and decreasing osteoclast numbers [86], and mechanical load has a regulatory effect on IGF-I levels [87]. The sex hormones, estrogen and androgen, stimulate osteocyte and osteoblast proliferation and decrease apoptosis, while reducing osteoclast formation and lifespan [88]. Additionally, serum levels of calcium and phosphate regulate whether mineral deposition to bone or resorption occurs. Resting metabolic rate (RMR) has also been correlated to periosteal bone growth rates [89].

1.8 Gap Statement

Comparatively assessing bone cell populations and changes in skeletal gene expression in response to mechanical load stimuli in diverse vertebrate groups may provide novel insights into the cellular mechanisms that regulate skeletal mechanobiology and the causes behind skeletal diseases such as osteoporosis. A deeper understanding of how the skeleton is naturally modulated will help to better inform the development of physical and pharmacological treatments to treat skeletal diseases like osteoporosis. Improved treatments would seek to not only stop further bone loss, but also to reverse it and reestablish skeletal integrity, or even to prevent the initial failure of the mechanisms responsible for maintaining adequate bone quality properties.

Mice have provided a wealth of knowledge regarding the skeleton and the mechanobiology of bone adaptation over the past 30 years, which describes how different cells and tissues sense and respond to mechanical forces. However, sole use of rodent models only propagates a large gap in understanding the basic cellular mechanobiological mechanisms responsible for skeletal structural diversity and homeostasis in terrestrial vertebrate groups. Although the skeleton is comprised of the same bone cells and similar material composition, it is extremely diverse across vertebrate species in its morphology, geometry, and mechanical properties. Ectothermic reptiles and amphibians have greater cortical thickness relative to diameter and increased safety factors compared to endothermic mammals and birds [90], which may be necessary due to a lower potential for skeletal adaptation. Despite evolving from reptilian ancestors, avian species today have a lighter and less metabolically costly skeleton, due to pneumatization of certain bones, making them more similar to derived mammals such as the mouse [91-93]. Additionally, avian bone is more dense than mammalian bone, which gives it greater stiffness and strength while minimizing bone mass and volume [93]. Stiffness and toughness of a bone is relative to its mineral content, and mechanical properties such as these vary considerably across all species, as well as by the specific bone [94, 95]. Avian and reptilian species are also unique to vertebrates in that they lay eggs with calcified shells, which involves special regulation of calcium balance hormones and more labile skeletons [96]. Additionally, avian species are uniquely able to form medullary bone, non-structural woven bone on endosteal surfaces, which serves as a calcium reservoir for egg-laying females and experiences varying rates of osteoclastic and osteoblastic activities [96, 97], although it can be induced in male birds as well with the administration of estrogen [98]. Fracture repair across vertebrate species received some brief attention several decades ago, and showed that repair was slower in reptiles relative to rodents [99]. Despite similar cell types and genes acting in the skeletons of these different species, osteoregulatory genetic and cellular mechanisms, as well as systemic physiologic factors are likely expressed differently across vertebrate taxa. Within two inbred strains of mice, differential responses to similar mechanical loads have been demonstrated [100]. How these differences are regulated and how they may affect skeletal response to similar mechanical loads is unknown.

Since one of the primary functions of the skeleton is to provide mechanical support during movement, it is likely that skeletal sensitivity and response to mechanical load is tuned to the needs of each species, yet skeletal adaptation studies have been performed on only a few select mammalian and avian species, and that number decreases more when only considering noninvasive models for inducing adaptation. There is a lack of fundamental insight into the mechanisms responsible for the potentially differential regulation of the skeleton in response to mechanical load across species. By comparatively assessing skeletal adaptation and its mechanobiological regulation across novel vertebrate species, we will establish a deeper understanding regarding the genetic, cellular, and systemic factors involved in bone modeling/remodeling, as well as potentially identify novel mechanisms and previously unrealized targets that could further enhance the development of pharmacologic treatments for skeletal metabolic diseases.

2. EXPERIMENTAL TESTS OF PLANAR STRAIN THEORY FOR PREDICTING BONE CROSS-SECTIONAL LONGITUDINAL AND SHEAR STRAINS

2.1 Introduction

The application of methods for predicting the distribution of longitudinal strains normal to a long bone's transverse cross-section, and the location of the neutral axis of bending in the cross-section, has significantly enhanced our understanding of the diversity of *in vivo* skeletal loading regimes found in vertebrate long bones during locomotion. Surface strain gauge measurements are used frequently to characterize 'typical' bone tissue strains during locomotion *in vivo,* as well as artificially-induced *ex vivo* strains, in order to estimate safety factors and mechanical properties in a large variety of animals and bones [24, 101-105]. Limitations of bone size and surgical surface availability often restrict the possible locations for gauge implantation as well as the type and size of the strain gauge used (single element versus rosette gauge). As a result, it is often difficult to place gauges at the exact locations of maximum strain, even if these locations can be estimated *a priori*. However, if three strain gauges can be distributed around the diaphyseal cortex, planar strain theory (PST) can be used to estimate the cross-sectional strain distribution, the sites of maximum tensile and minimum compressive strains, and the location of the neutral axis of bending [106-108]. Although this technique is used frequently in *in vivo* skeletal biomechanics studies, its accuracy for this application and the possible effect of gauge distribution around the diaphysis have not been validated experimentally to our knowledge.

Measures of shear strain, which are dependent upon the magnitudes and orientations of the principal strains in the bone, describe the off-axis loading of the bone including long-axis torsion, and can be calculated directly when a rosette gauge is attached to the bone's surface [106, 109]. While these direct measures of bone tissue shear are only valid at the location of the rosette gauge, there is interest in determining maximum shear strains around a bone's circumference, which may not coincide with the location of the attached rosette strain gauge. Some studies have applied PST-based longitudinal strain ratios to shear strain measures at one location to estimate shear strains at the PST-determined maximum longitudinal strain location on the bone [102, 105]. In this approach, an average longitudinal strain ratio was determined between the longitudinal strain values measured at a rosette gauge site and the site of maximum compressive strain on the bone, determined using PST from all animals in the study. This average longitudinal strain ratio was then applied to the shear strain measured at the rosette gauge for each animal to predict each individual's maximal shear strains. In this way, the estimated peak shear strain in the bone would always be larger than the measured shear strain, ensuring that any safety factor determined based upon the *in vivo* strain data would not be artificially inflated by using submaximal shear strain values. This approach requires the assumptions that shear strains increase in proportion to longitudinal strains around the bone's cortex, and that maximum shear strains occur at the same location as maximum longitudinal strains. These assumptions have not been experimentally validated in published literature. While the equation for shear strain does include a component of the longitudinal strain, it also depends on off-axis strain values and principal strain angles that do not necessarily change in a predictable way around a bone cross-section, but could have a large impact on shear strain values.

One goal of this paper is to evaluate the accuracy of PST in predicting cross-sectional strains given different strain gauge distributions around the cross-section of the bone. To address this goal, we attached four strain gauges around the midshafts of adult emu tibiotarsi (TBT) and loaded the instrumented bones in *ex vivo* four-point bending. Using combinations of experimentally measured strain values from three of the four gauges to create planar strain reconstructions for the midshaft cross-sections, we determined the predicted strain value at the location of the fourth gauge and compared it to the corresponding experimentally measured value. We hypothesized that regardless of the distribution of the gauges around the midshaft used for calculations, reconstructed strains would not be significantly different from the measured strains.

Our second goal was to evaluate the use of longitudinal strain ratios for extrapolating shear strains measured from a rosette strain gauge to positions on the bone cross-section that were not strain gauge-instrumented or were instrumented with a single element gauge incapable of measuring shear strain. To this end, *in vivo* longitudinal and shear strains were measured using three rosette strain gauges on the posterior, anterior, and medial midshaft surfaces of guinea fowl TBT at a specific point in the stride during treadmill running. With this data we tested the assumptions made when using longitudinal strain ratios relating the longitudinal strains at two gauge sites for predicting shear strain from one rosette gauge site to another. Like similar attempts to do this previously (Blob and Biewener, 1999; Butcher et al., 2008), this prediction makes the assumption that shear strains change in proportion to longitudinal strains across the cross-section. While our methods require shear strain predictions to be extrapolated to locations on the bone surface that may not coincide with the maximum longitudinal strain, our extrapolations to sites of empirically-measured shear strains allow us to experimentally test the predictions. We hypothesized that this type of extrapolation would not provide reliably accurate estimations of measured shear strains since it does not include the necessary contributions of off-axis strain.

2.2 Materials & Methods

2.2.1 Planar Strain Theory Validation

The TBTs of emu (*Dromaius novaehollandiae*, Mathews) were used in four-point bending tests to validate PST for animal long bones. The TBTs used in this study (n=5) were from the non-instrumented right limbs of birds used in a prior *in vivo* bone strain study (Main and Biewener, 2007). At time of sacrifice, the birds ranged in age from 36 to 75 weeks of age (62±18 weeks, mean ± 1 SD) and in mass from 29 to 52 kg (40.6 ± 11.4 kg). Upon sacrifice, the birds' hind limbs were dissected from the body and frozen at -20°C. At a later date, each TBT was thawed, cleaned of soft tissue and muscle, wrapped in water soaked paper towel, wrapped in a plastic bag, and re-frozen at -20°C. Prior to the testing conducted for this study, the bones were individually thawed, aligned using a custom alignment frame and fixed in machined aluminum pots using a commercial fast drying cement (Body Filler, 3M, Saint Paul, MN, USA). The proximal and distal ends of the bone were embedded such that 50% of bone length centered at the midshaft remained exposed. Exposed bone was kept moist at all times using saline-soaked paper towels during potting and between mechanical tests. Once the cement hardened, the potted bones were refrozen at -20°C. At a later date, the bones were thawed for the final time to conduct strain gauge implantation and mechanical testing. Thus, all bones went through three freeze-thaw cycles prior to mechanical testing. Once thawed, three rosette strain gauges (FRA-2-11, Tokyo Sokki Kekyujo Co., Ltd, Tokyo, Japan) and one single element gauge (FLA-3-11) were attached around the circumference of the bone's midshaft (**Figure 2.1**). A 1.5 cm^2 region of periosteum was scraped away at each gauge attachment site using a periosteal elevator. The bone surface was defatted and dried using 2-butanone (Sigma-Aldrich, St. Louis, MO, USA) and the gauges bonded to each site using a self-catalyzing cyanoacrylate adhesive (DURO Superglue, Loctite, Westlake, OH, USA). Rosette strain gauges were attached to anterior, posterior, and medial surfaces and a single element gauge was attached to an anterior-medial surface at the bone's midshaft with a goal of spacing the gauges as evenly around the cross-section as possible while respecting any bone surface limitations. The gauges were oriented so that the central element of each gauge was aligned with the long axis of the bone. Gauge lead wires were soldered to a micro-connector (4-103240-0, Digi-Key, Thief River Falls, MN, USA) that was plugged into a 1m shielded cable (NMuF 6/30-404655, Coonerwire, Chatsworth, CA, USA), to convey raw strain signals to Vishay amplifiers (2110B, Vishay Precision Group, City of Industry, CA, USA). During testing, amplified strain signals were sampled at 100 Hz through an A/D converter and converted to microstrain (με, strain x 10^6) in the manufacturer's software (Labchart7, ADInstruments, Dunedin, New Zealand).

Each instrumented emu TBT was loaded over its linear elastic range (i.e. not to failure) in four-point bending. A -10 N pre-load was applied to hold the specimen in place and to maintain equal distribution of load among the four contact points. Five triangular waveform cycles of preconditioning from -10 to -20 N were applied at a load rate of 0.25 mm/sec, immediately followed by 10 triangular waveform load-unload cycles from -10 to -175 N compressive load at 0.25 mm/s to induce an average peak bending moment of -9.63 Nm at the time of maximum applied load (**Table 2.1**, **Figure 2.2**). Each surface of the bone was loaded in turn in compression by placing the surfaces sequentially 'face-up' in the load fixture in the following order: anterior, medial, posterior, and lateral. The applied load from the load cell and bone strain readings from the four strain gauges were collected synchronously. The length:width aspect ratio of the tested bone region was approximately 18:1.

Following the four-point bend tests, planar strain analyses were conducted using different three-gauge combinations in order to test the accuracy of this method for modeling load-induced strains against the measured strain in the fourth gauge. Using a custom MATLAB (Mathworks, Natick, MA, USA) program, the raw longitudinal strain values were zeroed by subtracting the average strain in each channel measured prior to the upper load fixture contacting the sample. Then, a single cross-sectional slice from a CT scan (0.63 mm in-plane resolution, GE Lightspeed VCT, GE Healthcare, Purdue Veterinary Teaching Hospital) of each bone with all 4 gauges visible was imported into MATLAB and the location of each gauge manually selected in the program. In each bending orientation, the longitudinal strains were predicted for each gauge location in turn using the strain measures from the three other gauges and equations previously described for calculating the distribution of longitudinal strains normal to the bone's cross-section [106, 107].

$$\varepsilon_1 = A\,x_1 + B\,y_1 + C$$
$$\varepsilon_2 = A\,x_2 + B\,y_2 + C$$
$$\varepsilon_3 = A\,x_3 + B\,y_3 + C \quad \textbf{(1),}$$

Eqn 1 represents the equations used for PST predictions. 'x' and 'y' are the 2D coordinates of the strain gauge position on the bone cross-section. Strain (ε) is the strain measured at the corresponding gauge site. By solving the set of three equations, the coefficients A, B, and C can be determined. Once those coefficients are known, the strain at any location across the bone's cross-section can be determined. For each gauge, peak and predicted strains were determined for the final five load cycles for each bending direction and then averaged, resulting in a measured strain and predicted strain for each gauge on each bone. Thus, in Figure 3 each data point represents a mean value for measured and predicted strains for five cycles of loading for each bone. Calculated versus measured strains were plotted for the four gauge locations in each of the four bending directions for the n=5 bones tested, such that each bone is represented by 4 data points (once for each bending direction). A least-squares linear regression was fit to the predicted vs. measured strain data for each strain gauge location for all birds (20 data points; 5 birds with 4 strain gauge predictions each) across the four bending directions to determine the slope between the measured and calculated strain values. Ninety-five percent confidence intervals (CI) were calculated to determine if the slope of the regression was significantly different from unity.

We also quantitatively characterized the extent of the circumferential coverage of the strain gauges for the different 3-gauge combinations by measuring the length along the bone's circumference between the three successive gauges for each combination. This was achieved by manually tracing the total circumference of the bone and the length of the perimeter between the center of the gauge foil for each of the three successive gauges for each combination from the CT scan images (ImageJ, National Institutes of Health, Bethesda, Maryland, USA). Coverage percentages were averaged for all five animals for each of the four three-gauge combinations.

2.2.2 Extrapolation of Planar Strain Theory to Shear Strains

Male french guinea fowl (*Numida meleagris,* Linnaeus) were used to evaluate the validity of using the relationship between planar strains at two cortical bone sites in a cross-section to determine shear strains at a bone site remote to the location of a rosette strain gauge. All birds used were obtained from a commercial farm (JM Hatchery, New Holland, PA, USA; n=5) as hatchlings and raised at Purdue University in an indoor enclosure with free access to game bird feed and water until they were used in the study (age: 21.6$\underline{+}$0.9 weeks, mass: 2.72$\underline{+}$0.27 kg). All surgical and experimental procedures followed protocols approved by the Purdue University IACUC (PACUC Protocol #1310000977).

Aseptic surgery was conducted to attach strain gauges to each bird's left TBT. The birds were induced for surgery through mask inhalation of isoflurane (5%), and maintained at a surgical anesthetic plane with 2-4% isoflurane at a 1L/min O_2 flow rate. Breathing and heart rate were monitored throughout surgery, and anesthesia adjusted as necessary. To attach strain gauges to the midshaft of the TBT, incisions were made at the lateral border of the synsacrum and on the medial side of the TBT at the midshaft. Three rosette strain gauges (FRA-1-11, Tokyo Sokki Kenkyujo Co., LTD, Tokyo, Japan) and their lead wires were passed subcutaneously from the incision at the sacrum to the incision at the TBT midshaft. After retracting the overlying muscles to expose anterior, posterior, and medial bone surfaces, each surface was prepared for gauge attachment by removing an approximately 1 cm^2 region of periosteum, lightly scraping the underlying surface with a periosteal elevator, and defatting and drying the surface using 2-butanone (Sigma-Aldrich, St. Louis, MO, USA). Strain gauges were then bonded to each site using a self-catalyzing cyanoacrylate adhesive (DURO Superglue, Loctite, Westlake, OH, USA). Gauges were centered on each surface as much as possible (Fig. 4), and the central element of the rosette was aligned with the long axis of the bone within 5^o. Once all three gauges were bonded to the TBT, the overlying musculature was carefully replaced and the incisions overlying the hip and TBT were sutured (4-0 coated Vicryl violet braided, J392H, ETHICON, Somerville, NJ, USA). The lead wires exiting over the synsacrum were further anchored to the skin with suture to provide tension relief for the wires, and the incision and the pre-soldered epoxy mounted connector were covered with gauze and elastic bandaging tape. Following surgery and immediately prior to experimental testing the following day, each bird was given intramuscular injections of analgesic (0.5 mg/kg meloxicam, VETone, Boise, ID, USA).

The day following surgery, *in vivo* bone strain data were collected as the birds ran on a motorized treadmill over a range of speeds, but we only present data collected at the greatest running speed achieved, which was at 2.68 m/s. While on the treadmill, the lead wire connector over the hip was connected to a 5.4 m long shielded cable and the plug-cable connection was secured to the tail feathers with additional elastic bandaging tape. The cable was connected to a Vishay bridge amplifier, from which raw strain signals were sampled by an A/D converter at 2000 Hz. Following data collection, the birds were induced to a surgical plane of anesthesia by mask inhalation of isoflurane (5%) at a 1L/min O_2 flow rate and then euthanized via intravenous injection of sodium pentobarbital in the brachial vein (320 mg/kg Beuthanasia-D, Schering-Plough Animal Health, Union, NJ, USA).

Raw strain data for five consecutive, steady footfalls within each trial for each bird were imported into a custom MATLAB program for further analysis. Zero strain levels were determined by averaging the strains during the swing phases of the selected strides. Raw strain data from each rosette were used to calculate principal tensile and compressive strains and the orientation of these strains relative to the long axis of the bone using standard equations that assume a uniaxial planar state of strain [106].

$$\text{Principal Tension: } E1 = (\varepsilon_a + \varepsilon_c)/2 + [(\varepsilon_a - \varepsilon_c)^2 + (2\varepsilon_b - \varepsilon_a - \varepsilon_c)^2]^{1/2}/2$$

$$\text{Principal Compression: } E2 = (\varepsilon_a + \varepsilon_c)/2 - [(\varepsilon_a - \varepsilon_c)^2 + (2\varepsilon_b - \varepsilon_a - \varepsilon_c)^2]^{1/2}/2$$

$$\text{Angle of Principal Compression } \phi = ½(\tan^{-1}[(2\varepsilon_b - \varepsilon_a - \varepsilon_c)/(\varepsilon_a - \varepsilon_c)]$$

$$\gamma = 2 * (E1 * \sin\Phi * \cos\Phi - E2 * \sin\Phi * \cos\Phi) \qquad \textbf{(2),}$$

The equation for calculating shear strains (γ) relies on the calculation of principal strains E1 and E2, as well as the angle of principal tension, ϕ. The equations for principal tension, compression, and the angle of principal tension include contributions from longitudinal strain measures (ε_b) as well as the off-axis components of strain (ε_a and ε_c) that can all only be experimentally measured simultaneously using a rosette strain gauge.

The time point during stance corresponding to minimum longitudinal strain (peak compression) on the medial surface was chosen for further shear strain analysis in order to guarantee that both posterior and medial gauges were simultaneously measuring compression so that our shear predictions based upon the measured longitudinal strains would not attempt to cross the neutral axis. Shear strains were calculated for each gauge at the relevant time point using Eq. 2 [103], and mean values for the five stance phases analyzed per bird were calculated for both the medial and posterior gauges. Based upon these mean values, an individual ratio between posterior and medial longitudinal strain was found for each bird as well as the ratio between the mean medial and posterior longitudinal strains for all animals. Both ratios were then used to separately predict shear strain values at the posterior gauge site using the mean shear strain value measured for each bird at the medial gauge site (**Table 2.3**). Our methods were designed to closely replicate those used previously [102, 105]. Previous use of this approach used experimentally measured shear and longitudinal strains collected at one bone location to project shear strains to a site on the bone where the maximum longitudinal strains were expected to occur based upon the planar strain analysis of longitudinal strains. Because we did not know the location of peak longitudinal strain prior to gauge implantation, and would therefore not have a gauge present at this site to experimentally validate the extrapolation of shear strains from known measures, we had to make predictions from a medial to a posterior location, where we could reliably attach rosette gauges in all birds. Additionally, while similar prior studies used a mean longitudinal strain ratio from all animals in the study (typically n=2-4), we also found individual ratios for each animal to highlight the variation within a sample. Thus, the measured shear strain data plotted in Figure 5 represent the mean shear strain values from the posterior gauge measured over five consecutive stance phases and a single predicted posterior shear strain value for each individual. The predicted shear values are based upon the mean shear strains measured at the medial rosette gauge site and either a (i) mean longitudinal strain ratio for each bird or (ii) a mean longitudinal strain ratio averaged across our five bird sample. Predicted vs. measured shear strains for both ratios were plotted and a least squares linear regression fit was applied to each to determine the relationship between measured and predicted shear strain values at the posterior gauge site. Ninety-five percent confidence intervals were calculated to determine if the relationships between measured and predicted shear strains were significantly different from unity.

2.3 Results

2.3.1 Measured vs. Calculated Longitudinal Strains

All emu TBTs underwent 4-point bending in both directions across the medio-lateral and antero-posterior axes, sequentially placing each of the anterior, posterior, medial, and lateral bone surfaces in compressive and tensile strains of varying magnitudes. Strains near zero indicate that the gauge site was close to the neutral axis during bending, as would happen for the anterior gauge site when the upper load points contact the medial or lateral bone surface. For all strain gauge sites, the relationship between measured and calculated longitudinal strains was linear, and the slope of the regression line not significantly different from 1.0 as indicated by 95% CIs that include the value 1.0 (**Figure 2.3**). Y-axis intercept values were all less than 6με, thus not deviating markedly from the origin. R^2 values for anterior, posterior, medial and anterior-medial (single-element gauge) sites were 0.99, 0.94, 0.98, and 0.99, respectively. The percentage of gauge coverage of the bone's circumference during prediction of the anterior, posterior, medial and anterior-medial gauge sites was 47±4%, 32±3%, 55±4% and 70±2%, respectively. This indicates that predictions for the anterior-medial gauge were based upon the broadest gauge coverage of the bone circumference, while predictions for the posterior site were based upon the most restricted gauge coverage of each bone's circumference. Even for the surface with the most restricted gauge coverage, the correlation between measured and predicted strains was strong.

2.3.2 Extrapolation of Planar Strain Theory to Shear Strains

Measured shear strains at each rosette gauge and predicted values were analyzed at the time point of the minimum medial axial strain (maximum compression) during stance phase (29±7% through stance) for the five most consistent steps from each trial. Inter-animal variation in gauge position and the approximate location of the neutral axis at the time point analyzed are depicted in **Figure 2.4**. The individual-specific ratios of posterior to medial longitudinal strains ('longitudinal strain ratio', **Table 2.3**) varied considerably across the different birds (range: 0.28-5.35) indicating that for some birds, posterior longitudinal strains were greater than medial longitudinal strains, while for others the opposite occurred. The causes for this variation can be discerned from the varying strain distributions in the guinea fowl TBT (**Figure 2.4**), where for some birds the medial gauge is located closer to the neutral axis (e.g. Birds 3 and 4), while for others the neutral axis of bending falls closer to the posterior rosette gauge (e.g. Birds 1 and 2).

Extrapolated shear strain values using the individual-specific ratio of posterior:medial longitudinal strains resulted in a poor correlation overall between the measured and predicted shear strains at the posterior gauge site. The applied linear fit had a slope of 0.23 (R^2= 0.10) and intercept value of -327με (**Figure 2.5**). The sample-mean multiplier (1.52) also resulted in a better correlation between measured and predicted shear strains at the posterior gauge site than the individual-specific correlation, with an applied linear fit slope of 0.52 (R^2 = 0.37) and an intercept value of -217 με. Although the resulting confidence ranges for both multipliers included relationships with slopes equal to 1.0, they also included lines with slopes equal to 0.0. Both the individual-specific and sample-mean ratios produced a positive slope between the measured and predicted posterior site shear strains, which may suggest that, at least for the guinea fowl TBT, using this technique could help prevent underestimation of maximal shear strains in the bone.

2.4 Discussion

Planar strain theory (PST) is used in skeletal mechanics studies to predict the distribution of longitudinal strains normal to the bone's transverse cross-section and the location of the neutral axis of bending [24, 102-105, 108, 110]. To our knowledge, application of this theory to skeletal mechanics has not been experimentally validated. One of our primary goals in this study was to assess the accuracy of PST calculations in matching experimentally measured strain values at several strain gauge sites around a bone's cross-section. We found that predicted strain values closely matched experimentally measured values in long bones loaded in four-point bending. PST has also been used to extrapolate possible peak shear strain values at locations on the bone not instrumented with rosette strain gauges [102, 105]. We sought to test the use of a linear model based upon longitudinal strain measures for predicting shear strains in long bones. Shear strains include contributions from off-axis strain components (Eqn. 2) that can only be measured using rosette strain gauges and which may not scale linearly across a bone's cross-section as longitudinal strains do during long bone loading. For our experimental conditions, we found that shear strain values predicted from *in vivo* measures of longitudinal strain generally did not correlate well to experimentally measured shear strain values for the guinea fowl. However, both ratios did result in a relationship with a (non-significant) positive slope between the predicted and measured shear strains. Therefore, this technique may help to prevent underestimation of maximal shear strains by predicting increased shear strains with increased longitudinal strains. However, because both positive relationships were non-significant trends, the accuracy of this method could still be questioned.

2.4.1 Planar Strain Theory: Longitudinal Strain

PST predicts that for an element in bending, longitudinal strains increase linearly perpendicular to the neutral axis of bending. When applied to long-bone biomechanics, this theory assumes that bone material is linearly elastic, isotropic in the transverse plane of section, and has a perfectly cylindrical cross-section [109]. If these assumptions are closely matched, longitudinal strain values predicted theoretically at particular sites across the plane of section should equal the experimental strain gauge measures at those same sites. Our results showed that for all four gauge sites sampled, measured and predicted longitudinal strains had a linear relationship not significantly different from unity with y-intercept values less than ±6 $\mu\varepsilon$. These data support our hypothesis and the use of PST for predicting bone cross-sectional longitudinal strain distributions when the three gauges required for making longitudinal strain predictions are evenly distributed around the cross-section. In addition, our data evaluated the effect of an uneven distribution of gauges in making longitudinal strain predictions. Theoretically, the location of the three gauges around the cross-section should not affect predicted strain values. While we found that the linear fit for measured versus calculated longitudinal strains was good for all gauge sites and strain gauge distributions tested, gauge distribution did have a small effect on the confidence of the prediction. Predicted strains for the anterior-medial gauge site had the tightest 95% confidence interval (±0.08) and the greatest percentage of bone perimeter covered (70±2%) by the three gauges used to predict the strains at this fourth gauge site. Predicted strains for the posterior gauge site showed the largest confidence interval (±0.24) and the three gauges used to predict longitudinal strains at this site covered the lowest percentage of bone perimeter (32±3%) of the different gauge combinations examined. Even though surgical accessibility and bone surface limitations often limit gauge placement and distribution around a cross-section during *in vivo* experiments, our results suggest that an even distribution of gauges around the cross-section is not critical when the goal is to model cross-sectional strain distributions using PST. However, predictions made from uneven gauge distributions seem to have slightly more variability. Because the emu TBTs tested here were not solid cylindrical columns of homogeneous bone tissue, results from PST predictions appear to be relatively insensitive to the presence of a marrow canal and the bone tissue heterogeneity likely present in the bones we tested.

The bending moment applied to each bone varied slightly (-8.6 to -10.7 Nm). Because our 4-point bending device allows the support points to be adjusted, and they were manually reset between each experiment, the distance between the inner-most and outer-most supports varied (0.10 to 0.12m), causing slight variations in the applied moment. Since our analysis did not depend on achieving specific strain values or specific loads, but rather examined the relationship between strains around a bone's cross-section, the variation in applied moments do not affect our results or conclusions. Theoretically, regardless of the moment applied, longitudinal strains should increase linearly perpendicular to the neutral axes.

Planar strain theory is often used to evaluate how the *in vivo* strain environment across a bone's cross-section varies during locomotion [102, 103, 111], which typically induces a combination of bending, axial compressive, and torsional loads in long bones. We evaluated PST predictions using strain data from bones loaded *ex vivo* in four-point bending, which induces only pure bending. While our results suggest that longitudinal strain predictions closely match the measured strains around a cross-section for pure bending situations, we could not assess the effect of other types of loading combined with bending on the cross-sectional strain distribution and the accuracy of PST predictions in these experiments. Limitations of our mechanical loading system prevented us from applying combinations of bending, compressive and torsional loads to specimens *ex vivo*. Additionally, muscle forces during locomotion could affect the local *in vivo* strain environment which we could not account for in our *ex vivo* loading model. A valuable future study would include a similar four-gauge analysis conducted *in vivo*. However, as previously stated, *in vivo* gauge attachment is often limited by bone size and surfaces as well as muscle attachment locations. For example, we were not able to perform such a study with the guinea fowl TBT that were used to predict shear strains because there was not an available surface to add a fourth gauge.

2.4.2 Planar Strain Theory: Shear Strain

Determining the maximum diaphyseal shear strain in a bone during locomotion is also commonly of interest, as shear strain accounts for the off-axis strain components due to torsional and eccentric loading in a bone during locomotion. Just as for longitudinal strains, it is difficult to place a rosette gauge at the location of maximum shear strain without *a priori* knowledge of where peak strains occur around a bone’s circumference. Thus, to be able to accurately predict shear strains at non-instrumented locations would be a valuable extension of PST. Attempts have been made to predict shear strains using PST, which makes the assumption that shear strains increase linearly perpendicular to the neutral axis and in proportion to longitudinal strains. As this has been applied to *in vivo* locomotion and *ex vivo* mechanical tests, an average longitudinal strain ratio for the animals used in the study is first determined between measured longitudinal strain values from a rosette gauge located at a similar bone site in each animal, and the longitudinal strain values determined by PST at a non-instrumented location (typically the location of maximum longitudinal strain). Then the average ratio between the strains at these two sites across all animals in the study is applied to the shear strain measured at each rosette gauge location to produce predicted shear strain values at the non-instrumented locations [102, 105]. However, since shear strains include contributions from off-axis components of strain in addition to longitudinal strain (Eqn. 2), it is unclear how accurately the ratio between two longitudinal strain values at different sites around a bone’s circumference can be used for predicting shear strains at sites remote to rosette gauge locations.

Our *ex vivo* loading model was not capable of applying the combined axial or bending and torsional loads necessary to create significant shear strain in the bone, so we turned to *in vivo* rosette strain data collected from the guinea fowl TBT during treadmill locomotion to test the accuracy of shear strains predicted using longitudinal strain ratios. At this time we cannot compare the accuracy of our *in vivo* PST-based shear strain predictions to similar *in vivo* locomotor longitudinal strain predictions because we did not have a fourth strain gauge placed *in vivo* for longitudinal strain validation. However insight into the accuracy of applying PST to shear strain predictions is still important for drawing conclusions from its future use. We did not have *a priori* knowledge of the location of the maximum axial or shear strain at the TBT midshaft in this experiment, so it was not possible to place a rosette gauge at those specific locations to provide empirical data to compare to our predictions. Therefore, we were not able to exactly mimic the methods used previously where measured shear strains were extrapolated to the site of the predicted peak compressive strains on the bone [102, 105]. However, if the assumption holds that shear strains, like axial strains, increase linearly perpendicular to the neutral axis, the longitudinal strain ratio should be able to reliably predict the sub-maximal shear strain values we measured just as successfully as it would maximal values.

Our methods tested extrapolation of shear strains from a rosette gauge site on the medial surface of the guinea fowl TBT to a rosette gauge site on the posterior surface. We used both individual-specific and sample-mean longitudinal strain ratios in order to highlight intra-species variation and to more closely mimic previous methods, respectively. We found that for both of the ratios used for shear strain prediction, the predicted versus measured shear strains did not correlate linearly with a zero y-intercept for the guinea fowl in this study. Furthermore, while a slope of 1.0 fell within the confidence intervals for the linear regressions for both ratios used, the intervals themselves were large (-1.10 to +1.50 for individual-specific ratios, -0.73 to +1.77 for sample-mean ratio). There are some limitations in using 95% confidence intervals to distinguish our empirical relationship from an idealized slope since 95% confidence intervals rely heavily on sample size. In this case, a linear regression based upon five data points may have led to particularly wide intervals. An increased sample size in future studies could potentially reduce the width of these intervals. Additionally, the individual longitudinal strain ratio between posterior and medial longitudinal strains was both above and below 1.0 depending on the bird, indicating that the location of the neutral axis varied considerably across the birds at the time point used for analysis (when medial longitudinal compressive strains were maximal). We also examined using the time point at which posterior compressive strains were maximal, but this corresponded to positive (tensile) strains on the medial surface for some birds, further indicating the prevalent variation in the neutral axis position and strain distribution present between the individual birds examined. Although it is reasonable to expect greater variation in measured and predicted strain values in a less controlled mode of mechanical loading, such as locomotion, when compared to the highly controlled *ex vivo* bending we used for the PST validation, we would expect a robust method to be able to account for this type of natural variation and still produce a linear relationship with a near zero intercept. Instead we found non-significant trends that *generally* showed an increase in predicted shear strain with increased measured shear strains, but also included slopes of zero, indicating no relationship between the measured and predicted shear strains. Measures from additional guinea fowl would likely reduce the confidence intervals, perhaps even generating significant trends, which is an important consideration in attempting to evaluate the validity of using this method to predict shear strains in long bone diaphyses.

However, the sample size we used here reflects closely the sample sizes typically used in *in vivo* bone strain studies [24, 102-105]. Therefore, the variation present in this sample should be indicative of that seen in studies that would attempt to apply this methodology for estimating shear strains across a bone's cross-section.

Table 2 clearly shows inter-individual variation in the medial and posterior axial strain magnitudes, which affect the resultant ratio of these strains and consequently our predicted shear strains. There are several possible contributing factors to the variation in strain magnitudes measured in these birds on the posterior and medial bone surfaces. Although we intend to place the gauges at the bone midshaft and centered on each surface, slight differences in gauge placement both around the circumference of the midshaft and/or the proximal-distal position relative to the midshaft were sometimes necessary due to surface limitations, such as bone size and surface features (i.e. unexpected ridges) which caused us to shift gauge placement slightly. The greatest difference in proximal-distal gauge placement between any two birds was only about 13.9mm (-8.1mm to +5.8mm from midshaft), which only amounts to about 4-6% of the bone's length, which is within the variation described in other *in vivo* strain studies [101]. Additionally, slight differences in bone geometry can affect how load is transmitted through the bone and the resultant strain at a given location. Although none of the animals appeared lame while running on the treadmill, slight differences in running kinematics could easily affect the strain distribution throughout the bone as well. A combination of these factors could have contributed to the inter-individual variation in the neutral axis orientation and location across the birds examined, which would significantly impact the calculated longitudinal strain ratios for predicting shear strain. However, regardless of the variation in axial and shear strain measures between animals, the predicted shear strains did not closely match the measured shear strains in most of the animals examined here, especially using the individual-specific multiplier, suggesting that the planar relationship between longitudinal strains does not necessarily correlate linearly to shear strains present in long bones during locomotion, at least for the guinea fowl TBT.

While our results do not indicate a significant relationship between measured and predicted peak shear strains in the guinea fowl TBT it could be argued that a one-to-one relationship between the measured and predicted shear strains also exists within the variation of our data. Similarly, the generally positive (though non-significant) relationships between the measured and predicted shear strains indicate that predicted strains calculated using a longitudinal strain multiplier could increase in relation to increasing measured shear strains. These two results could be used to argue in favor of applying a longitudinal strain multiplier for prediction of shear strains at non-instrumented sites on a bone surface. Extrapolation of measured shear strains to bone sites of maximal longitudinal strains may help to prevent underestimation of maximal shear strains and therefore, artificially inflated safety factor estimates [112, 113]. It is also possible that were this experiment repeated in a different vertebrate taxon, that a more consistent relationship could be determined between the measured and predicted shear strains and that the lack of correlation that we found here could be the result of the variability in bone loading seen in the guinea fowl TBT. In some cases the margin of error that PST-based predictions of shear strains may incur might be acceptable given the goals of a particular study, as long as the investigator recognizes the assumptions made and the uncertainty of the results we have found here in attempting to validate this technique. While we found that a one-to-one relationship could be possible between predicted and measured shear strains in the guinea fowl TBT, the variation within this relationship also indicates that shear strain predictions using a longitudinal strain multiplier could equally over- or under-estimate the true shear strains occurring at a cortical bone location. If one does hope to apply this methodology, we recommend using a sample-mean based average longitudinal strain ratio for estimating shear strains since this resulted in a relationship closer to 1.0 and a somewhat tighter confidence interval for the guinea fowl TBT than using an individual-based strain multiplier. However, if a lower margin of error is desired, one should look towards other methods of assessing bone strains at non-instrumented locations, such as finite element analysis [39, 114, 115].

In conclusion, PST is a robust and accurate method for predicting the distribution of longitudinal bone strains normal to the cross-section and for determining the location of the neutral axis of bending for bones loaded in *ex vivo* bending. Predicted longitudinal strain values closely matched measured values regardless of the distribution of gauges used for the prediction or the strain magnitudes measured. Repeating a similar analysis with strain data collected during *in vivo* locomotion would further validate the use of this method for bones undergoing more complicated loading regimes than the pure bending examined here. Shear strains measured during *in vivo* locomotion, however, could not be accurately predicted in the guinea fowl TBT using longitudinal strain measures. As long as an investigator can accept the potential margin of error present in making shear strain predictions, the method may still have merit for some experiments. However, if more accuracy is desired, alternative methods should be considered. Additional work in several animal species with greater sample sizes would be necessary to attempt to validate a repeatable relationship between longitudinal and shear strain measures in long bones.

Table 2.1 Emu subject data and 4 point bending test parameters

						4-pt Bend Test Parameters				
Animal Number	Age (wks)	Mass (kg)	TBT Length (cm)	TBT AP Diameter (mm)	TBT ML Diameter (mm)	inner span distance (m)	outer span distance (m)	a (m)	Peak Load (N)	Moment Applied (Nm)
A	36	27.4	42	19.4	23.7	0.256	0.452	0.098	-175	-8.58
B	48	30.0	44	21.8	24.9	0.234	0.452	0.109	-175	-9.54
C	74	43.1	43.5	25.8	28.6	0.233	0.460	0.114	-175	-9.93
D	75	50.9	43	24.8	29.2	0.255	0.470	0.108	-175	-9.41
E	75	51.7	43	24.5	27.8	0.200	0.445	0.123	-175	-10.72

Table 2.2 GF subject data and strain gauge positions relative to the bone midshaft

			Gauge Distance from Midshaft (mm) + proximal, - distal		
Animal Number	Mass (kg)	Age (wks)	Anterior	Posterior	Medial
1	2.6	21	-2.0	-3.1	-4.8
2	2.9	21	+4.5	+2.4	+3.8
3	3	21	-1.5	-2.3	-3.9
4	2.8	22	-8.1	-6.4	-6.5
5	2.3	23	+5.8	+2.2	+2.4

Table 2.3 GF longitudinal and shear strains measured during treadmill locomotion, individual-specific longitudinal strain multiplier, and shear strain extrapolations to posterior gauge site for both multipliers

Animal Number	Medial Longitudinal Strain (με)	Posterior Longitudinal Strain (με)	Individual-Specific Posterior/Medial Longitudinal Strain Ratio	Measured Medial shear strain (με)	Measured Posterior Shear Strain (με)	Calculated Posterior Shear Strain – Individual-Specific- (με)	Calculated Posterior Shear Strain – Sample-Mean - (με)
1	-231	-64	0.28	-360	-217	-100	-547
2	-384	-302	0.79	-657	-1000	-518	-1000
3	-51	-271	5.35	-159	-263	-852	-242
4	-27	-33	1.20	-179	-35	-215	-273
5	-153	-616	4.03	-118	-695	-473	-179

Medial and posterior longitudinal and shear strains are experimentally determined values. The individual-specific posterior/medial longitudinal strain multipliers were found by dividing the posterior longitudinal strain value by the medial longitudinal strain value for each animal. A sample-mean multiplier was determined by dividing the mean posterior strain value by the mean medial longitudinal strain value, and for our sample was 1.52. Calculated (extrapolated) posterior shear strains were then determined by multiplying the measured medial shear strain values by the individual-specific and sample-mean multipliers for each bird.

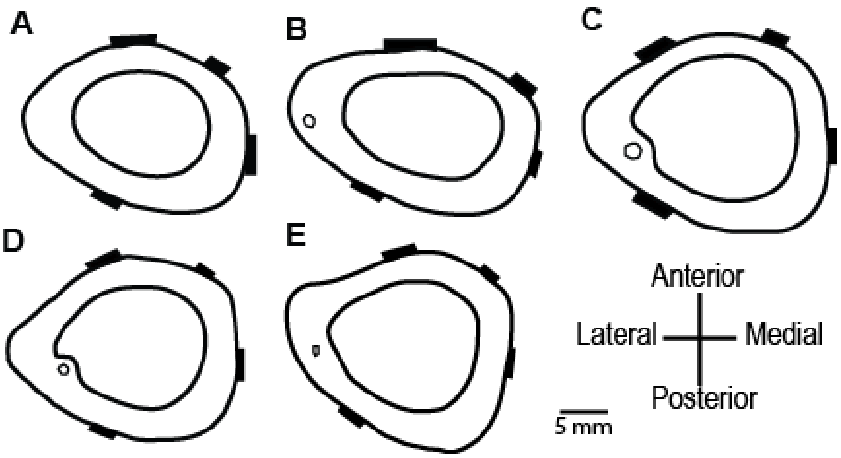

Figure 2.1 Cross sections for each emu TBT included in this study. The strain gauge positions are indicated with black rectangles. Gauge coverage percentage was measured as the distance around the circumference of the gauge for three consecutive gauges used for the prediction (ie for posterior site prediction, circumference between anterior, anterior-medial, and medial gauge locations was measured) over the total circumference.

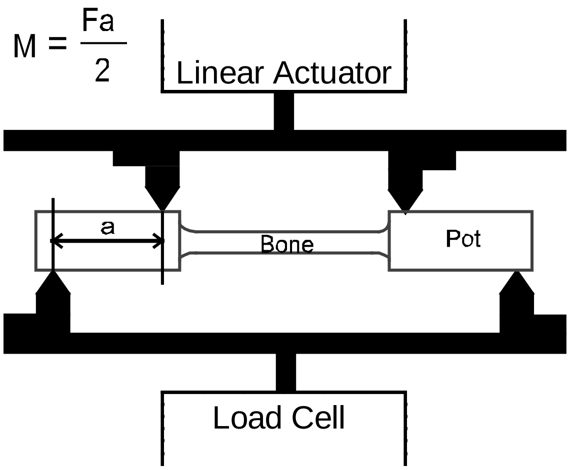

Figure 2.2 Schematic of the four-point bending apparatus. The load points were adjusted horizontally for each bone to maximize the bending moment. The equation shown calculates the bending moment the bone will experience where M is moment, F is the total force applied from the top load points, and ‘a’ is the horizontal distance between the top and bottom load points.

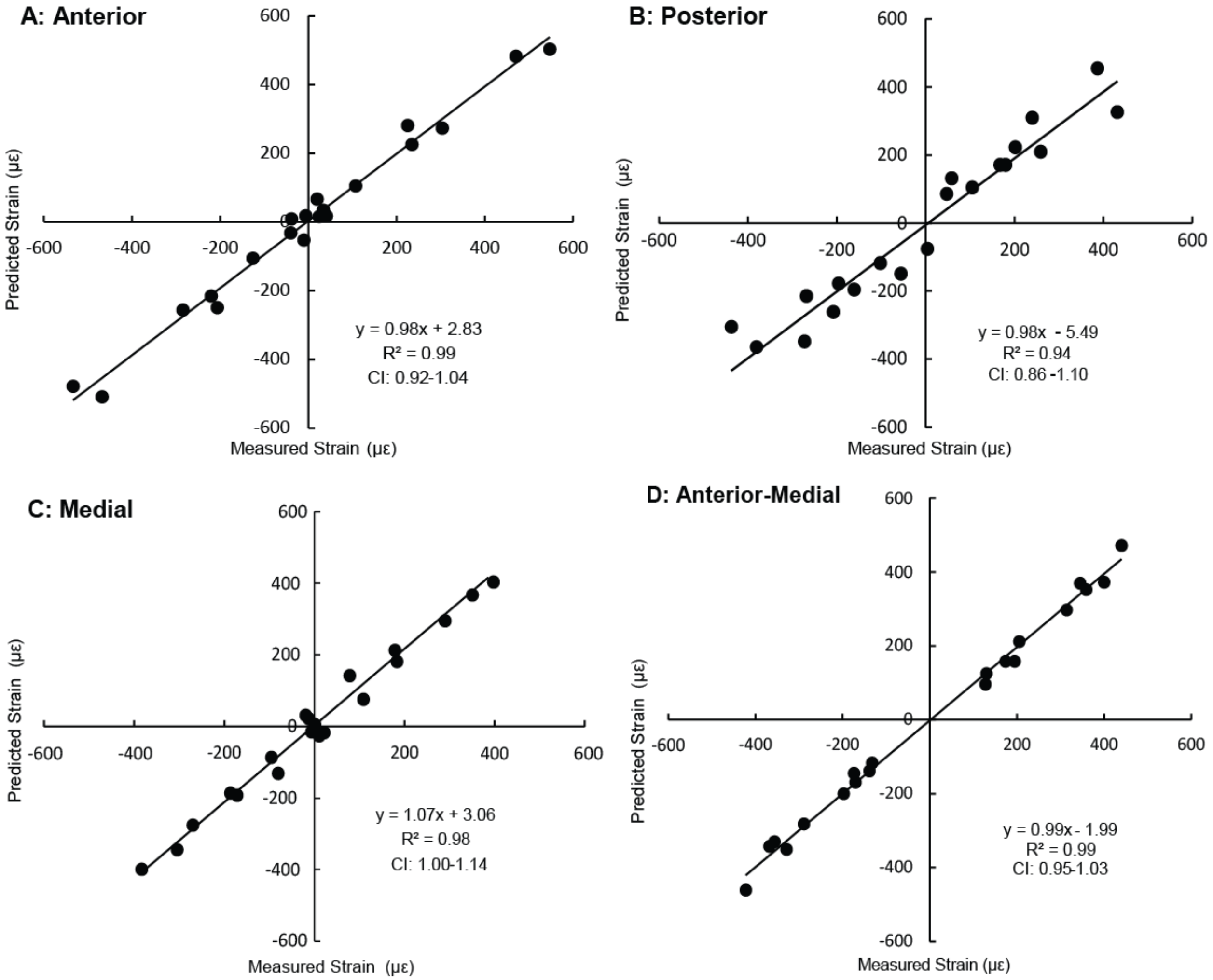

Figure 2.3 Measured versus predicted longitudinal strains (με) for the gauge sites tested. Sites include the (A) anterior gauge site, (B) posterior gauge site, (C) medial gauge site, and (D) anterior-medial gauge site. Each plot contains data from all for bending directions such that, for example, in A, strains would be large and positive or negative during posterior and anterior bending respectively, and close to zero during medial and lateral bending indicating the gauge site was close to the neutral axis. The line through the data represents the linear regression fit.

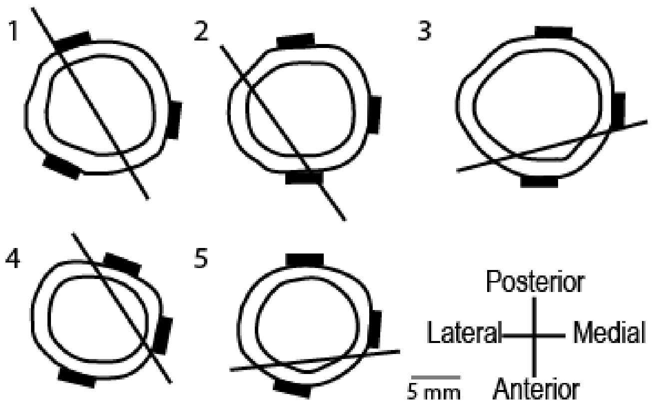

Figure 2.4 Cross sectional strain distributions for each GF TBT included in this study at the time of peak compressive longitudinal strain on the posterior bone surface. The strain gauge positions are represented by black rectangles. The average longitudinal strain values (microstrain) have been included next to the appropriate gauge. The approximate location of the neutral axis for each animal at the time of analysis is indicated on each cross-section.

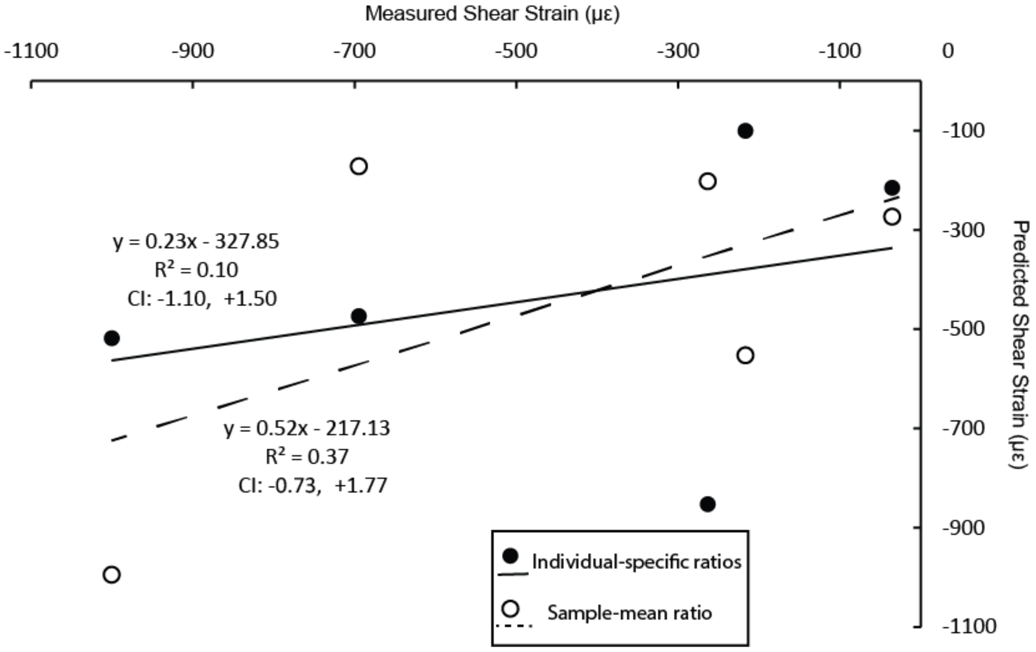

Figure 2.5 Measured versus predicted (extrapolated) shear strain values for each GF for both individual-specific ratios and the sample-mean ratio. The solid and dotted lines represent the linear regression fits for the individual-specific and sample-mean data, respectively, and the slopes, R^2s, and 95% confidence intervals are placed closest to their line in the plot.

[Note: This chapter was published in the Journal of Experimental Biology in 2016. I would like to acknowledge my co-authors Michael Lehner, Luis P. Lamas, and Russell P. Main]

3. CHARACTERIZATION OF THE STRAIN ENVIRONMENT IN THE MOUSE TIBIA AND THE CHUKAR PARTRIDGE TIBIOTARSUS DURING LOCOMOTION AND EXPERIMENTALLY APPLIED MECHANICAL LOADING

3.1 Introduction

Dynamic mechanical loading plays an important role in regulating bone geometry and strength [24, 47, 51, 116-119]. While a healthy skeleton is adapted to the bone tissue strain profile and magnitude of loads it experiences on a daily basis in order to maintain reasonable safety factors [120], when load magnitudes increase, such as in athletes [121-123], or decrease, such as for astronauts in microgravity [10, 124, 125], the affected bones will adapt to the change in stimuli. Although it is unclear if the strain magnitude induced by a given load is the direct stimulus that causes adaptation, it has been established that there is a relationship between strains induced by controlled, experimentally applied loads and the resulting adaptive response [30, 34, 51, 119, 126-129]. Studying bone adaptation using experimental loading models has been essential in determining the sensitivity of bone, as well as the mechanobiological mechanisms responsible for bone modeling and remodeling. Therefore, accurately characterizing the strain environment induced throughout the bone is critical for interpreting the mechanobiological response of the bone to physical stimuli. In addition to knowing what strains are induced in the bone at a given load magnitude, assessing the sensitivity of the bone and relationship between the load stimulus and the adaptive response requires determining the relative increase in strain magnitude between the experimentally applied load and peak physiologic activities to which the bone should be adapted to.

The non-invasive, axial compressive murine tibial loading model has been used extensively to study the skeleton’s response to mechanical load. Since quantifying the stimulus is so important to interpreting the adaptive response, several groups have published independent studies characterizing *in vivo* bone strains during physiologic activities and under experimentally applied loads using strain gauges, digital image correlation, and finite element models [34, 39, 51, 130-133]. Bone size and strength are dependent on several factors including sex [134, 135], age [136, 137], species strain [100], and husbandry conditions [138, 139], and these variations could affect the range of physiologic strains as well as the strains induced by a given load magnitude a bone experiences. Therefore, in order to determine the precise relationship between applied loads and the resulting strain environment, it is important that the strains be characterized during both physiologic activities and under experimental loading conditions on animals similar to those that will be used in future studies. Previous studies have used either female mice or male mice of a different age than we intend to use for future skeletal adaptation studies, both factors that could have significant impact on bone strains.

Sole use of rodent models propagates a large gap in understanding the basic cellular mechanobiological mechanisms responsible for skeletal structural diversity and homeostasis in terrestrial vertebrate groups. Although the skeleton is comprised of the same bone cells and similar material composition, it is extremely diverse across vertebrate species in its morphology, geometry, and mechanical properties. The avian skeleton exhibits several features that make it unique to the mammalian skeleton. Despite evolving from reptilian ancestors, avian species today have a lighter and less metabolically costly skeleton, due to pneumatization of certain bones, making them more similar to derived mammals such as the mouse [91-93]. Yet, avian species are unique compared to vertebrates in that they lay eggs with calcified shells, which involves special regulation of calcium balance hormones and more labile skeletons [96]. Additionally, avian species are uniquely able to form medullary bone, non-structural woven bone on endosteal surfaces, which serves as a calcium reservoir for egg-laying females and experiences varying rates of osteoclastic and osteoblastic activities [96, 97]. The formation of medullary bone can be induced in male birds as well through the administration of estrogen [98]. One of the early animal models employed to study skeletal adaptation was the surgically isolated turkey ulna. Although this model was useful in gaining early insight to the skeleton's sensitivity to dynamic versus static loading [47], axial versus torsional loading [140], the applied number of cycles [50], and the load magnitude [24], the invasiveness and highly non-physiologic strain profile induced [24] have been recognized as significant limitations to the model [141]. Here we take the initial steps to develop a non-invasive, axially compressive avian tibiotarsal (TBT) loading model in which we can begin investigating differences in skeletal sensitivity and response to mechanical load across vertebrate species. Given the novelty of this model, the strain environment during both physiologic activities and under experimental loading conditions was previously unknown.

While strain gauges have been used to measure *in vivo* strains during physiologic activities in a variety of species [24, 26-30, 111, 142, 143] and during experimental loading studies [24, 30, 34, 40, 48], the surfaces of a bone to which they can be attached without disturbing muscle and other soft tissues is often limited. Bone size and surface features also affect the ability to properly instrument a bone. Bone strains measured at instrumented locations are not necessarily the peak bone strains, nor do they correlate with peaks strains at various regions of interest throughout the bone [39]. These limitations make strain gauge measurements alone an inadequate method to characterize a localized adaptive response relative to the induced strain environment. While strain gauges do provide valuable *in vivo* data, high resolution finite element (FE) models provide complementary and more complete assessments of the strain environment throughout the bone [39, 133, 144]. FE models can provide strain predictions on periosteal and endosteal surfaces of the entire diaphysis, as well as trabecular bone regions which are not accessible during *in vivo* conditions.

The intent of this work is to set up the mouse tibial and avian TBT loading models such that in future loading studies we will be able to apply loads that induce similar increases in strain at the midshaft relative to peak strains measured during fast locomotion for these species. Therefore, the objectives of this chapter are to (1) characterize the strain environment in the tibia of the mouse and the TBT of the bird during treadmill running to determine peak physiologic bone strains, (2) determine the relationship between experimentally applied axial compressive loads and the resulting strain environment at the bone midshaft, and (3) develop specimen-specific finite element models that approximate *in vivo* experimental tibial/TBT loading conditions in order to provide more robust characterizations of the whole-bone strain environment for the mouse tibia and the chukar TBT for future applied loading studies.

3.2 Methods

Male mice were obtained at 15 weeks (Jackson Labs, n=8) and housed individually with free access to rodent chow and water until used (16 weeks, mass: 26.8±1.2 g). One mouse was not used for mechanical loading strain data collection due to strain gauge failure between experiments, and two mice were instrumented and used solely for mechanical loading strain data collection. Male chukar partridge were obtained as juveniles from a commercial farm (CM Game Bird Farm & Hatchery, Calais, ME, USA; n=4) and were maintained in an indoor enclosure with free access to game bird feed and water until the they were used in the study (16±2 weeks, mass: 0.44±0.02 kg). All surgical and experimental procedures followed protocols approved by the Purdue University IACUC (PACUC Protocol #1310000977).

3.2.1 Strain Gauge Surgeries

Aseptic surgery was conducted to attach strain gauges to the left tibia of each mouse and the left TBT of each bird. Animals were induced for surgery through mask inhalation of isoflurane (mice: 2%; chukar: 5%), and maintained at a surgical anesthetic plane with 2-4% isoflurane at a 1L/min O_2 flow rate. Breathing and heart rate were monitored throughout surgery, and anesthesia adjusted as necessary. To attach strain gauges to the midshaft of the tibia/TBT, incisions were made on the medial side of the tibia/TBT at the midshaft and the gauges' lead wires were passed subcutaneously from an incision at either the shoulder (mice) or the synsacrum (chukar) to the incision at the tibia/TBT midshaft. Overlying musculature was retracted as necessary to expose the medial surface of the mouse tibia, and the anterior, posterior, and medial surfaces of the chukar TBT. Each surface was prepared for gauge attachment by removing a region of periosteum (mice: 0.05 cm^2; chukar: 0.5-1 cm^2), lightly scraping the underlying surface with a periosteal elevator, and defatting and drying the surface using 2-butanone (Sigma-Aldrich, St. Louis, MO, USA). Strain gauges were then bonded to each site using a self-catalyzing cyanoacrylate adhesive (DURO Superglue, Loctite, Westlake, OH, USA). Mice were instrumented with one single element gauge (EA-06-015LA-120, Micro-measurements, Vishay Precision Group, LTD., Raleigh, NC, USA) on the medial surface, and each bird was instrumented with one rosette gauge (FRA-1-11, Tokyo Sokki Kenkyujo Co., LTD, Tokyo, Japan) on the anterior surface and single element gauges (FLA-1-11, Tokyo Sokki Kenkyujo Co., LTD, Tokyo, Japan) on the medial and posterior surfaces. Gauges were centered on each surface, and the single element or central element of the rosette was aligned with the long axis of the bone within 5°. Once all gauges were bonded to the tibia/TBT, the overlying musculature was carefully replaced as necessary and the incisions overlying the shoulder (mouse) or hip (chukar) and tibia/TBT were sutured (4-0 coated Vicryl violet braided, J392H, ETHICON, Somerville, NJ, USA). The lead wires exiting over the shoulder blades (mice) or synsacrum (chukar) were further anchored to the skin with suture to provide tension relief for the wires, and the incision and the pre-soldered epoxy mounted connector were covered with gauze and elastic bandaging tape. Following surgery, and immediately prior to experimental testing (the following day for the chukar), each animal was given intramuscular injections of analgesic (0.5 mg/kg meloxicam, VETone, Boise, ID, USA).

3.2.2 *In Vivo* Strain Data Collection

In vivo bone strains during treadmill running were collected one hour after surgery for the mice, and 24 hours after surgery for the birds. Once each animal was placed on the treadmill, the strain gauge lead wire connector was connected to a longer shielded cable (mice: 1m; chukar: 5.4m) and the plug-cable connection was further secured to the animal as necessary with additional elastic bandaging tape. The cable was connected to a Vishay bridge amplifier, from which raw strain signals were sampled by an A/D converter at 2000 Hz. Data was collected for 10 second intervals while each animal ran on the treadmill at gradually increasing speeds (mice: 0.18-0.50 m/s; chukar: 0.4-1.34 m/s) with two trials at each speed until each animal reached its peak speed (defined as the highest speed that could be maintained for 10 seconds), while strain data were collected simultaneously.

Immediately following treadmill running, animals were anesthetized and the knee and ankle of the gauged limb were secured in the appropriate custom cups of a mechanical loading device (ElectroForce Testbench, TA Instruments, New Castle, DE, USA) with a preload (mouse: -1N; chukar: -10N). *In vivo* bone strains were collected while the limb was loaded cyclically with a triangular waveform at 4 Hz at incrementally increasing axial compressive loads until maximum longitudinal strain on the medial gauge reached approximately 3-times the maximum strains recorded during locomotion. Strain data were similarly collected at 2000 Hz, and applied load data were simultaneously collected by reading in the applied voltage from the mechanical loading device to the A/D converter using a coaxial cable. Following data collection and while still under anesthesia, mice were euthanized by cervical dislocation and the chukar via intravenous injection of sodium pentobarbital in the brachial vein (320 mg/kg Beuthanasia-D, Schering-Plough Animal Health, Union, NJ, USA). Gauge lead wires were cut, and the tibiae/TBT, with gauges still intact, were carefully dissected, cleaned of all soft tissue, and stored in 70% ethanol at room temperature.

3.2.3 Strain Data Analysis

For treadmill stains, raw strain data for five consecutive, steady strides from both trials at the highest speed each species could maintain (10 total strides per speed per animal) were imported into a custom MATLAB (Mathworks, Natick, MA, USA) program for further analysis. Raw data were filtered using a fourth order Butterworth filter. Zero strain levels were determined by averaging the strains during the entire swing phases of the selected strides. Peak longitudinal strains on all gauged surfaces were determined for single element gauges and from the central element of each rosette gauge. For the birds, filtered strain data from the rosette gauges on the anterior surface were also used to calculate peak principal tensile and compressive strains and the orientation of these strains relative to the long axis of the bone using standard equations that assume a uniaxial planar state of strain [106].

A separate custom MATLAB program was used to calculate peak longitudinal (and principal, when applicable) strains at each applied axial load. Zero strain levels were determined from the strain trace prior to applying the preload to the limb. For the applied loading tests, peak strains were averaged over the final five load cycles at each load magnitude to account for any viscoelastic damping effects that the soft tissue in the knee or ankle may have had on the first half of the applied load cycles. Viscoelastic damping would cause peak strains to occur slightly after the timing of the peak applied load. Linear regression analyses were performed to define the applied load and resulting strain relationship.

3.2.4 Finite Element Modeling

Tibiae/TBT with gauges still attached were scanned in 70% ethanol using microCT (mice: µCT 40, Scanco Medical AG; chukar: Skyscan 1176, Bruker MicroCT, Kontich, Belgium). Any remaining wire and solder leads were carefully removed with a scalpel prior to scanning. Scanning the bone with gauges in place allows the precise location of each gauge to be identified later in the models. For the chukar, the intact knee and ankle joints were positioned in angular configurations similar to that during *in vivo* mechanical loading so that joint contact locations could be determined during modeling. Joint contacts have been previously determined for the mouse in our lab [39], so mouse tibiae were scanned without the femur and metatarsal bone. Bones were scanned with an isotropic voxel resolution of 10 µm (55 kVp, 145 µA, 300 ms integration time, no frame averaging) and 16.81 µm (55 kVp, 455 µA, 224 ms exposure time, no frame averaging) for the mouse and chukar, respectively. An aluminum filter was used to reduce beam hardening effects. MicroCT scanner-specific calibrations were performed using bone phantoms (hydroxyapatite) provided by each manufacturer in order to convert attenuation values to bone mineral density (mg HA/ccm).

Specimen-specific FE models were developed for instrumented bones for the mouse (n=6) and chukar (n=4) using the microCT image stacks. In each image stack containing a whole bone, the gauge(s) were omitted either during the bone contouring (mice, Scanco software), or in ImageJ (NIH) using a black paintbrush (chukar) to prevent the gauge(s) from being rendered as bone during model development. A threshold value was chosen for each species to separate bone and background pixels in their respective scan sets. Three-dimensional FE mesh models with tetrahedral elements were generated using the segmented tibial microCT images for each species and a Matlab-based mesh generation and processing program [145]. Using the grayscale-based bone density values, the modulus of elasticity was assigned to each voxel based upon a published relationship between bone tissue density and isotropic elastic modulus [146]. A poisons ratio of 0.3 was used for all elements [144]. For the mice, contact areas, load application points, and boundary conditions were applied as described previously [39]. Briefly, the contact nodes on the tibial plateau surface were approximated as two ellipses with anterior-posterior and medial-lateral diameters of 0.3 and 0.4 mm, respectively, and rigidly coupled to a reference point approximating the location of patella, at which the compressive load was applied. All nodes on the concave distal articular surface of the tibia were coupled to a distal reference point. Boundary conditions were applied to these reference points such that all translation and rotation was prevented proximally, and only axial translation was allowed distally. For the chukar, load application and boundary conditions were applied similarly to the mouse. Contact areas were determined by assessing joint configurations from the microCT scans with the femur and tarsometatarsus intact. The soft tissue connection between the fibula and tibia for the chukar was modeled separately and given an elastic modulus of 800 MPA, which was between reported maximum elastic moduli values for avian periosteum (230 MPa) [147] and tendon (1479 MPa) [148]. A sensitivity analysis was performed to assess the effect of the elastic moduli of the tibia-fibular soft tissue connection over an order of magnitude on the resulting bone strains measured at the gauge location. An initial proximal reference point location at which load is applied was determined based on the location of patella through which load was applied *in vivo*. This point was then iteratively adjusted by 2mm increments in the anterior-posterior and medial-lateral directions. Modeled strains at the posterior and medial gauge sites were assessed for each reference point location. Ultimately, the reference point location was accepted when the resulting posterior and medial strains had a root mean square error less than 140, which would represent average errors of less than 100με for the modeled strains relative to the measured strains at each location for each model.

Linear elastic finite element analysis was performed in Abaqus 6.13.3 (Simulia, Dassault Systemes, Waltham, MA, USA) for both species to simulate the *in vivo* axial compressive loading. Peak principal strains, defined by the cut-off values for the upper 95th percentile, as well as the average nodal strains, were found for cortical volumes located at 90%, 50%, and 37% of bone length relative to the proximal end of the tibia/TBT. The volume of cortical bone at 37% of bone length relative to the proximal end of the tibia was chosen for additional analyses because it has previously been identified as the site with higher strains and the greatest osteogenic response to axial compressive loading in mice [119]. The volume of cortical bone at 90% of bone length relative to the proximal end of the bone was selected for analyses because of the fractures observed at that location in the chukar TBT when the applied load was increased above -160N during preliminary experiments. An additional volume of cortical bone at 10% of bone length for the chukar only was selected post hoc for analysis because of the high strains indicated in that region of the models as well. Each volume analyzed at these locations captured 2.5% of total bone length. Finally, planar strain analyses were performed using standard equations [107, 149, 150] for the chukar during treadmill running and experimentally applied axial compressive load conditions at the cross-section containing all three gauges in order to compare the strain distributions during each load condition with the modeled strain distribution during axial compression.

3.3 Results

3.3.1 *In Vivo* Bone Strains and Finite Element Model Results for the Mouse Tibia

Mice ran on a treadmill at speeds between 0.18 m/s and 0.5 m/s while strains were measured simultaneously (figure x). The peak speed all mice were able to maintain on the treadmill was

0.5 m/s. The peak longitudinal strain measured at the medial midshaft surface at this speed was 236 ± 61 με (**Figure 3.1**).

To determine the relationship between experimentally applied axial compressive loads and the resulting tibial midshaft strains, incrementally increasing axial compressive loads from –4N to –15N were applied to the mouse hind limb. Longitudinal strains on the medial surface of the tibia increased with increasing applied load. A linear regression determined a relationship between applied load and strain as $y= -84.533x + 73.321$ ($R^2= 0.987$) (**Figure 3.2**). Extrapolation of strain values at the gauge location to incremental load increases determined that the load necessary to induce 2.5x peak strains during treadmill running is -6.5N. Tibial FE models were used assess principal strains at several cortical volumes throughout the diaphysis after their accuracy was verified by matching modeled longitudinal strain values at the gauge location to *in vivo* measured strains (**Table 3.2**). Models were also used to predict principal compressive and tensile strains at 37%, 50%, and 90% of bone length relative to the proximal end of the bone (**Table 3.3**). For the cortical volume at the 37% site, peak principal tensile strains at a 6.5N load were 978 ± 251 με and occurred on the anterior surface of the bone, while the mean principal tensile strains over the volume were 512 ± 129 με. Peak principal compressive strains were -1965 ± 402 με and occurred on the posterior-lateral surface of the bone, and mean principal compressive strains over the volume were -695 ± 154 με. For the cortical volume at 50% of bone length (mid-diaphysis), peak principal tensile strains were 1023 ± 320 με and occurred on the anterior surface of the bone, while the mean principal tensile strains throughout the volume were 452 ± 140 με. Peak principal compressive strains were -1601 ± 449 με and occurred on the posterior surface of the bone, and mean principal compressive strains throughout the volume were -663 ± 168 με. For the cortical volume at 90%, peak principal tensile strains were 291 ± 27 με and occurred on the anterior surface of the bone, while the mean principal tensile strains over the volume were 161 ± 9 με. Peak principal compressive strains were -843 ± 80 με and occurred on the posterior surface of the bone, and mean principal compressive strains throughout the volume were -384 ± 11 με.

3.3.2 *In Vivo* Bone Strains and Finite Element Model Results for the Chukar Partridge TBT

In vivo TBT strains were measured at treadmill belt speeds between 1.8 m/s and 2.3 m/s, but the peak treadmill belt speed all birds could maintain was 2.0 m/s. At this speed, peak longitudinal strains were -438 ± 154με, -397 ± 197με, and 118 ± 119με on the posterior, medial, and anterior TBT midshaft surfaces, respectively (**Table 3.1**, **Figure 3.3**). Although 2.0 m/s was the peak speed all birds reached, strains measured at 1.8 m/s (N=4) and 2.3 m/s (N=2) were not different from those measured at 2.0 m/s. Peak longitudinal strains on the posterior and medial surfaces were compressive, while the peak longitudinal strains on the anterior surface were tensile, indicating that the bone was loaded in a combination of posterior-anterior and medial-lateral bending at the point in stride at which peak strains occurred (**Figure 3.3**). Additionally, principal strains were measured on the anterior midshaft surface of the TBT. Peak principal tensile strains on the anterior surface were 154 ± 120 με, and were oriented at an angle -29° ± 5° from the longitudinal axis of the bone, acting in a proximal-lateral to a distal-medial direction.

The relationship between non-invasive compressive load magnitudes and the resulting midshaft strains in the chukar partridge TBT were previously unknown. To determine the relationship between experimentally applied axial compressive loads and the resulting TBT midshaft strains, incrementally increasing axial compressive loads from –100N to –200N were applied to the chukar TBT [load range chosen based on unpublished preliminary data so that induced strains were similar to or greater than peak physiologic strains during treadmill running]. Longitudinal strains on the posterior and medial midshaft surfaces of the chukar TBT during axial compressive loading increased with increasing applied load. Loads above -150N were not assessed for the entire sample due to concern about bone fracture, so those data were not included in the development of the load:strain relationship. However, above -150N the absolute strains on the medial surface began to decrease (although sample size decreased from n=4 to n=2 at -160N, and to n=1 for load magnitudes of -170N, -185N, and -200N due to concern for fracture failure). Although posterior strains continued to increase linearly after -150N, medial strains decreased. The decrease in strain magnitude could indicate that some shift in joint orientation and contact points changed above a certain load magnitude, resulting in an altered strain profile for that bird. A linear regression over the load range from -100 to -150N described a relationship between applied load and strain for the posterior surface as $y= 8.05x + 446$ (R^2= 0.95) (**Figure 3.4**). For the medial surface, the linear regression relationship between applied load and midshaft strain was $y=4.99x – 345$ (R^2= 0.81) between loads of -100N and -150N. Planar strain analyses were used to determine the similarity between cross-sectional strain distributions during treadmill running and experimental loading. The neutral axis rotated slightly from representing primarily antero-posterior bending, so a combination of medio-lateral and antero-posterior bending, relocating peak strains from the posterior surface to between the posterior and medial surfaces of the cross-section (**Figure 3.7**).

Finite element models for the chukar TBT were validated for n=3 out of 4 bones. Bird 1's root mean square error was 431, although the majority of this error came from the posterior surface, which under the modeled conditions, estimated posterior strains to be approximately 400 $\mu\varepsilon$ higher in magnitude than what was measured *in vivo*. On the medial surface, measured and modeled strains had a difference of less than 50$\mu\varepsilon$ (**Table 3.4**). During the sensitivity analysis, moving the reference point 1 and 2 mm in the anterior direction did reduce the error, however this location was on the anterior edge of the cnemial crest of the TBT, considerably different from the other three models. Root mean square error was less than 140 for the remaining three birds, indicating strong agreement between modeled strains at the medial and posterior gauge locations compared to *in vivo* measurements (**Table 3.5**). Anterior strains were not considered during model validation due to the low magnitude and considerable variability in *in vivo* strains measured on that surface. Results from Bird 1's model were ultimately included due to the good agreement on the medial surface. Sensitivity analyses of the elastic modulus for the soft tissue connection between the fibula and tibia showed no effect on tibial strains over an order of magnitude change, so a value of 800 MPA was accepted.

Chukar TBT FE models were used to assess principal strains in cortical volumes throughout the diaphysis (**Figure 3.6**). An applied load level of -130N was chosen after preliminary *in vivo* loading studies employing higher loads (as low as -160N) caused several TBT's to fracture after one to three days of cyclic loading (data not included). At -130N, strains at the posterior and medial gauge locations were about 1.6x and 2.3x higher, respectively, than peak strains measured during treadmill running (**Table 3.7**). Models were used to predict principal compressive and tensile strains at 10%, 37%, 50%, and 90% of bone length relative to the proximal end of the bone for this load of -130N. For the cortical volume at the 10% site, peak principal tensile strains were 1625 ± 800 $\mu\varepsilon$ and occurred on the anterior surface of the bone, while the mean principal tensile strains over the volume were 756 ± 141 $\mu\varepsilon$. Peak principal compressive strains were -3059 ± 1133 $\mu\varepsilon$ and occurred on the posterior-lateral surface of the bone, and mean principal compressive strains over the volume were -1271 ± 221 $\mu\varepsilon$. For the cortical volume at the 37% site, peak principal tensile strains were 303 ± 78 $\mu\varepsilon$ and occurred on the anterior surface of the bone, while the mean principal tensile strains over the volume were 193 ± 36 με. Peak principal compressive strains were -955 ± 239 με and occurred on the posterior-medial surface of the bone, and mean principal compressive strains over the volume were -519 ± 41 με. For the cortical volume at the 50% site, peak principal tensile strains were 364 ± 125 με and occurred on the anterior surface of the bone, while the mean principal tensile strains over the volume were 219 ± 86 με. Peak principal compressive strains were -1157 ± 377 με and occurred on the posterior-medial surface of the bone, and mean principal compressive strains over the volume were -584 ± 91 με. For the cortical volume at the 90% site, peak principal tensile strains were 831 ± 142 με and occurred on the posterior surface of the bone, while the mean principal tensile strains over the volume were 429 ± 59 με. Peak principal compressive strains were -2006 ± 377 με and occurred on the anterior surface of the bone, and mean principal compressive strains over the volume were -887 ± 169 με.

3.4 Discussion

In this study, we developed the relationship between peak bone strains *in vivo* during experimental loading conditions relative to strains that occur during physiologic activity such that futures studies will be able to assess skeletal sensitivity across these two vertebrate species, the mouse and chukar partridge. *In vivo* strain gauge data were complemented with specimen-specific finite element models for both species in order characterize whole bone strains. Additionally, because we were able to instrument the chukar TBT with three gauges for *in vivo* strain measurements, we were able to use planar strain analyses to make novel assessments regarding the similarity of cross-sectional strain distributions that occur during treadmill running and experimentally applied loads.

3.4.1 Development of the Chukar TBT finite element models

Specimen-specific chukar TBT finite element models were developed and validated using the instrumented bones from the *in vivo* strain experiments. The models were developed similarly to the mouse models, which have previously undergone significant sensitivity analyses to assess the effect of features such as scan resolution, bone threshold, mesh refinement, tissue heterogeneity, fibula inclusion, and reference point location [39]. Of those analyses, the only parameters shown to strongly influence model outcome were tissue heterogeneity, fibula inclusion, and reference point location. Sensitivity analyses to assess the effect of homogenous versus heterogeneous bone tissue moduli on results were not performed for the chukar models because previous studies have shown heterogeneous models to be more accurate. We used the same mathematical relationship to relate bone tissue mineral density and elastic modulus for both the mouse and chukar, rather than developing species-specific values through mechanical testing, because the relationship used here was determined through testing a comprehensive sample of vertebrate species [146], and its use has resulted in models for both species that strongly agree with *in vivo* measurements. We did include the fibula in our chukar models as there appeared to be substantial articular contact between the lateral condyle of the femur and the proximal fibula. Our sensitivity analysis showed that a range of connective tissue mechanical properties over an order of magnitude did not affect the resulting TBT strains at the medial and posterior gauges, so it seems that for the chukar, the fibula may not have as strong of an impact on TBT strains during axial compressive loading compared to the mouse tibia under similar loading conditions. Proximal reference point location was important for the chukar as well, and was chosen through iterative adjustments until the root mean square error was below 140, indicating mean errors less than 100με for the posterior and medial surfaces.

3.4.2 Tibial strains for the mouse during experimental loading relative to locomotion

Peak strains measured at the medial midshaft of the mouse tibia during treadmill running were tensile with a magnitude of about 230 με. Longitudinal strains on the medial surface of the mouse tibia did not increase significantly with increased treadmill belt speeds, despite previous studies in other species that have shown that bone strains do typically change with speed [29, 142, 151]. One previous study using inverse dynamics and finite element models predicted that the mouse tibia is loaded primarily in antero-posterior bending during locomotion [152], which would mean that our gauge on the medial surface was likely located near the neutral axis of bending. Higher strain magnitudes likely did occur on posterior and anterior surfaces during locomotion, even though medial surface strains did not change much. The location of the neutral axis may cause medial midshaft strains to be a poor representative of what happens on other surfaces of the bone during locomotion, however, measuring strain *in vivo* on posterior or anterior surfaces is not possible due to bone geometry. Longitudinal medial midshaft strains were similar to what has been reported previously for the mouse during locomotion, although strains reported during jumping were even greater than what have been measured during locomotion [34], which suggests that strains during fast locomotion may not represent the highest strains the bone experiences.

Murine tibial medial midshaft strains were tensile and increased linearly up to 1200με in response to experimentally applied axial compressive loads between -4N to -15N. Peak longitudinal strains on the medial midshaft surface were tensile, similar to the peak strains measured during treadmill locomotion for the mouse tibia. Finite element models of the mouse tibia showed that at the midshaft, the bone is loaded primarily in antero-posterior bending, such that peak strains actually occur on the posterior surface at the midshaft and the neutral axis of bending does cross through the medial surface of the bone. Based on the longitudinal strain distribution throughout the whole bone though, antero-posterior bending shifts towards medial-lateral bending as you move proximally and distally from the midshaft due to the curvature and geometry of the bone during experimentally applied axial compressive loads. Of our three regions of interest, the highest strain magnitude was compressive and occurred at the 37% volume of interest. Despite higher compressive strains at the 37% site compared to the midshaft, peak principal tensile strains were similar at both locations, likely due to the difference in cortical cross-sectional geometry and resulting strain distribution between the two diaphyseal regions of the bone. Peak principal compressive and tensile strains during a -6.5N load were 2-3x higher at the midshaft and 2-4x higher at 37% than peak longitudinal strains measured at the gauge location during treadmill locomotion. Peak strains at 90% of bone length were compressive, but their magnitudes were half as high as those predicted at the midshaft. Finite element strain distributions did not indicate any additional areas along the tibial diaphysis where strains were higher than the areas previously recognized. The mouse tibia could only be instrumented with one, single element strain gauge at the midshaft, which prevented *in vivo* assessments of principal strains as well as planar strain analyses, which could have determined the degree of similarity in the cross-sectional strain distribution between treadmill locomotion and experimentally applied loading. Although, based on the aforementioned predictions of *in vivo* strain distribution during locomotion for the mouse tibia [152], the two loading scenarios do cause similar strain profiles.

3.4.3 Chukar Partridge Tibiotarsal strains during experimental loading relative to locomotion

For the chukar, we were able to measure strains on three surfaces at the TBT midshaft during treadmill running and experimental loading conditions, which provides a more comprehensive understanding of the induced strain profile during various mechanical loading scenarios than is possible using the mouse tibia. During treadmill locomotion, longitudinal strains on the posterior and medial midshaft surfaces where compressive, while strains on the anterior surface were tensile, indicating that during peak loading the chukar TBT experiences a combination of anterior-posterior and medial-lateral bending. Although the peak principal strains on the anterior surface are lower than what has been reported previously for the emu [142] and chicken TBTs [25, 153], the angle of principal tension is similar to what was reported for those species, as well as the guinea fowl during level locomotion (unpublished data collected by author), indicating that torsional loading may be a consistent component of the loading profile on the anterior midshaft of the avian TBT. The posterior and medial surfaces of the chukar TBT could only be instrumented with single element strain gauges due to surface size, so we cannot comment on off-axis strain components on those surfaces. Only peak principal strains have been reported for the posterior and medial surfaces of the TBT for other avian species, however the principal strains for the emu [142] and chicken [25, 153] were larger than the longitudinal strains we report for the chukar. It is possible that since we only had single element gauges on the medial and posterior surfaces, we could not measure additional components of the strain field that could potentially contribute to significant increases in TBT strain. Torsion did occur on the posterior and medial surfaces of the emu TBT, therefore off-axis strains had an influence on principal strains. Due to the similarities of torsional loading on the anterior surface between the chukar, emu, chicken, and guinea fowl, it seems possible that torsional loading might also be similar on the other surfaces, which would suggest that principal strains may be higher than the longitudinal strains that we were able to measure for the posterior and medial surfaces of the chukar TBT during locomotion. Regardless, relative differences in strain between the avian species could also be associated with differences in animal size [25], genetic background [154], and specific husbandry conditions during growth [153, 155].

The chukar TBT models showed that, unlike the mouse, peak strains occur at the proximal and distal metaphyses when the bone is loaded in axial compression. The highest principal strains occurred at the 10% site on the postero-lateral edge of the cross-section, and were approximately -3000με (figure x). The volume with the lowest principal strains was at 37% of bone length, although peak strains at the midshaft were only 200με higher in magnitude. Overall, the models demonstrated that peak strains in the avian TBT do not occur at or near the midshaft during axial compressive loading, and can be 2-3x higher at other locations on the bone. At the midshaft, axial compressive loads induced peak strains on both the posterior and medial surfaces that were compressive. On the posterior and medial gauged surfaces, peak longitudinal strains induced by a -130N load were 1.2x and 2.5x higher, respectively, than peak longitudinal strains measured at those respective gauge locations during treadmill locomotion.

Planar strain analysis of the cortical cross-section at the gauge locations shows that there is a slight shift in neutral axis orientation between the peak strain profiles during treadmill running compared to axial compressive loading. At the time in stride of peak strains during treadmill running, the bone is loaded in antero-posterior bending, with the greatest strain magnitudes occurring on the posterior and anterior surfaces, while the medial surface is near the neutral axis. During axial compressive loading, the neutral axis shifts due to similarly high magnitudes of compression on the medial and posterior surfaces, while the anterior and lateral surfaces are under low magnitude tension. The shift in the neutral axis between treadmill running and experimental loading is likely what makes it possible to induce a larger strain differential on the medial surface compared to the posterior surface. In addition to bending loads, principal strain angles during treadmill running indicated that the chukar TBT is also loaded in torsion, which is an aspect of physiologic loading we are not able to recreate experimentally. While it is unclear what effect the lack of torsional load component during experimental loading may have on skeletal sensitivity, a previous study did demonstrate that torsional loads alone were not anabolic to the avian skeleton [140]. Previous studies have shown that the necessary strain stimuli to induce a response may be relative to the change in strain profile between physiologic loading activities and the experimentally applied load [24, 34, 156], so these differences between loading scenarios should be taken into consideration when assessing the skeletal response to a given experimental load during future studies. Relative changes in strain profile could affect the strain threshold necessary to cause an adaptive response.

The chukar TBT FE models helped to elucidate why attempts to increase strains at the midshaft using higher load magnitudes during *in vivo* preliminary testing caused fracture failure to occur at approximately 90% of bone length in several animals. Fracture failure was observed in multiple birds at loads of either -200N, -180N, or -160N after 1, 3, and almost 14 days of loading, respectively. With 216 cycles applied daily, the two highest loads caused fracture in less than 700 total cycles, and the third load level caused fracture after approximately 2100 cycles. If strains at 90% of bone length are assumed to increase linearly, the 95th percentile of peak strains would be about -3000 με during a -200N load, which is less than yield and failure strains previously reported for cortical bone in longitudinal compression [106, 107]. Although we use the cut-off values for the upper 95th percentile for strains in each volume to represent peak strains, small areas of locally higher strains do occur in that region, likely due to stress concentrations related to the supratendinal bridge. Based on the models, local maximum strains could be as high as approximately -15,000 με at loads of -200N, which is above the yield strain range and within the range of strains previously reported to cause fracture failure. Between the high local strain values and the increasing number of cycles required to cause fracture with decreasing load, it is likely that fracture failure resulted from a combination of high strains and low cycle fatigue. Peak strains in the TBT during locomotion may occur at sites distant to the midshaft, so our assessment of peak strains *in vivo* may not represent the highest strains the chukar TBT experiences during normal activities. Although it is of interest to assess the response of the bone to a specific increase in strain, which we can do near the midshaft, we cannot assess strains *in vivo* at locations such as the 10% and the 90% sites due to bone geometry and muscle attachments. Ultimately, it may be more feasible to assess the adaptive response relative to the absolute strain stimuli predicted by the models at the various regions of the TBT rather than relative to peak strains measured during physiologic activities.

3.4.4 Strain profile comparisons between the Mouse Tibia and Chukar TBT

The differences in shape between the mouse tibia and the chukar TBT cause axial compressive loading to induce fairly different strain profiles throughout the whole bones. The mouse tibia has a substantial amount of curvature between the tibia-fibular junction (TFJ) and the proximal epiphysis of the bone. Axial compressive loads cause bending to occur in that region, as evidenced by the compressive strains on the posterior surface and the tensile strains on the anterior surface. Alternatively, the chukar TBT has a relatively straight diaphysis, with the most significant curvatures occurring at the proximal and distal metaphyses. When loaded in axial compression, FEA models show that the diaphysis of the chukar TBT is loaded almost entirely in compression. Peak strains in the bone were compressive and estimated to occur on the postero-lateral surface of the proximal metaphysis and the anterior surface of the distal metaphysis. The volume at 50% is used frequently in the mouse model, but it is not necessarily the location of peak strains during axial compression for either species. Although future loading studies will be designed to assess the sensitivity of each skeleton to similar relative increases in strain, comparing the magnitude of those peak strains induced is interesting as well. Based on our models, the cortical bone volumes with the most similar peak principal strains during experimentally applied axial compressive loading in the two species were the 37% site for the mouse, and the 90% site for the chukar. At the midshaft, peak principal compressive and tensile strains for the chukar were approximately 400με and 600με lower in magnitude, respectively, compared to the mouse, which constitutes large percentages of the peak values. There is still significant debate in the field over whether an adaptive response is triggered by absolute strain magnitudes or relative strain increases, so knowing both will help when interpreting future loading study results.

Although comparisons across species would ideally be made at similar locations on the bone using experimentally applied loads that induce similar increases in strain relative to peak physiological strains (during activities such as high speed locomotion), differences in bone shape and size have significant impact on the resulting strain profile. Reaching similarly high strain magnitudes on midshaft surfaces of the mouse and chukar bones was not possible because although peak strains did occur near the midshaft for the mouse, they occurred near the proximal and distal epiphyses for the chukar, such that further increasing the load caused fracture failure to occur distally. Querying the strain profile at similar bone locations in multiple species, such as the mouse and chukar, is interesting for comparative load induced strain assessments, but ultimately making assessments about the sensitivity of the bone to relatively similar strain stimuli may require choosing species-specific volumes of interest.

Table 3.1 Peak strains for the chukar TBT midshaft during treadmill running at 2.01 m/s. Longitudinal strains are reported for all surfaces, while principal tension (E1) and its angle (φ1) relative to the long axis of the bone are reported only for the anterior surface. For each animal, data is presented as mean ± one standard deviation.

Animal Number	**Posterior**	**Medial**	**Anterior**		
	με	με	E1, με	φ1	με
1	-217 ± 14	-235 ± 28	120 ± 18	-33	112 ± 19
2	-502 ± 39	-620 ± 43	57 ± 17	-33	39 ± 20
3	-573 ± 102	-226 ± 56	328 ± 78	-27	289 ± 78
4	-458 ± 37	-505 ± 45	109 ± 17	-23	33 ± 13
Average	-438	-397	154	-29	118
Std. Dev	154	197	120	5	119

Table 3.2 Extrapolation of longitudinal strain measures (με) at the gauge to incrementally increasing applied axial compressive load levels (N) based on finite element models for the mouse tibia.

Load (N)	1	4	5	6	6.5	7	8
Gauge Strain (με)	92	367	459	551	590	643	735

Table 3.3 Peak and mean principal strains determined by finite element analysis for a -6.5N compressive load for cortical cross-sections at 37%, 50%, and 90% of bone length relative to the proximal end of the mouse tibia. Values represent mean (n=6) ± one standard deviation.

Cortical Cross-Section Strains				
		37%	50%	90%
Principal Tension	95% percentile	978 ± 251	1023 ± 320	291 ± 27
	Mean	512 ± 129	452 ± 140	161 ± 9
Principal Compression	95% percentile	-1965 ± 402	-1601 ± 449	-843 ± 80
	Mean	-695 ± 154	-663 ± 168	-384 ± 11

Table 3.4 Sensitivity analysis for the proximal reference point location for the chukar FE models. An initial location was chosen, then adjusted 2mm in the anterior (A) or posterior (P) direction and 2mm in the medial (M) or lateral (L) direction. Mean longitudinal strains at the posterior, medial and anterior gauge sites were assessed under each condition. Additional assessments were made 1mm in specific directions dependent on the results of the error assessment (Table 3.5).

Posterior

Animal #	In Vivo Strains (με)	Modeled Strains	+2 A-P	+1 A-P	-2 A-P	+2 M-L	+1 M-L	-2 M-L
1	-385	-802	-286	-542	-1298	-520		-1060
2	-556	-587	-123		-1089	-451	-526	-756
3	-726	-757	-195		-1319	-816		-699
4	-607	-663	-128		-1210	-372		-963

Medial

Animal #	In Vivo Strains (με)	Modeled Strains	+2 A-P	+1 A-P	-2 A-P	+2 M-L	+1 M-L	-2 M-L
1	-637	-705	-422	-560	-955	-1185		-195
2	-1413	-1246	-1084		-1370	-1784	-1509	-675
3	-807	-853	-803		-900	-1348		-356
4	-985	-884	-669		-1078	-1405		-340

Anterior

Animal #	In Vivo Strains (με)	Modeled Strains	+2 A-P	+1 A-P	-2 A-P	+2 M-L	+1 M-L	-2 M-L
1	265	-194	-790	-505	441	-123		-229
2	46	14	-638		675	250	133	-215
3	197	-103	-252		469	-531		-426
4	15	-158	-868		578	-123		-171

Table 3.5 Root square mean evaluation of the error between the in vivo measured strains and the predicted strains in the FE models for the posterior and medial gauges at each reference point location.

Error assessment for posterior and medial gauges

Animal #	Modeled Strains	+2 A-P	+1 A-P	-2 A-P	+2 M-L	+1 M-L	-2 M-L
1	423	237	175	967	564		807
2	170	544		535	386	101	765
3	55	531		600	548		452
4	115	574		610	481		737

Table 3.6 Extrapolation of longitudinal strain measures (με) at the posterior and medial gauges to incrementally increasing applied axial compressive load levels (N) based on finite element models for the chukar TBT.

Load: Gauge Strain Extrapolations								
Load (N)	-1	-100	-110	-120	-130	-140	-150	-160
Posterior Gauge Strain (με)	-5	-540	-594	-648	-702	-756	-810	-864
Medial Gauge Strain (με)	-7	-709	-780	-851	-922	-993	-1064	-1135

Table 3.7 Peak and mean principal strains determined by finite element analysis for a -130N compressive load for cortical cross-sections at 10%, 37%, 50%, and 90% of bone length relative to the proximal end of the chukar TBT. Volumes representing 2.5% of bone length were assessed at each site. Values represent mean (n=4) ± one standard deviation

		10%	**37%**	**50%**	**90%**
Principal Compression	95%	-3059.25 ± 1133	-955 ± 239	-1157.75 ± 377	-2006.5 ± 377
	Mean	-1271.75 ± 221	-519 ± 41	-584.75 ± 91	-887.5 ± 169
Principal Tension	95%	1625.75 ± 800	303.75 ± 78	364.25 ± 125	831.75 ± 142
	Mean	756.25 ± 141	193.5 ± 36	219.75 ± 86	429.75 ± 59

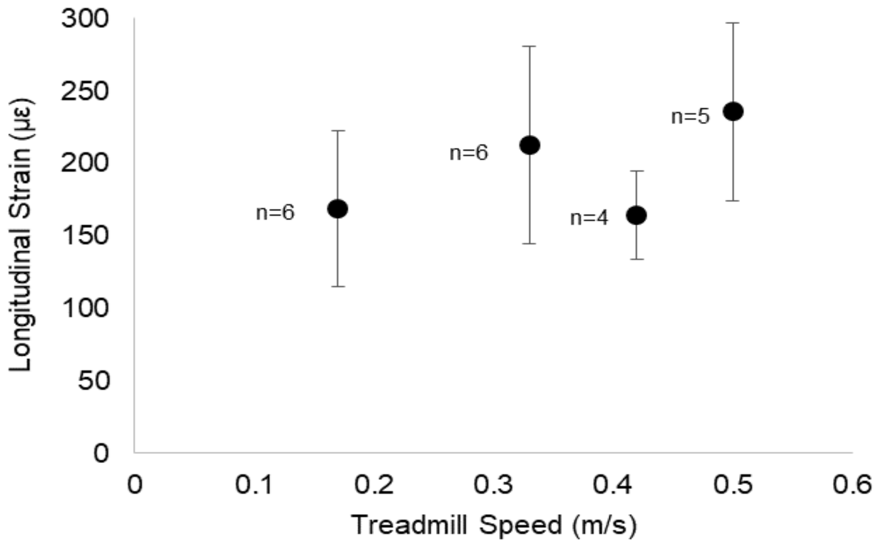

Figure 3.1 Mean peak longitudinal strains at the medial midshaft of the mouse tibia during treadmill running.Error bars represent ± one standard deviation. The sample size at each speed is indicated adjacent to the data point.

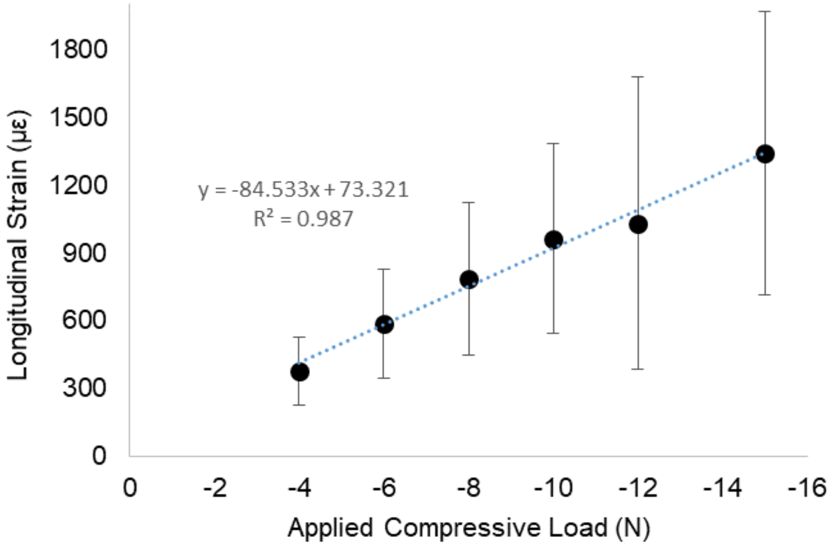

Figure 3.2 Mean peak longitudinal strains at the medial midshaft of the mouse tibia during axial compressive applied mechanical loading (n=7). Error bars represent ± one standard deviation.

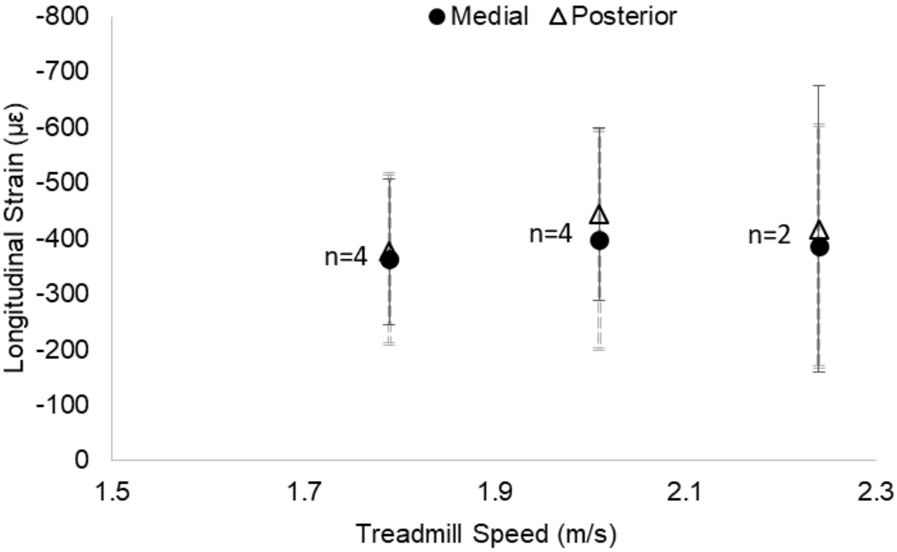

Figure 3.3 Mean peak longitudinal strains on the medial and posterior surfaces of the chukar TBT during treadmill running at the highest speeds achieved. Error bars represent ± one standard deviation. Note that the x-axis starts at 1.5 m/s rather than 0. The grey dashed error bar is for the medial surface while the black solid error bar is for the posterior surface. The sample size at each speed is indicated next to the data points and applies to both surfaces.

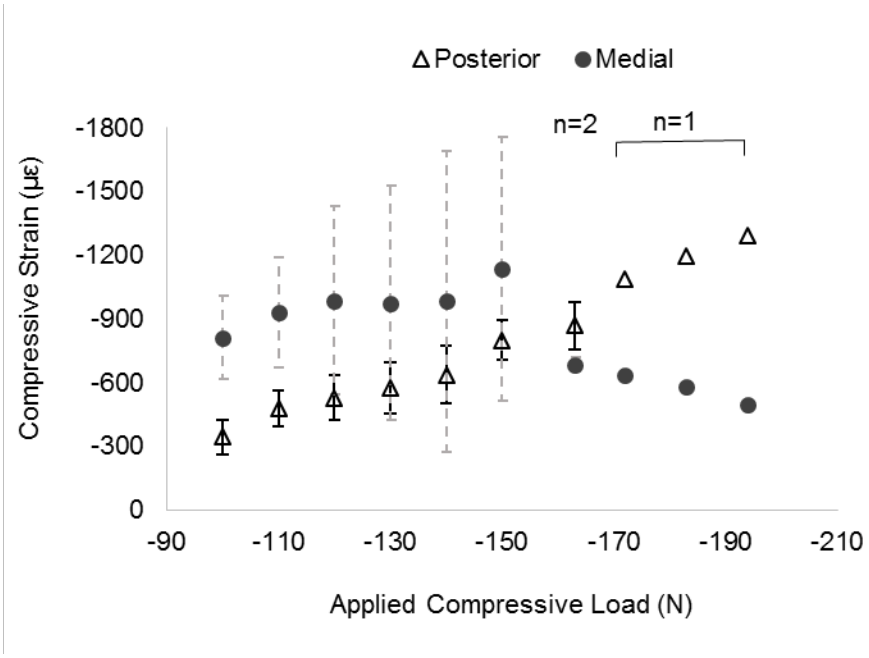

Figure 3.4 Mean peak longitudinal strains on the posterior and medial midshaft surfaces of the chukar TBT during axial compressive applied mechanical loading. Data is from n=4 animals unless otherwise noted. Note that the x-axis begins at -90N rather than 0. Error bars represent ± one standard deviation. The grey dashed error bar is for the medial surface while the black solid error bar is for the posterior surface.

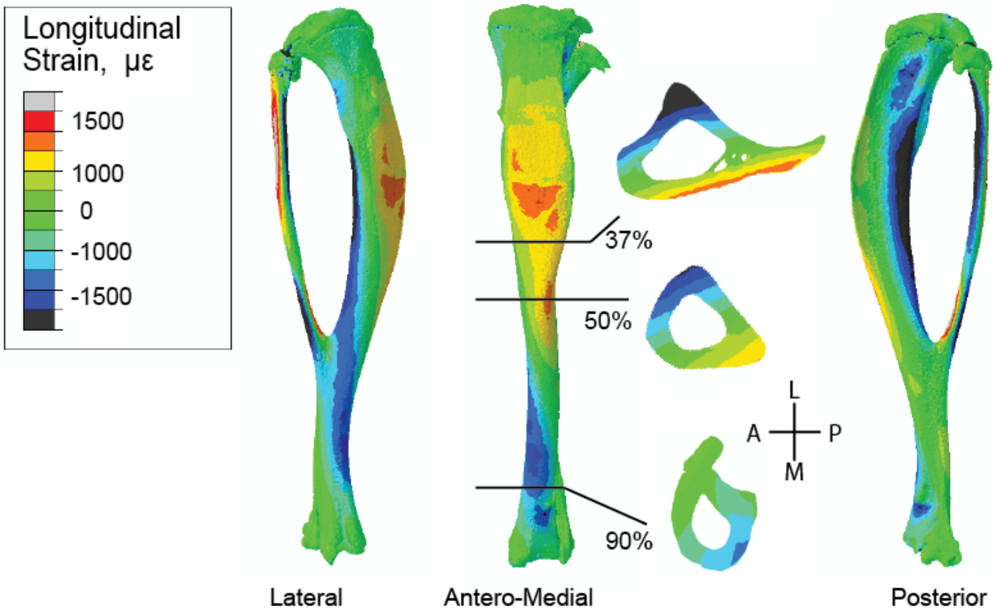

Figure 3.5 Representative finite element modeling of the longitudinal strain (με) profile for the mouse tibia during axial compressive loading at -6.5N. Images show the lateral, antero-medial, and posterior surfaces of the whole bone from left to right. Cross-sectional strain distributions at 37%, 50%, and 90% relative to the proximal end of the bone are shown as well.

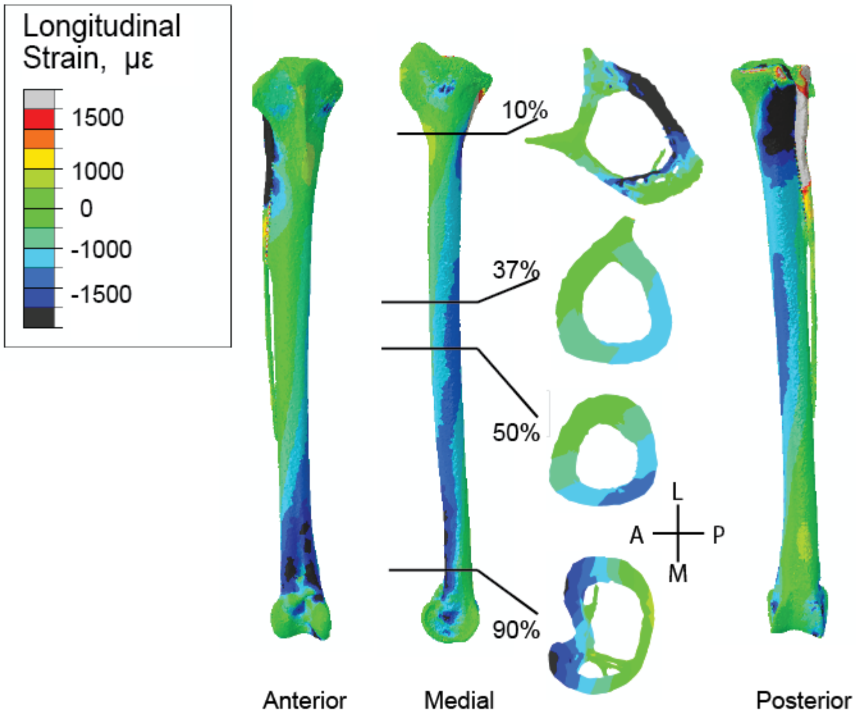

Figure 3.6 Representative finite element modeling of the longitudinal strain (με) profile for the chukar TBT during axial compressive loading at -130N. Images show the Anterior, medial, and posterior surfaces of the whole bone from left to right. Cross-sectional strain distributions at 10%, 37%, 50%, and 90% relative to the proximal end of the bone are shown as well.

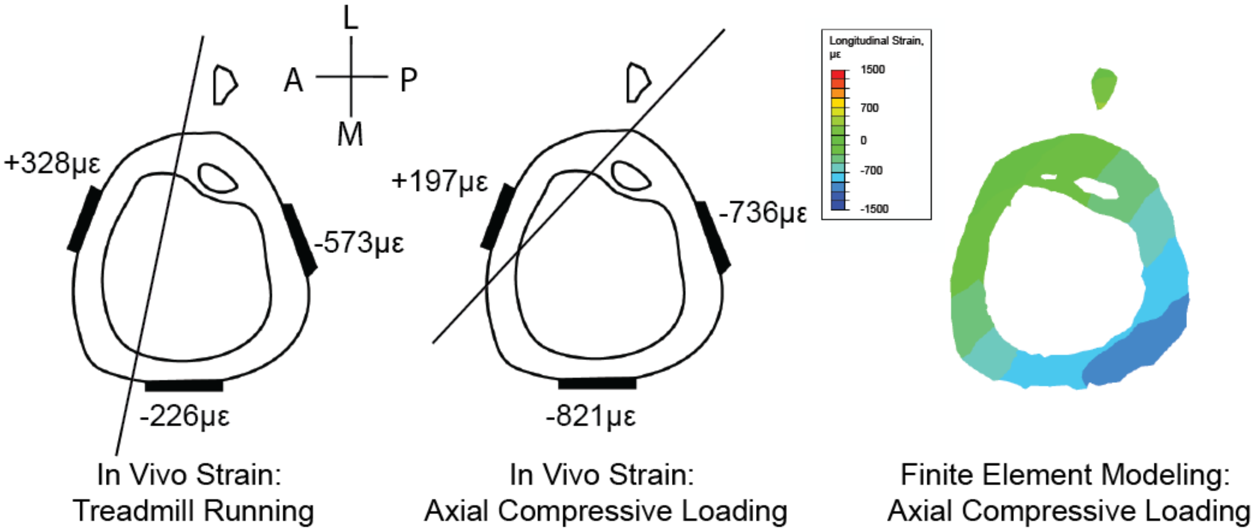

In Vivo Strain: Treadmill Running

In Vivo Strain: Axial Compressive Loading

Finite Element Modeling: Axial Compressive Loading

Figure 3.7 Representative cross-sectional longitudinal strain distributions during treadmill running (left), experimentally applied axial compressive loading (center), and finite element modeling of experimentally applied axial compressive loading (right). Data from bird 3 was used for all cross sections, and the values next to each gauge represent the mean measured values for each gauge. For axial compression loading figures, the data is shown for a -130N load. The solid line represents the location and orientation of the neutral axis for each condition.

4. COMPARATIVE ASSESSMENT OF THE SKELETAL RESPONSE TO EXPERIMENTALLY APPLIED MECHANICAL LOADING BETWEEN THE MOUSE AND CHUKAR PARTRIDGE

4.1 Introduction

Bone mass, geometry, and strength are regulated by mechanical load. However, all of the studies done using non-invasive, experimentally applied mechanical loads have employed rodent models [34, 40, 48, 157]. Use of these models has provided significant insight into the many variables of a load stimulus that the skeleton is sensitive to, such as load magnitude [129, 158], load rate [116], frequency [54, 56], and cycle number [50, 129], in addition to the effects of age [59, 60, 132] and sex [58, 159]. Rodent models have been key in developing the concepts of the pre-adapted strain range or “lazy zone,” and the minimum effective strain (MES) stimulus, where above that stimulus there is a linear relationship between the applied load and the resulting increase in bone volume relative to non-loaded control bones [51]. They have also helped to provide insight to the genetic and cellular level mechanisms involved in bone adaptation [68, 80, 160-162]. However, it is known that the skeleton of small rodents does not undergo haversian remodeling similar to larger vertebrates [163], including humans, and it is unknown how mechanobiological processes involved in modeling and remodeling may differ because of it. Also, the small size of the murine skeleton, the most commonly used rodent model, limits the ability to experimentally characterize the strain profile *in vivo* under various loading conditions, which is important for interpreting the skeleton’s response to a specific stimulus.

Despite the insights made regarding skeletal adaptation using rodent models, there have been no direct attempts to compare skeletal plasticity across vertebrate species. Studies have shown that there is significant diversity in skeletal morphology, geometry, and mechanical properties across various vertebrate groups [164], yet direct comparisons of the sensitivity and adaptive response of the skeleton between vertebrate species have not been evaluated. The avian skeleton, in particular, exhibits several features that make it unique to the mammalian skeleton. Despite evolving from reptilian ancestors, avian species today have a lighter and less metabolically costly skeleton, due to pneumatization of certain bones, making them more similar to derived mammals such as the mouse [91-93]. Avian species are also differ from most vertebrates in that they lay eggs with calcified shells, which involves special regulation of calcium balance hormones and more labile skeletons [96]. Additionally, avian species are uniquely able to form medullary bone, non-structural woven bone on endosteal surfaces, which serves as a calcium reservoir for egg-laying females and experiences varying rates of osteoclastic and osteoblastic activities [96, 97]. The formation of medullary bone can be induced in male birds as well through the administration of estrogen [98]. Although one of the early animal models employed to study skeletal adaptation was the surgically isolated turkey ulna [24, 47, 50], it was limited by the invasiveness and highly non-physiologic strain profile induced [24, 141]. Given the available non-invasive skeletal loading models, it is currently impossible to make direct assessments of the sensitivity of various vertebrate skeletons.

Although the rodent models have generally shown increases in bone mass and moments of inertia relative to the load stimulus above a certain MES [34, 51, 165], it seems possible that different vertebrates may regulate bone strength or stiffness variably based on species-specific factors. Development of a novel avian model to study bone adaptation could be used to provide initial insights into skeletal sensitivity across vertebrates, and would also offer a novel bipedal model that, unlike the small rodent models, is known to exhibit haversian remodeling [24]. In this chapter, we sought to evaluate skeletal sensitivity and adaptive response of the mouse tibia and a novel avian model, the chukar partridge tibiotarsus, to relatively similar increases in bone strains. Previous comprehensive strain characterizations (Chapter 2) were used to determine the necessary experimental loads that induced similar increases in strain relative to peak strains measured during treadmill running for each species. Non-invasive, axially compressive experimentally applied loading studies were conducted for both species and the resulting tissue level responses were measured by microCT and histomorphometry. Additionally, colony forming unit-osteoblast assays were performed for each species to compare the osteogenic potential of bone marrow-derived mesenchymal stem cells from similar quantities of total marrow cells.

4.2 Methods

4.2.1 Animals

C57Bl/6 male mice (Jackson Laboratory, Bar Harbor, ME, USA) were obtained at 15 weeks of age and housed individually with free access to water and a maintenance diet in a 12-

hour light/dark cycle. The chukar partridge was chosen as the avian model because it is a flightless avian species that is commercially available, and its tibiotarsi are large enough to instrument with three strain gauges yet small enough that loads above -200N would not be necessary. Chukar partridge were obtained at 10±2 weeks of age (CM Game birds, Calais, ME, USA) and group-housed in indoor enclosures with free access to water and a maintenance game bird diet in a 12-hour light/dark cycle. All procedures were approved by the Purdue University IACUC (Protocol # 1310000977).

4.2.2 Experimentally Applied Loading: Mice

The left tibia of each mouse was loaded while the right tibia served as a paired, non-loaded contralateral control. Mice underwent either two weeks (n=5, Mass: 27.47 ± 1.35 g) or four weeks (n=10, Mass: 27.90 ± 1.32 g) of non-invasive externally applied axial compressive loading five days per week, with load bouts occurring approximately 24 hours apart. Mice were anesthetized (2% isoflurane, 2 L/min), and the left limb was secured between custom cups that fitted the knee and ankle (**Figure 4.1**). The load protocol consisted of 216 cycles applied cyclically at 4 Hz. The target load level was chosen such that the strains induced at the medial midshaft were 2.5x the peak strains measured during high speed locomotion. Based on the experimentally applied load and bone strain relationship determined in Chapter 2, a load of -6.5N was used. In order to assess the time course of osteoid mineralization throughout the duration of the study, the bone fluorochromes calcein (50 mgs/kg) and alizarin red (50 mgs/kg) were administered via intraperitoneal injections at specific time points (**Figure 4.2**).

Three days following the final episode of loading, the animals were euthanized by cervical dislocation. Both left and right tibiae were dissected, cleaned of soft tissue, fixed for 24 hours in 10% neutral buffered formalin, and then stored in 70% ethanol. Whole bones were scanned by high resolution microCT with an isotropic voxel size of 10 µm and integration time of 300 ms (µCT40, Scanco Medical, Basserdorf, Switzerland). Volumes representing 2.5% of bone length at the midshaft, and 2.5% of bone length at 37% and 90% of bone length relative to the proximal end of the bone were selected for bone morphometry analyses. Cortical bone tissue was segmented from non-bone tissue using a Gaussian filter with a fixed threshold. The threshold value was determined by identifying the voxel grayscale value at the average value representing 1/3 of the bone peak from histograms of the midshaft volume of the right non-loaded control limbs (mouse: 2530 mg HA/ccm; chukar: 2605 mg HA/ccm). Maximum (Imax) and minimum (Imin) moments of inertia, bone volume, bone area, and bone mineral density were evaluated. Student's paired, one-way t-tests were performed to test for differences between the loaded and control limbs for each parameter, with $p<0.05$ indicating significance.

4.2.3 Experimentally Applied Loading: Chukar Partridge

The left TBT of each bird was loaded while the right TBT served as a paired, non-loaded contralateral control. Birds were to undergo four weeks (n=4, Mass: 0.44± 0.05 kg) of non-invasive, externally applied axial compressive loading five days per week, with load bouts occurring approximately 24 hours apart. Three out of four birds developed significant soft tissue damage at the knee and ankle of the loaded limb prior to completion of the study, so all four birds were euthanized seven days early, making the actual study duration three weeks. Each day, birds were anesthetized (4% isoflurane, 4 L/min) and the left limb was secured between custom cups that fitted the knee and ankle (**Figure 4.1**). The load protocol was applied five days per week and consisted of 216 cycles applied cyclically at 4 Hz. The original target load level was chosen such that the strains induced were 2.5x the peak strains measured on the medial midshaft surface during high speed locomotion, however due to several fracture failures that occurred during preliminary tests, a load of -130N was ultimately used. Based on the experimentally applied load and bone strain relationship determined in Chapter One, a load of -130N would induce strains approximately 1.5x and 2.5x higher strains on the posterior and medial midshaft surfaces, respectively. In order to assess the time course of osteoid mineralization throughout the duration of the study, the bone fluorochromes calcein (30 mgs/kg) and alizarin red (80 mgs/kg) were administered via intraperitoneal injections at specific time points (**Figure 4.2**).

Three days following the final episode of loading, the animals were euthanized via intravenous injection of sodium pentobarbital in the brachial vein (320 mg/kg Beuthanasia-D, Schering-Plough Animal Health, Union, NJ, USA). Both left and right tibiae were dissected, cleaned of soft tissue, cut into three equal segments, fixed for 24 hours in 10% neutral buffered formalin, and then stored in 70% ethanol. Bone segments were scanned by high resolution microCT with an isotropic voxel size of 15 µm and an integration time of 300 ms (µCT40, Scanco Medical, Basserdorf, Switzerland). Volumes representing 2.5% of bone length at the midshaft, 37%, and 90% of bone length relative to the proximal end of the bone were selected for bone morphometry analyses. Cortical bone tissue was segmented from non-bone tissue using a Gaussian filter with a fixed threshold. The threshold was determined by identifying the voxel grayscale value at the average value representing 1/3 of the bone peak from histograms of the midshaft volume from the right non-loaded control limbs. Maximum (Imax) and minimum (Imin) moments of inertia, bone volume, bone area, and bone mineral density (BMD) were evaluated. Marrow area was additionally evaluated post hoc for the chukar only based on histomorphometry results. Student's paired, two-way t-tests were performed to test for differences between the loaded and control limbs for each parameter, with $p<0.05$ indicating significance.

4.2.4 Mineralized Tissue Histology

Following microCT scanning, mouse and chukar bones were processed for mineralized tissue histology in order to assess time-sensitive parameters of osteoid mineralization at the midshaft via fluorochrome incorporation during the loading studies. Midshaft bone segments were dehydrated and infiltrated under a vacuum (17 Hg) over several days at incrementally increasing concentrations of ethanol and methyl methacrylate (MMA) before being embedded (96% MMA + 4% dibutyl phthalate + 0.8% perkadox). Once polymerization was complete, sections were cut, ground (mouse: 50±5 μm, chukar: 90±5 μm), polished, and cover-slipped. Green and red fluorochrome labels were visualized independently using a microscope with fluorescence (Mouse: BX53, Olympus Life Science Solutions, Center Valley, PA, USE; Chukar: AF6000, Leica Microsystems, Wetzlar, Germany) then merged (ImageJ), and histomorphometry measurements were made using the OsteoMeasure software (OsteoMetrics Inc., Decatur, GA, USA).

Although all normal cortical bone parameters were assessed, only specific basic parameters and measures with significant differences were reported. For the mice that received two weeks of loading, reported values include cortical profile perimeter (Ct.Pf.Pm, mm), marrow profile perimeter (Ma.Pf.Pm, mm), cortical bone area (Ct. B. Ar., mm^2), endocortical and periosteal single label perimeters (Ec.Sl.Pm, Ps.sL.Pm, mm), endocortical and periosteal mineralizing perimeters (Ec.M.Pm, Ps.M.Pm, mm), and endocortical and periosteal mineralizing surfaces normalized to bone surface (Ec.MS/BS, Ps.MS/BS, %) (Table x). Double label-related parameters for both the periosteal and endocortical surfaces were not reported because less than half of the sample did not have measurable double labels on either surface. For the mice who received four weeks of loading and the birds, reported values include periosteal perimeter (mm), endocortical perimeter (mm), cortical bone area (mm^2), marrow area (mm^2), total endocortical mineralizing perimeter (T.Ec.M.Pm, mm), total endocortical inter-label thickness (T.Ec.Ir.L.Th), and total endocortical mineral apposition rate (T.MAR) (table x). The total values were determined for each limb in order to assess combined double label data in addition to the single labels. Assessing totals between successive first (calcein) label and third (calcein) labels would not have fully captured the total study duration since first and second sets of double labels did not necessarily occur at the same locations. The values were then calculated as follows:

$$\text{T.Ec.M.Pm} = \text{Ec.dL.Pm (first label set)} + \text{Ec.dL.Pm (second label set)} + \text{Ec.sL.Pm}/2$$

$$\text{T.Ec.Ir.L.Th} = \text{Ec.Ir.L.Th (first label set)} + \text{Ec.Ir.L.Th (second label set)}$$

$$\text{T.MAR} = \text{T.Ec.Ir.L.Th}/14$$

When calculating mineral apposition rates (MAR), in cases where values were zero, a nominal value of 0.1 µm/day was used [166]. Standard values for Ec.MAR, Ec.dL.Pm, and Ec.Ir.L.Th were also reported for the individual label sets in order to assess differences between each measure during different weeks of loading (**Table 4.3**). T.MAR was divided by 14 because that was the number of days between successive calcein labels for both species. A mixed model repeated measures ANOVA was performed on chukar and mouse Ec. MAR, Ec.dL.Pm, and Ec.Ir.L.Th parameters between each label set to determine if mineral apposition rates within a limb changed depending on the week of loading.

4.2.5 Colony Forming Units-Osteoblast Assays

Non-loaded tibiae/TBTs from new animals for both species were dissected immediately after each animal was euthanized by approved Purdue IACUC methods. Bones were stored in sterile DPBS and transferred to a sterile, negative flow hood. Bones were rinsed in four serial washes of a solution containing 10 ml DPBS, 2ml fungizone, and 2 ml pen/strep to reduce the risk of contamination. For the chukar TBTs, a small hole was drilled in the distal epiphysis, and for the mouse tibiae, proximal and distal ends of the bones were removed using scissors. Marrow was isolated through centrifugation (8000G, 1 minute), re-suspended in primary culture media (alpha-MEM, 10% FBS, 1% pen/strep), and the cell suspension density determined using normal hemocytometer methods. Cells were plated in 6-well uncoated plastic dishes at densities of either

1 or 2 million cells per well (n=6 wells/density/animal for n=3 animals of each species). Cells were maintained in 3 ml of primary culture (10% FBS, 1% Penicillin/Streptomycin, 89% αMEM) media for the first seven days, then cultured in osteogenic media for the next 14 days (primary culture media + 0.05% ascorbic acid, 0.00392% 1 x 10^{-8} M dexamethasone, 0.3% 3mM β-glycerophosphate), with media changed every 2-3 days throughout.

Staining and absorbance analyses procedures followed previously reported methods exactly [167]. Briefly, on day 21, wells were rinsed with sterile dPBS, and then fixed for 15 minutes with 10% neutral buffered formalin. The wells were then washed with dH_20 prior to the addition of 1mL 40 mM alizarin red stain (pH 4.1-4.3), and incubated at room temperature for 20 minutes with gentle shaking on a rocker. Wells were washed with dH_20 to remove excess stain, and then imaged using an inverted camera (Nikon). In order to quantitatively assess mineralization, wells were rocked gently at room temperature for 30 minutes with 800 µL acetic acid to lift the cell layer. The slurry was then vortexed, heated to 80°C via a water bath, cooled in ice, and the supernatant removed. Supernatant samples were neutralized to a pH between 4.1-4.5 with 200µL of 10% ammonium hydroxide, then aliquoted (150 µL) and read in triplicate at 405 nm in 96-well format using black-walled, transparent-bottomed plates using a plate reader (Glomax Discover System, Promega, Madison, WI, USA).

4.3 Results

4.3.1 Bone geometry, volume, and mineral density in response to mechanical load

For the mouse in the cortical VOI at 50% of the tibia's length from its proximal end, daily applied dynamic loading increased maximum and minimum moments of inertia, bone volume, and bone area in the left loaded compared to the right contralateral control limb after two weeks of loading, but these differences were not apparent in loaded versus contralateral control limbs for mice who received four weeks of loading (**Figure 4.3**). Alternatively, bone mineral density increased after four weeks of load, but not after two weeks. There was no statistical difference between the right control limbs for any of the measures between the two week and four week load groups.

In the cortical VOI at 37% of the tibia's length from its proximal end, daily applied dynamic loading increased the maximum moment of inertia in the left loaded limb compared to the right contralateral control limb after two weeks of loading, but there was not a difference between limbs for mice who received four weeks of loading (**Figure 4.4**). No other parameters were significantly affected by load for both the two week and four week load groups. There were no statistical differences between the right control limbs for any of the measures between the two week and four week load groups.

For the chukar, in the cortical VOI at 50% of the tibia's length from its proximal end, daily applied dynamic loading increased the maximum moment of inertia and decreased bone area in the left loaded limb compared to the right contralateral control limb after three weeks of loading (**Figure 4.5**). There were also trends that marrow area was larger and cortical bone volume was lower in the loaded limbed compared to the control limb. In the cortical VOIs at 37% and 90% of the tibia's length from its proximal end, no significant effect of load was measured by microCT (**Figure 4.6**, **Figure 4.7**).

4.3.2 Histomorphometry

For the mouse, no significant differences were found for the left-loaded limb compared to the right-control limb after both two weeks and four weeks of loading for bone geometry parameters as well as label-related parameters such as mineralizing surfaces and mineral apposition rates (**Table 4.1**). For the four week group, less than half of the sample size had visible periosteal single or double labels, so sample means for periosteal surface labeling-related parameters were not calculated. For the four week study duration group, triple labeling allowed investigation into differences between mineral apposition rates, labeled surfaces, and inter-label thicknesses for weeks 2-3 and weeks 3-4, separately. Although within each week the left and right limbs did not have different Ec.MAR, Ec.dL.P, or Ec.In.L.Th., these parameters increased similarly from weeks 2-3 to weeks 3-4 for both the left and right limbs (**Table 4.3**).

For the chukar, no significant differences were found for the left-loaded limb compared to the right-control limb for bone geometry parameters as well as for the majority of labeling-related parameters (**Table 4.2**). The exceptions were Ec.MAR, T.Ec.M.Pm, and T.Ec.MAR, which were all greater in the right-control limb compared to the left-loaded limb. Again, the series of three labels allowed investigation into differences between endocortical mineral apposition rates, labeled surface perimeters, and inter-label thicknesses between weeks 1-2 and 2-3 (**Figure 4.8**). Although all left to right limb comparisons were non-significant each week, there were trends seen that Ec.MAR and Ec.dL.P were lower for the left limb compared to the right. Additionally, from weeks 1-2 to 2-3, all three parameters decreased significantly in both loaded and control TBTs with time (**Table 4.3**).

4.3.3 CFU-OB Assay

For both species, bone marrow cultures were successfully completed for n=3 animals, with 6 wells per animal at densities of 1 and 2 million cells each for a total of n=18 wells per cell density. Absorbance, which increases relative to the amount of mineral present in each culture, was measured at 0.162 ± 0.028 and 0.193 ± 0.017 for wells with a cell density of 1 million, and 0.304 ± 0.067 and 0.220 ± 0.046 for wells with a cell density of 2 million, for the mice and chukar, respectively (**Figure 4.10**). Absorbance significantly increased with cell density for the mouse ($p<0.001$), but not for the chukar. Comparatively, absorbance was greater in the mouse for 2 million cells/well ($p=0.003$), but was similar between the species for the 1 million cells/well cultures. Images of the wells prior to stain extraction were qualitatively assessed for any gross differences between mouse and chukar colonies (**Figure 4.9**). Qualitatively, mouse colonies were more numerous but smaller relative to the colonies formed by chukar MSCs.

4.4 Discussion

Although rodent models have provided extensive insight into skeletal sensitivity and the adaptive response to mechanical load, no studies to our knowledge have previously attempted to determine if sensitivity is consistent across vertebrate species. The skeleton is very diverse in its morphology, geometry, and mechanical properties across vertebrate species, so it seems possible that adaptation may vary by rate and bone quality feature (i.e. independent changes in BMD, bone volume, or cross-sectional geometry) based on the needs of each species. Here we've attempted to make initial assessments of skeletal sensitivity in a novel non-invasive avian model, the chukar partridge TBT, relative to the mouse tibial loading model. In order to compare sensitivities and adaptive responses, experimental load magnitudes were applied such that they would induce similar relative increases in peak bone strains measured during treadmill running at the medial midshaft surface. The new loading model encountered several issues including fracture failure, which limited our load magnitude, as well as serious soft tissue damage due to daily load application, which ultimately limited our study duration. Despite these issues, we were able to measure a load-related geometry response for the chukar TBT. Although we had to limit our load level for the mouse tibia in order to maintain similar relative increases in load to the chukar, we were also able to measure a geometry and bone mass response to load after two weeks, although not after four weeks. CFU-OB assays also demonstrated that despite similar amounts of mineral generated, the colonies were qualitatively quite different. Overall, the results suggest that while the mouse skeleton adapted to our load initially through increases in bone mass and geometry, the chukar skeleton attempted to adjust only geometry to better resist our induced bending without complementary increases in bone mass.

4.4.1 The Mouse Tibia showed a geometry and bone volume response after 2 weeks but not after 4 weeks

Although we measured a geometric and volumetric response to load in the mouse after two weeks, it seems that our stimulus was no longer anabolic by weeks 3-4, possibly due to natural bone growth over the course of the study. Increasing endocortical fluorochrome labeling from weeks 2-3 to weeks 3-4 further implies that the rate of natural growth may have increased towards the latter half of the four week study when the mice were 18-19 weeks old, whereas the two week study would have ended at the end of their 17th week prior to the growth increase. It seems possible that while our load may have induced strains just above the MES in order to invoke an early adaptive response, the response saturated after a few weeks and natural growth ultimately muted any load-related response by the end of four weeks. Increases in maximum and minimum moments of inertia, bone volume, and bone area measured at the midshaft after two weeks of loading are all adaptations that would make the bone more resistant to bending and likely decrease the strain induced by our applied load [168-170], and represents a similar type of response to what has been reported in other studies employing the mouse tibial loading model [34, 51, 119, 165]. After four weeks of our loading protocol, the only significant difference was a higher bone mineral density in the loaded limb. The four week group did show increased BMD relative to the control limb, which is a response similar to what has been seen during exercise studies [17-19]. The strains induced in the bone during exercise would represent a small relative increase in loading to the skeleton compared to the strains that can be induced during experimental loading. It seems possible that natural growth over time altered the necessary adaptation to our chosen load magnitude from a bone volume and geometry response to an increase in BMD based on the bone’s natural threshold for adaptation.

Despite higher peak strains predicted in the mouse tibia at 37% of bone length relative to the proximal end of the tibia compared to the midshaft (Chapter 2), maximum moment of inertia was the only parameter that increased in the loaded limb relative to the control, and only after two weeks. The 37% volume was originally selected due to the higher peak strains predicted by our finite element models. If peak strain magnitude is the most important stimuli to the bone, we should have measured a significant bone volume response at 37% compared to at the midshaft. Although previous mouse tibial adaptation studies have shown a stronger response at this location relative to the midshaft [51, 119, 165], that is not what we have observed at a -6.5N load magnitude.

Although we were able to measure load-related differences by microCT, histomorphometry measurements were not able to discern geometric differences between the loaded and control limbs for either study duration, and any fluorochrome labeling present in the loaded limb was not significantly different from the control limb. One of the significant limitations of the histological approach to assessing bone deposition is that measurements are limited to a single section of bone, rather than a volume that can be accurately selected during microCT analyses, so it is possible that we missed areas of load-related labeling. The presence of labeling in the right-control limb, though, suggests that some natural bone growth was occurring throughout the duration of our studies.

4.4.2 The Chukar Partridge TBT showed a geometric cortical bone response after 3 weeks of loading

Increased maximum moment of inertia and decreased bone area along with suppressed endocortical bone deposition at the midshaft VOI could indicate that the avian TBT attempted to adapt its cross-sectional geometry to increase resistance to the bending our axial compressive loads without increasing bone mass. The average maximum radius of the midshaft cross-section VOI would have had to increase enough through modeling and remodeling to overcome a lower mass in the loaded limb compared to the control in order for the loaded limb to achieve a higher maximum moment of inertia. Since the avian skeleton prioritizes a ‘light’ skeleton, this seems like a reasonable strategy for adapting to relatively small increases in bone strains without metabolically costly increases in bone mass. Histomorphometry results indicated that while some bone deposition did occur at the midshaft throughout the study in both limbs, mineral apposition was suppressed in the loaded limb compared to the control limb.

Despite the decreased endocortical mineral apposition rates, mineralizing surfaces, and label thicknesses, there wasn't a significant difference in cortical thickness or bone area by histology, or bone volume by microCT between left and right bones, although the trends seen by microCT do support the histomorphometry results. It is possible that the small differences between left and right TBT's were not well represented by the single cross-section used for histomorphometry analysis. Especially for the chukar relative to the mouse, a 90µm thick section represents a very small portion of total bone length. While there were trends that cortical bone area was lower and marrow area was higher in the loaded limbs relative to the control limbs, the individual differences for each animal were less than 0.15mm^2 and 0.3mm^3, respectively. Regardless, it seems that such small differences in bone volume and area would have a fairly small impact on bone stiffness or strength, although for a load inducing strains equal to or less than 2.5x peak strains measured during fast running, a more significant response may not have been necessary.

Although statistical analyses did not show differences in bone area and volume at the 90% VOI for the complete sample, woven bone was identified by qualitative observations of the microCT scans for one of the loaded TBTs (**Figure 4.11**). This was the smallest bird by individual mass, so it's possible that its bones were smaller and the resulting peak strains from a -130N load were higher relative to the other three chukar. While we estimated the peak strains that occur in TBT of a male chukar at approximately 16 weeks of age using finite element models (Chapter 3), a range of responses from no response to a woven bone response suggests a potentially large discrepancy in strains in the 90% VOI. An alternative explanation could be that the strain window for a lamellar bone response is comparatively small and that the threshold for a woven bone response is lower in the avian skeleton compared to the murine skeleton. Based on results from Chapter 3 of this thesis, peak compressive strains in that volume were approximately -3000με. In the turkey ulnar loading model, the only other avian species in which bone adaptation has been studied to our knowledge, bending loads inducing peak strains around -1000με resulted in insignificant amounts of periosteal bone deposition [140], but peak strains of approximately -1700με induced a significant woven bone response [42]. It is unclear if that woven bone response was a result of the peak strain magnitudes or the abnormal strain profile and disuse osteopenia induced by that loading model, but taken together with our results could suggest that the strain window for generating no response to a woven bone response is a small strain range for the avian skeleton.

Initially, two and four week studies with a load magnitude of -200N were planned for the birds. Unfortunately, within the first three days of those studies, which were happening simultaneously, six of the birds experienced TBT fractures distally during applied loading. As a result, we ended the studies immediately due to concern for the birds. We attempted to restart the studies with just two birds at a load of -160N, but one of those birds experienced fracture after two weeks of loading, so we did not feel comfortable committing a larger sample size to a study at that load magnitude. At that point, we had four remaining birds who had no applied loading history. We chose to run a four week loading study with a load magnitude of -130N. Unfortunately that study also had to be cut short by a week due to significant soft tissue damage at the knee and ankle, an effect from loading this author had never seen during several other preliminary loading experiments in both chukar and guinea fowl. One of the consistent difficulties with the bird model has been the availability of animals; juvenile adult chukar are only available between September and November. While additional loading studies to increase our sample size and complete the two week study duration are planned, they could not be fully completed prior to the writing of this thesis.

4.4.3 Colony Forming Unit – Osteoblast assays revealed qualitative differences in the colonies between the species

Despite the results showing that initial marrow cell density had a significant effect on mineral deposition in 2D cultures for the mouse but not the chukar, the arguably more interesting assessment may come from the qualitative difference between the colonies formed by each species. Counting colonies is the most common analysis technique for the CFU-OB assay because a single osteoblast progenitor is responsible for each colony, so this analysis method reflects the original percentage of mesenchymal stem cells present in the marrow [171, 172]. We chose to quantitatively assess mineralization via absorbance of alizarin red stain instead of colony numbers because the colonies formed, especially for the mouse, were not always distinct, which would make colony counting very subjective. However, the obvious discrepancy between the number of colonies and the mineral produced by each raises questions regarding marrow cell population and marrow-derived osteoblast progenitors across the two species. Previous studies have demonstrated correlations between treatment-related (i.e. bisphosphonate/ glucocorticoid stimulation,) *in vivo* increases or decreases in bone mass with similar changes in osteoblastogenesis and mineral deposition via the CFU-OB assay [85, 173]. For those studies, species and culture duration were the same, so the resulting number of colonies was related to the treatment. Additionally, differences in proliferation rate and differentiation potential have been shown to vary even within different strains in inbred mice [174]. These previous results suggest that systemic factors have an impact on marrow cell population or osteoblast progenitors. For our studies, culture duration and conditions were the same, so any differences between the colonies and the amounts of mineral produced by the completion of the study are inherent to the species. Based on our results, it seems that osteoblast progenitor cells are more prevalent in the marrow of mice, but a single progenitor can generate more mineral over the same period of time for the chukar relative to the mouse. Unfortunately, we do not know what systemic factor differences occur between these two species or what led to the results we found through the CFU-OB assay, but it seems reasonable to expect that whatever these differences are could also more generally affect skeletal adaptation.

Despite the differences in study durations and the varied peak strain magnitudes at relatively similar volumes along the diaphysis (Chapter 3), the results generally suggest that the birds adapted to increase their bone strength through changes in geometry without increasing bone mass, whereas the mouse adapted via changes in geometry in addition to increased bone mass. CFU-OB results further suggested that there are inherent differences between marrow cell populations or marrow-derived osteoblast progenitors, possibly due to differences in systemic factors, between the two species, which could impact skeletal adaptation. While this work will benefit from larger sample sizes and more study durations, these findings provide early evidence that skeletal adaptation across vertebrates is variable and that probing the mechanobiology responsible for these differences could generate novel insight into skeletal regulation.

Table 4.1 Select histomorphometry results for the two week mouse loading group (n=5).Values represent the mean ± standard deviation for each measure for the left (L) loaded limbs and the right (R) control limbs. Paired, two-tailed students T-test were used to evaluate statistical differences between loaded and control limbs for each measure.

	Ct.Pf.Pm (mm)	**Ma.Pf.Pm (mm)**	**Ct. B. Ar. (mm^2)**	**Ct. Ma. Ar (mm^2)**	**Ec.sL.Pm (mm)**
L	4.37 ± 0.37	2.74 ± 0.33	1.13 ± 0.11	0.44 ± 0.08	1.36 ± 0.40
R	4.31 ± 0.44	2.78 ± 0.36	1.11 ± 0.10	0.45 ± 0.06	1.16 ± 0.63
P-Value	0.48	0.71	0.23	0.45	0.15
	Ps.sL.Pm (mm)	**Ps.M.Pm (mm)**	**Ps.MS/BS (%)**	**Ec.M.Pm (mm)**	**Ec.MS/BS (%)**
L	2.50 ± 1.19	1.26 ± 0.61	76.88 ± 34.66	0.80 ± 0.37	29.33 ± 14.08
R	1.93 ± 1.11	0.96 ± 0.56	64.22 ± 38.12	0.61 ± 0.36	22.67 ± 14.18
P-Value	0.47	0.46	0.63	0.19	0.21

Table 4.2 Select histomorphometry results for left (loaded) versus right (control) limbs for the mice (n=10) after four weeks of loading and chukar (n=4) after three weeks of loading. Values represent mean ± standard deviation. Student's paired two-way t-tests were used to assess statistical differences between the left and right limbs for both species.

	Limb	**Mouse**	**P-value**	**Chukar**	**P-value**
Periosteal Perimeter (mm)	Left	4.25 ± 0.34	0.66	12.88 ± 1.44	0.53
	Right	4.30 ± 0.28		13.48 ± 0.69	
Endocortical Perimeter (mm)	Left	2.80 ± 0.39	0.65	9.68 ± 1.17	0.50
	Right	2.85 ± 0.35		10.37 ± 0.66	
Cortical Bone Area (mm^2)	Left	1.13 ± 0.12	0.60	11.56 ± 1.94	0.25
	Right	1.15 ± 0.12		13.05 ± 0.90	
Marrow Area (mm^2)	Left	0.47 ± 0.08	0.39	6.32 ± 1.26	0.49
	Right	0.50 ± 0.08		6.82 ± 0.33	
Total Endocortical Mineralizing Surface (mm)	Left	0.61 ± 0.30	0.97	5.34 ± 2.64	0.02
	Right	0.61 ± 0.27		7.42 ± 2.65	
Total Endocortical Interlabel Thickness	Left	4.58 ± 3.42	0.55	9.01 ± 1.84	0.046
	Right	5.53 ± 5.10		15.61 ± 3.58	
Total Endocortical Mineral Apposition Rate	Left	0.35 ± 0.24	0.48	0.64 ± 0.13	0.046
	Right	0.42 ± 0.33		1.12 ± 0.26	

Table 4.3 Time point specific histomorphometry results for the mouse (n=10) after four weeks of load and the chukar (n=4) after three weeks of load. Values represent mean ± standard deviation. Paired two-tail students t-tests were used to compare left versus right limbs within each week. A mixed model repeated measures ANOVA was used to assess how values changed from week to week.

		Limb	Mouse	L vs. R comparison P-value	Week to Week Comparison P-Value	Chukar	L vs. R comparison P-value	Week to Week Comparison P-Value
Endocortical Mineral Apposition Rate	Week1-2	Left				1.21 ± 0.26	0.15	0.003
		Right				1.66 ± 0.40		
	Week 2-3	Left	0.15 ± 0.16	0.39	<0.001	0.35 ± 0.29	0.08	
		Right	0.30 ± 0.48			0.97 ± 0.62		
	Week 3-4	Left	0.72± 0.40	0.94				
		Right	0.73 ± 0.47					
Endocortical Double-Label Perimeter	Week1-2	Left				3.25 ± 3.17	0.23	0.01
		Right				3.80 ± 3.53		
	Week 2-3	Left	0.002 ± 0.006	0.25	<0.001	0.33 ± 0.59	0.09	
		Right	0.01 ± 0.03			1.01 ± 1.02		
	Week 3-4	Left	0.21 ± 0.17	0.43				
		Right	0.16 ± 0.16					
Endocortical Interlabel Thickness	Week1-2	Left				7.23 ± 1.55	0.15	0.003
		Right				9.95 ± 2.38		
	Week 2-3	Left	0.36 ± 1.12	0.41	<0.001	1.78 ± 2.07	0.25	
		Right	1.31 ± 3.10			5.66 ± 4.02		
	Week 3-4	Left	4.22 ± 2.64	0.1				
		Right	4.22 ± 3.12					

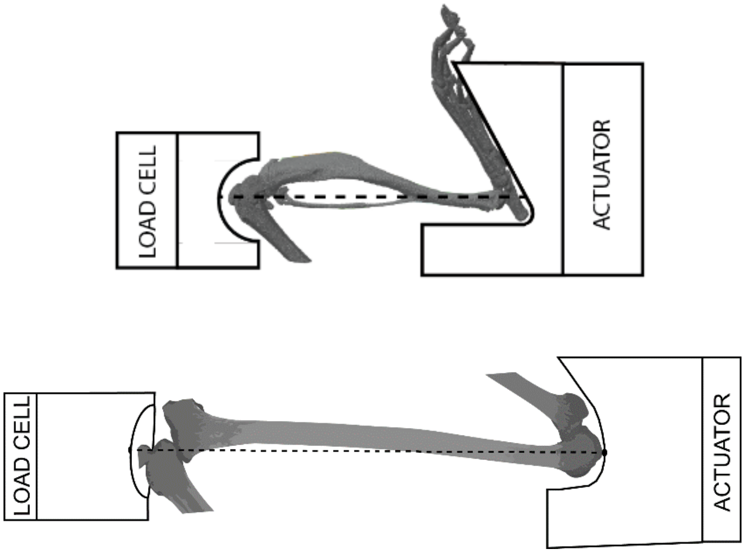

Figure 4.1 Diagrams representing the configuration of a mouse tibia (top) and chukar TBT (bottom) while held in the cups of the loading device. Load is applied through the actuator, which is connected to the ankle cup, and is transmitted through the tibia/TBT and knee, to the load cell. Figures are not to scale.

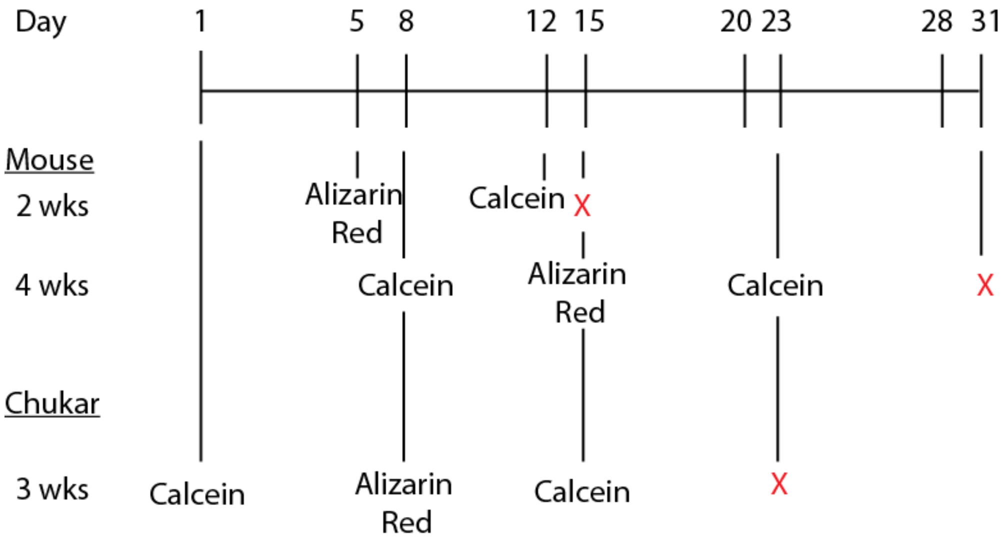

Figure 4.2 Timeline of the loading study for both the mice and chukar. The days on which flourochromes were given for each of the studies is indicated. Red ‘X’ indicates the day on which animals for each study were euthanized.

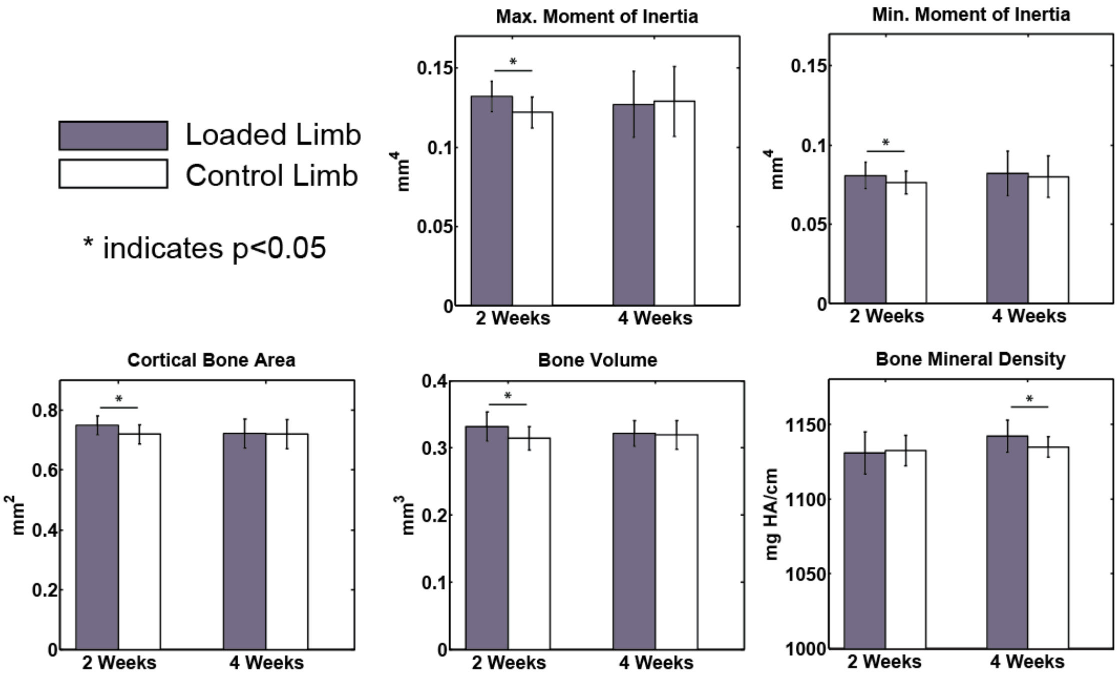

Figure 4.3 Cortical bone morphometry results by microCT for the mouse tibia for 2.5% of bone length, centered at the midshaft for bones loaded either two weeks (n=5) or four weeks (n=10). Parameters include maximum and minimum moments of inertia, cortical bone area, cortical bone volume, and bone mineral density. Units are indicated on the y-axis for each plot. Purple bars represent the loaded, left limb, and white bars represent the right, non-loaded control limb. Asterisks (*) indicate a significant difference between loaded and controls limbs (paired, one-way T-test, $p<0.05$).

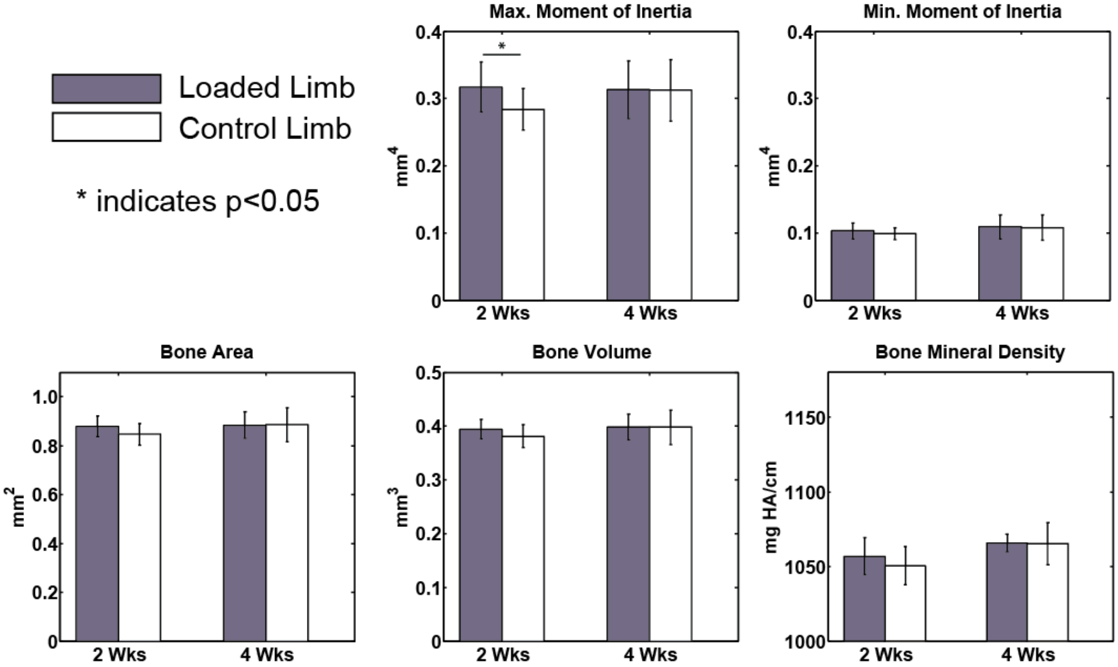

Figure 4.4 Cortical bone morphometry results by microCT for the mouse tibia for 2.5% of bone length, centered at 37% of bone length relative to the proximal end for bones loaded either two weeks (n=5) or four weeks (n=10). Parameters include maximum and minimum moments of inertia, cortical bone area, cortical bone volume, and bone mineral density. Units are indicated on the y-axis for each plot. Purple bars represent the loaded, left limb, and white bars represent the right, non-loaded control limb. Asterisks (*) indicate a significant difference between loaded and controls limbs (paired, one-way T-test, $p<0.05$).

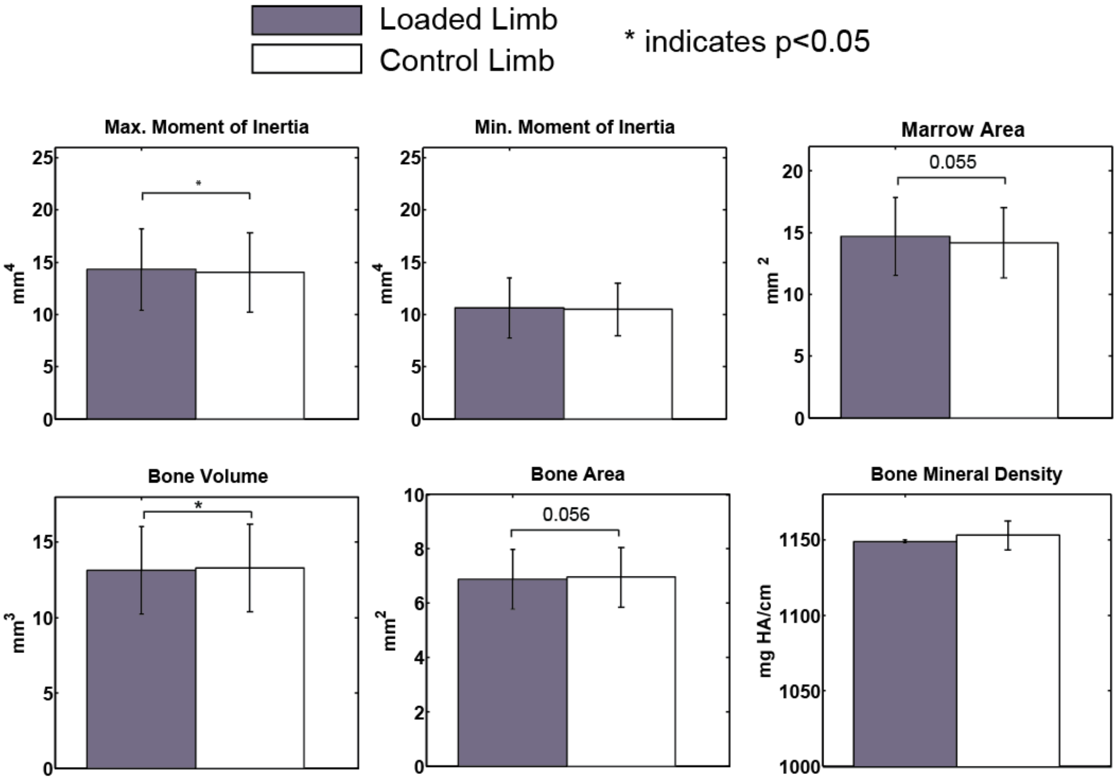

Figure 4.5 Cortical bone morphometry results by microCT for the chukar TBT for 2.5% of bone length, centered at the midshaft for bones loaded for three weeks (n=4). Parameters include maximum and minimum moments of inertia, marrow area, cortical bone area, cortical bone volume, and bone mineral density. Units are indicated on the y-axis for each plot. Purple bars represent the loaded, left limb, and white bars represent the right, non-loaded control limb. Asterisks (*) indicate a significant difference between loaded and controls limbs (paired, one-way T-test, $p<0.05$). Parameters whose p-values were trending towards significance have also been included.

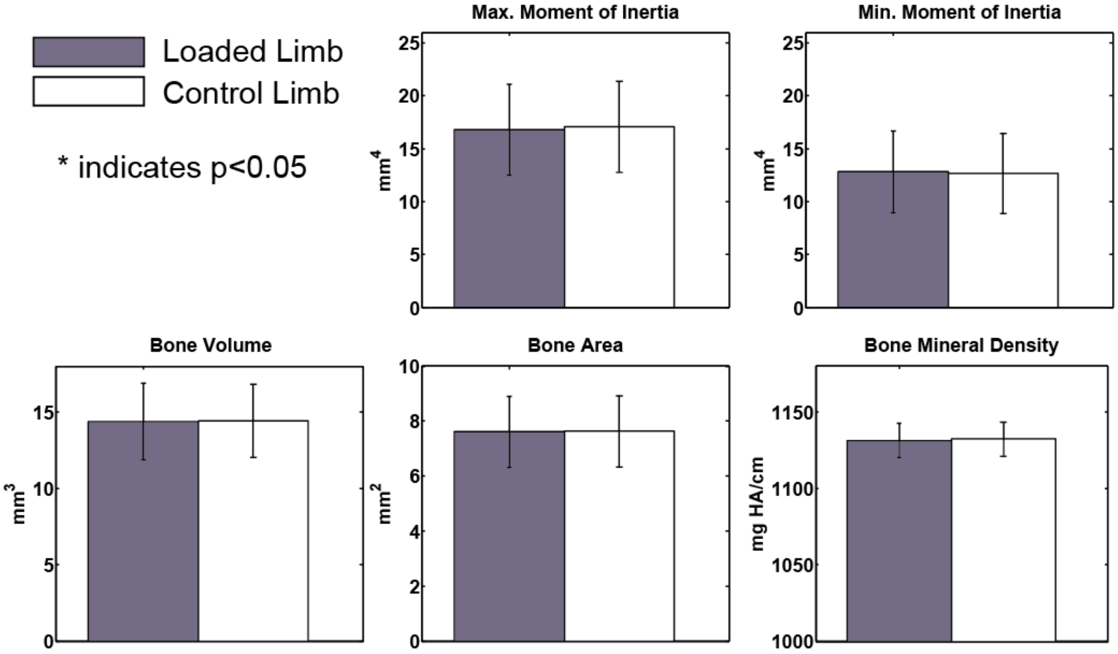

Figure 4.6 Cortical bone morphometry results by microCT for the chukar TBT for 2.5% of bone length, centered at 37% of bone length relative to the proximal end for bones loaded for three weeks (n=4). Parameters include maximum and minimum moments of inertia, cortical bone area, cortical bone volume, and bone mineral density. Units are indicated on the y-axis for each plot. Purple bars represent the loaded, left limb, and white bars represent the right, non-loaded control limb. Asterisks (*) indicate a significant difference between loaded and controls limbs (paired, one-way T-test, $p<0.05$).

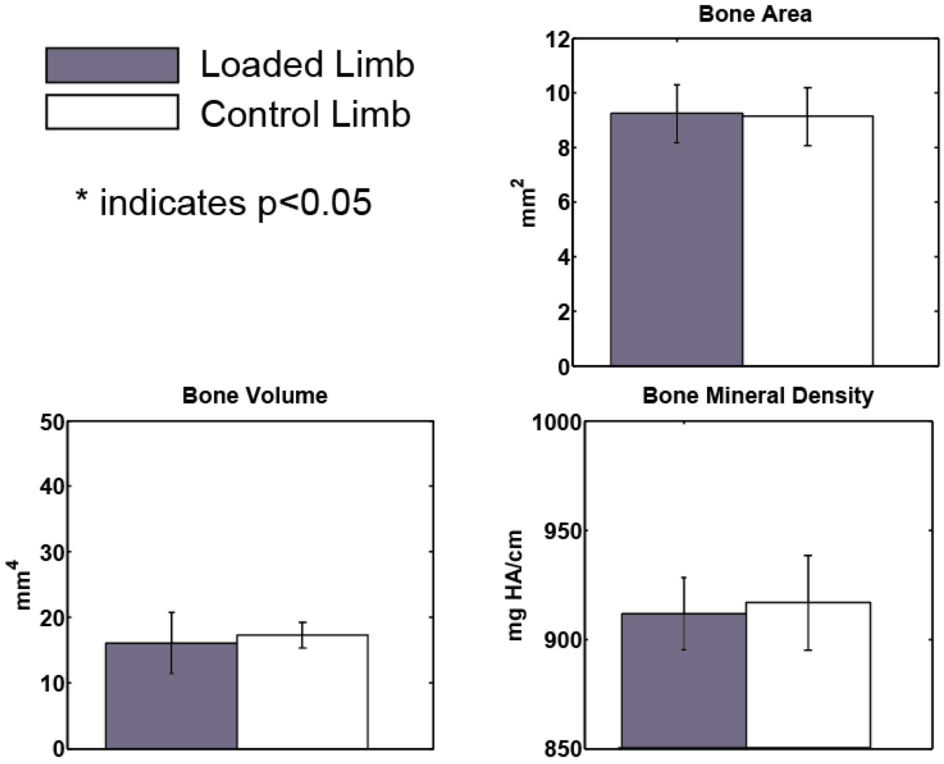

Figure 4.7 Cortical bone morphometry results by microCT for the chukar TBT for 2.5% of bone length, centered at 90% of bone length relative to the proximal end for bones loaded for three weeks (n=4). Parameters include cortical bone area, cortical bone volume, and bone mineral density. Units are indicated on the y-axis for each plot. Purple bars represent the loaded, left limb, and white bars represent the right, non-loaded control limb. Asterisks (*) indicate a significant difference between loaded and controls limbs (paired, one-way T-test, $p<0.05$).

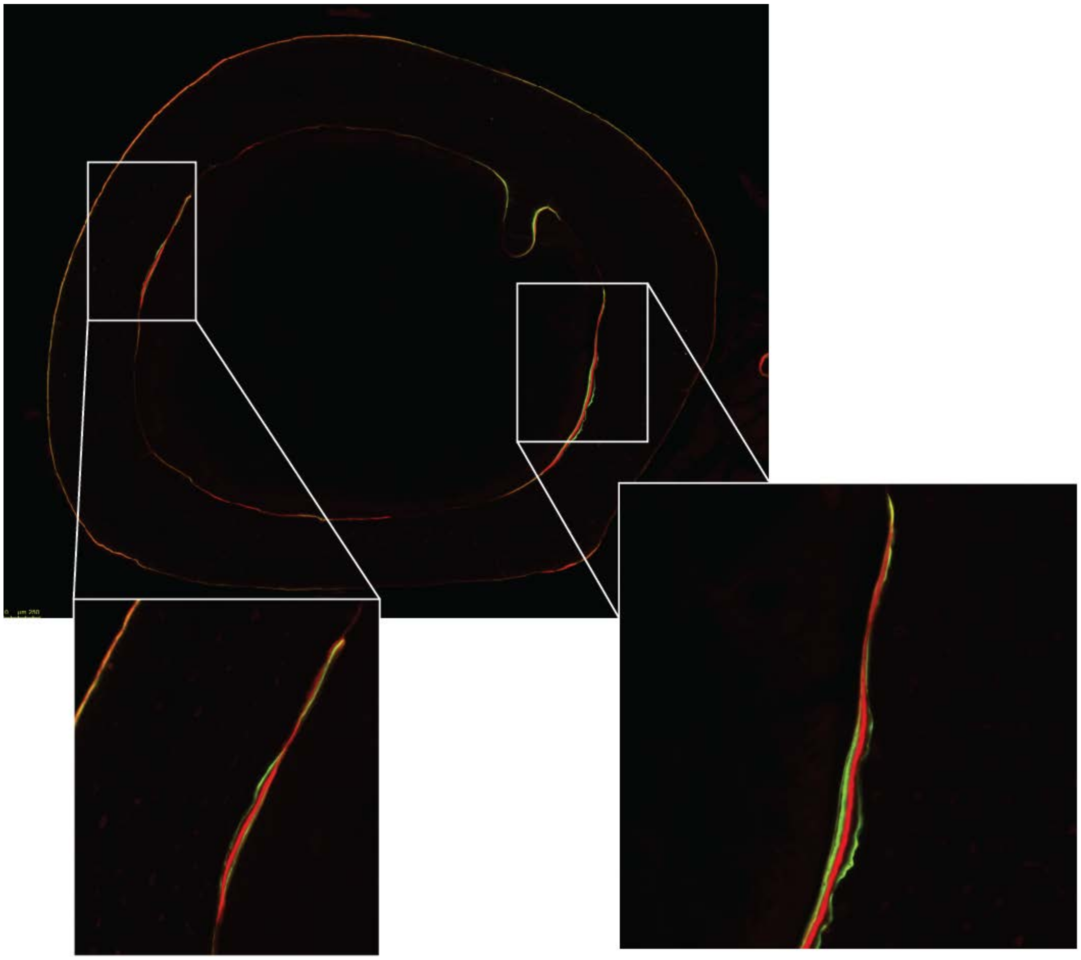

Figure 4.8 Representative fluorescent image of a chukar TBT cortical midshaft cross-section. Green labeling represents calcein stain while the red represents alizarin red stain. Inset images show instances of double labeling on the endocortical surface.

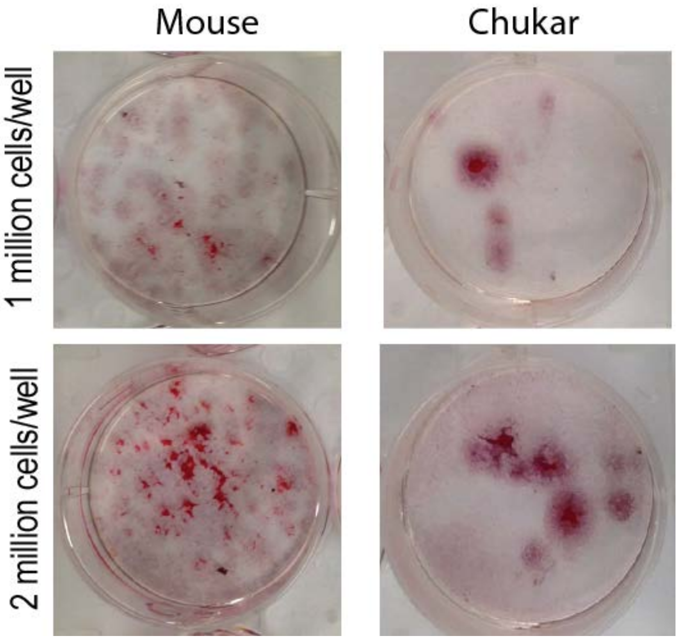

Figure 4.9 Representative images of mouse and chukar CFU-OB wells stained with alizarin red for both marrow cell densities, 1 million and 2 million cells/well.

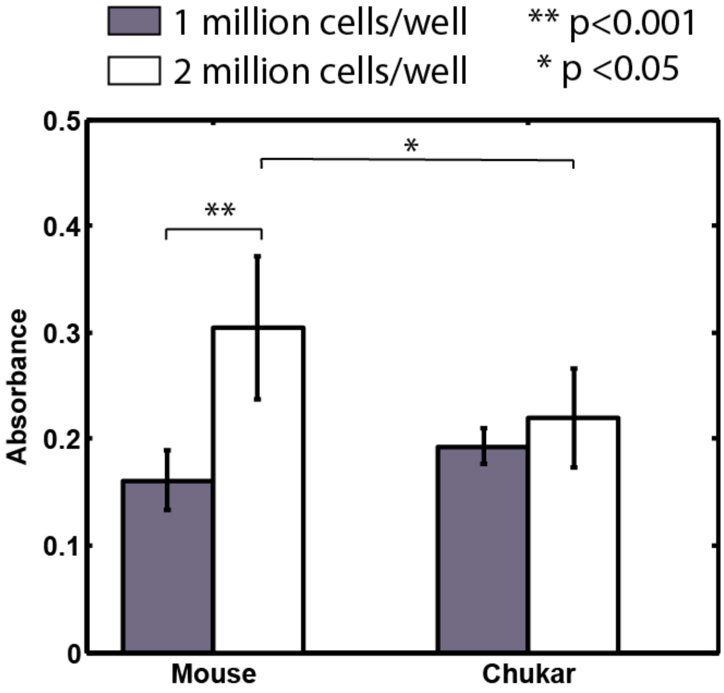

Figure 4.10 Absorbance results at 405 nm for the mouse and chukar CFU-OB assays. For each species, marrow was cultured at two densities (marrow from n=3 animals per species; n=18 wells per density), 1 million cells/well (purple bars) and 2 million cells/well (white bars). Results are plotted as mean ± standard deviation. An increase in absorbance would indicate increased mineral produced by the culture.

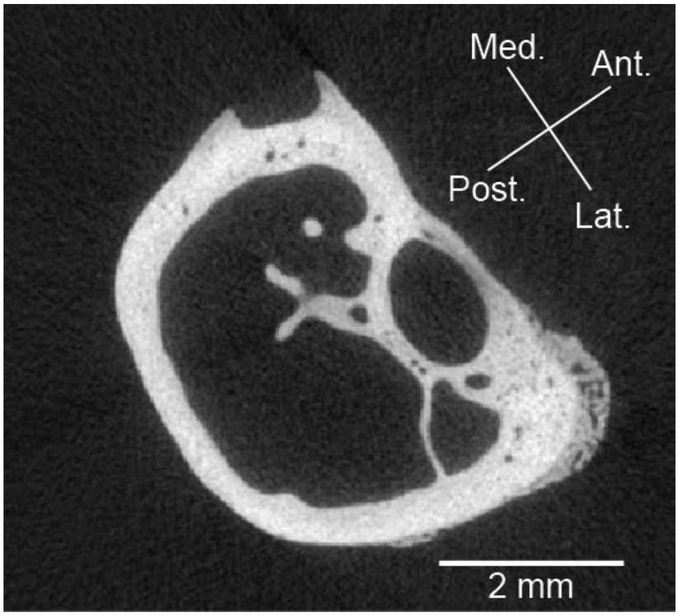

Figure 4.11 MicroCt cross-sectional image of a chukar TBT showing woven bone on the antero-lateral surface near the distal metaphysis.

[For this chapter, I would like to specifically acknowledge the Purdue Bone and Body Composition Core, and the Purdue Histology Research Laboratory for their assistance with microCT scanning and mineralized tissue histology processing, respectively.]

5. DEVELOPMENT OF A NOVEL ISOLATED BONE ORGAN CULTURE SYSTEM

5.1 Introduction

The skeleton is highly integrated with systemic physiology through its vascularity and the lacunar-canalicular network. Systemic factors are involved in regulating osteoblast and osteoclast activity necessary for bone remodeling [4, 175-177]. Systemic regulators of bone metabolism include factors such as basal metabolic rate, parathyroid hormone, and calcitonin, as well as several other hormones, cytokines, and growth factors [77, 178, 179]. Relative differences in these factors across vertebrate species and or as a result of disease states could play a role in differential bone metabolism rates during skeletal adaptation in response to mechanical stimulation, but there is not currently a way to assess bone cell activity and response to mechanical load while cortical bone is isolated from these factors.

In vitro techniques, such as 2D cell cultures or 3D bioreactor systems, are often used to test a variety of factors and conditions on specific cells or tissues in an isolated system [180-182], such as stimulating osteoblast-like cells cultured from trabecular bone explants *in vitro* with human growth factor, but there are some drawbacks to the current models. Some studies have used embryonic bone organ explants to study the effects of various hormones and growth factors, and/or mechanical load on bone [183-188]. Their small size and cartilaginous state likely benefit cell survival. However, embryonic bones do not accurately represent the post-natal or mature skeleton. They are also very fragile and already actively involved in growth and mineralization, which could confound any response to experimentally applied stimuli. Utilizing mature bone segments in culture maintains the native density and network of the bone cells in their complex 3D environment as well as cellular interactions with the native extracellular matrix. Maintaining those features of the native bone is an obvious benefit compared to 2D *in vitro* culture or current 3D hydrogel techniques, while still allowing more control over chemical and mechanical stimuli to the cells relative to *in vivo* studies. So far, *in vitro* mature bone organ cultures have been limited to cancellous bone explants loaded in compression, and good cell viability can be maintained up to four weeks under perfusive media conditions [189-194]. Although the porous nature of cancellous bone provides an innately large surface area to media ratio which likely benefits the model's ability to maintain cell viability, the porosity also makes it difficult to directly measure the strain induced by the compressive loads. It is well established that there is a relationship between strains induced by a mechanical load and the resulting adaptive response, so characterizing the strain stimulus is critical for interpreting the bone's mechanobiologic response. Additionally, *in vivo* loading studies have also shown that cortical and cancellous bone have different responses to mechanical stimuli [195, 196], therefore studying them both under *in vitro* conditions is important. Cortical bone segments could be instrumented with strain gauges *in vitro* similar to how intact tibiae are instrumented *in vivo* in order to experimentally measure the strains induced by a given load. Yet to our knowledge, a mature cortical bone segment has not previously been kept in *in vitro* conditions for more than 24 hours [197].

Development of a model to study cortical bone's innate response to mechanical load while isolated from systemic factors could provide unique insight into the vertebrate skeleton of various species, specifically the mechanobiological regulation of osteocyte's response to load independent from systemic factors. Using a bioreactor with the capabilities to continuously perfuse media through and around the bone, as well as apply mechanical loads should help to maintain cell viability in cortical bone throughout the culture period relative to previous models. The overarching goal of this work is to take initial steps towards developing a bone organ culture model for mechanobiology studies by validating cell viability in cortical bone samples and to determine the potential for applying physiological tissue strains to the bone samples. Specifically, I will (1) validate the viability of bone cells in a segment of a mouse tibial cortical bone cultured in the biodynamic chamber for five days and (2) determine the relationship between experimentally applied axially compressive load magnitudes and the resulting strains induced in the bone segment when loaded in the biodynamic chamber. Successful development of this model will allow *in vitro* investigations into the skeletal response to mechanical load relative to the stimulus across vertebrate species since the induced strain environment can be characterized through a combination of experimental measurements and finite element models. Additionally, this system will provide a new *in vitro* cortical bone model with the potential for an extensive variety of future biomedical and basic science applications beyond the comparative skeletal biology goals of this thesis.

5.2 Methods

5.2.1 Bone Specimens

Tibiae from male, C57Bl/6 mice between the ages of 16-25 weeks were used in all studies (Jackson Labs, Bar Harbor, ME). Each mouse used was euthanized by cervical dislocation and both tibiae were dissected immediately. Euthanasia procedures were approved by Purdue University IACUC (Protocol # 1310000977).

5.2.2 Validation of Osteocyte Viability in Bone Organ Culture

5.2.2.1 Initial Processing of the Tibiae

Immediately after dissection, bones were maintained in sterile Dulbecco's phosphate buffered saline (dPBS) at room temperature until transferred to a sterile hood. Once in a sterile, negative pressure hood, bones were rinsed twice in a combination of 10 ml dPBS, 1.5 ml Penicillin/streptomycin (pen/strep) and 1 ml fungizone. The proximal and distal ends of the bones were then removed with sterilized scissors, and the bones were rinsed once more in dPBS/pen/strep/fungizone solution.

5.2.2.2 Lactate Dehydrogenase Assay for Cell Viability

A lactate dehydrogenase assay (LDH) was used to assess osteocyte cell viability in negative and positive control samples, as well as tibial samples cultured for five days. Lactate dehydrogenase is an enzyme found in almost all living cells, but is released during tissue damage or cell apoptosis, and can therefore be used to assess tissue breakdown or viability [198]. A benefit of the LDH assay is that the LDH enzyme is present for up to 36 hours after cell death [199], meaning the near-term effects of tissue processing following euthanasia would not affect cell viability analyses. Using this method, viable osteocytes and osteoblasts react with the primary stain to form non-reversible tetrazolium-formazan granules. Following the bone processing outlined above, the LDH staining protocol was performed as follows: bones were rinsed in 37°C Hanks buffered saline, incubated with gentle shaking in the LDH stain for four hours (37°C, 5% CO_2), fixed in 4% paraformaldehyde for 24 hours, demineralized in 15% EDTA for four days, then stored at 4°C in a 2.5% sucrose/deionized water solution. Between each successive step after LDH staining, the bones were rinsed in deionized water. Within two weeks, bones were cut in half with a scalpel along the sagittal plane, embedded cut-surface down in OCT and stored at -80°C until sectioning. All sections were cut using a cryostat (7µm, Leica CM1950, Leica Biosystems, Buffalo Grove, IL, USA), and cover-slipped using a mounting medium (Richard-Allen Scientific Cytoseal XYL, Thermo Scientific, VWR Product #8312-4). Sections were imaged for LDH staining using an upright microscope (BX53, Olympus Life Sciences, Tokyo, Japan) at 20x.

5.2.2.3 Positive and Negative Controls

Positive control bones samples to establish maximum osteocyte viability were dissected following mouse euthanasia and immediately subjected to the LDH staining protocol (n=3). Since the LDH enzyme is valid for several hours after cell or tissue death, the immediate processing and staining procedures for the positive control bones provides a baseline for maximum cell viability. Negative control bones were generated by autoclaving the bone samples (121°C, 30 minutes) immediately following euthanasia and dissection (n=3). These bones were then maintained at room temperature for a minimum of 36 hours prior to performing the LDH assay on the bone samples.

5.2.2.4 Bone Organ Culture in the Biodynamic Chamber

Three organ culture trials (n=2 tibiae per trial from n=3 mice) were completed using a biodynamic chamber (BioDynamic 5100, TA Instruments, New Castle, DE, USA). This biodynamic chamber has previously been used to culture and mechanically stimulate bone cell-seeded scaffolds [200-202], but to our knowledge it has not be used on an actual mature bone. It is designed such that a perfusive flow loop exists between a reservoir bottle and the chamber (**Figure 5.1**). Fluid enters the chamber through one piston, and then leaves through the other. The pistons have porous platens that hold the bone in place (**Figure 5.4**). The entire chamber was sterilized as recommended by the manufacturer. The closed chamber and flow loop were set up under sterile conditions and filled with medium (300 mL per culture: 1% pen/strep, 10% FBS, 89% αMEM). Each bone went through initial processing as described above, was secured between the two porous platens, and the chamber sealed. The chamber, reservoir bottle and tubing were then transferred to and maintained in an incubator (37°C, 5% CO_2). A peristaltic pump (Masterflex C/L Dual channel Variable Speed compact pump, Cole-Parmer, Vernon Hills, IL, USA) was used to recirculate media between the reservoir and chamber for the duration of the culture period at a flow rate of 0.3 mL/minute [189]. Bones were maintained in culture for five days, and were processed for osteocyte cell viability using the LDH assay on the sixth day.

5.2.2.5 Quantitative Analysis of Bone Cell Viability

Cell viability was measured in positive controls (n=3) and cultured bones (n=6) by counting the LDH+ cells within selected areas of cortical bone until a minimum of 450 positive cells had been counted per sample. This required analyzing 13±2 sections from each bone, and average areas of 1.001 ± 0.112 mm^2 and 0.736 ± 0.093 mm^2 for cultured and control bones, respectively. Cells were counted from three slides and a minimum of three sections per slide in order to ensure the areas assessed were broadly representative of a larger volume of the tibial diaphysis. Each image was taken within an acceptable range around the midshaft which was above the tibial-fibular junction and below any cancellous bone proximally, indicated in **Figure 5.2**. Pixels were scaled to mm using a microscope calibration slide image, and then cortical area selections and cell counting were performed in ImageJ (NIH). Cell viability was reported as the number of viable cells per mm^2 of cortical bone area. A Students T-test (non-paired, two-tail, two sample equal variance) was used to determine if there was a difference between the mean viable cell densities of the positive control bones compared to the cultured bones. Negative controls (n=3) were qualitatively assessed to verify that ‘dead’ cells or empty lacunae did not stain positively for LDH. Given the complete lack of staining in the negative controls, cells were counted as LDH+ if there was any stain present and appeared to be in a lacunae.

5.2.3 Applied Load and Strain Relationship

Characterization of the strain environment induced in the tibial segments while being loaded in compression in the biodynamic chamber were determined through a combination of empirical strain gauge measures and finite element analysis. These analyses were conducted in preparation for future in vitro studies to examine the organ culture’s response to cyclic compressive loading.

Left and right tibiae from two mice (n=4 bones) were dissected from freshly euthanized 16 week old male mice. The bones were carefully cleaned of all soft tissue, the proximal and distal ends removed with scissors at the growth plate, and then stored in PBS. Each bone was instrumented with one single element strain gauge, placed on the medial midshaft surface. The surface was prepared for gauge attachment by removing a 0.05 cm^2 region of periosteum, lightly scraping the underlying surface with a periosteal elevator, and defatting and drying the surface using 2-butanone (Sigma-Aldrich, St. Louis, MO, USA). A single element strain gauge (EA-06-015LA-120, Micro-measurements, Vishay Precision Group, LTD., Raleigh, NC, USA) was then bonded to the site using a self-catalyzing cyanoacrylate adhesive (DURO Superglue, Loctite, Westlake, OH, USA). The instrumented bone was kept moist using phosphate buffered saline throughout instrumentation and the duration of testing.

The biodynamic chambers were interfaced directly with a mechanical loading system (ElectroForce Testbench, TA Instruments, New Castle, DE, USA). Instrumented bones were placed one at a time between the two platens of the chamber and a -1N preload applied to secure the bone (**Figure 5.3**, **Figure 5.4**). Strain data were collected at 2000 Hz while each bone was loaded cyclically using a triangular waveform at 4 Hz at incrementally increasing axial compressive loads between -4N and -13.5N, similar to the loads applied during *in vivo* testing (Chapter 3 of this thesis). Multiple trials over this load range were collected for each bone. Following each trial, the bone was released from the preload and platens, and then re-secured for the subsequent trial. Care was taken to position the bone with the proximal and distal ends centered on their respective platens, and the medial surface facing up. After recognizing the potential for variation in strains for each trial if the bone after the bone had been re-secured, for the second two bones, a replicate of load and strain data was collected for each trial without re-securing the bone in order to assess the repeatability of strains once the bone had been secured. For these tests, the mean of the two trials was used in developing the relationship between load and strain. After testing, tibiae with gauges still attached were stored in 70% ethanol. A custom MATLAB (MathWorks, Natick, MA, USA) program was used to calculate peak longitudinal strain at each applied axial load. Zero strain levels were determined from the strain trace prior to the bone being secured with a preload. Peak strains were averaged over the final five load cycles for each load magnitude. For results from each bone, a linear regression analysis was performed to determine the relationship between applied compressive load magnitude and the resulting longitudinal strains, as well as if that relationship resulted in a slope greater than zero.

At a later date, bones were scanned by micro-computed tomography in 70% ethanol (µCT 40, Scanco Medical AG, Wayne, PA, USA). Any remaining wire and solder leads were carefully removed with a scalpel prior to scanning. Bones were scanned with an isotropic voxel resolution of 10 µm (55 kVp, 145 mA, 300 ms integration time, no frame averaging). An aluminum filter was used to reduce beam hardening effects. A scanner-specific calibration was performed using bone phantoms (hydroxyapatite) provided by the manufacturer in order to convert attenuation values to bone mineral density (mg HA/ccm). In each bone segment scan, the gauge was omitted during the bone contouring to prevent it from being rendered as part of the bone during model development. A threshold value was chosen to separate bone and background pixels. Three-dimensional FE mesh models with tetrahedral elements were generated using the segmented tibial microCT images and a Matlab-based mesh generation and processing program [145]. A voxel-specific modulus of elasticity was applied based on the grayscale to bone density calibration and a previously determined relationship between bone mineral density and modulus [146]. A poisons ratio of 0.3 was applied to all elements [144]. Meshed models were imported into Abaqus 6.13.3 (Simulia, Dassault Systemes, Waltham, MA, USA) where boundary conditions and the load were applied. The contact nodes on the proximal and distal cut surfaces were selected and rigidly coupled to a reference point centered in the cross-sectional area of each surface and 50µm from the surface. A new coordinate system was defined such that the primary longitudinal axis was connected to both proximal and distal reference points. The proximal surface was constrained from all translational and rotational movement along this longitudinal axis, and the distal surface was similarly constrained, except for allowing translational movement along the primary longitudinal axis. A concentrated compressive load was applied through the distal reference point. Linear elastic finite element analysis was performed in Abaqus for a simulated -10N compressive load, which represented an intermediate load level of what was tested experimentally. Each model was validated by iteratively adjusting the proximal reference point in the proximal-distal direction until modeled strains at the gauge location matched the corresponding strains measured during experimental testing at that load magnitude.

Once validated, models were used to evaluate peak principal and mean strains for two volumes of interest (VOI): 2.5% of total (pre-cut) bone length at the anatomical 37% (proximal/mid-diaphysis) and 50% (mid-diaphysis) regions along the diaphysis, relative to the proximal end of the bone. The ‘peak’ principal tensile and compressive strains were defined using the cut-off value at the 95th percentile of the range of strains induced in the VOI during loading. Since proximal and distal ends of each tibia had been removed prior to scanning by µCT, the distance from the tibia-fibular junction (TFJ) to each region was determined in microCT images from a previous set of 16 week old male mice, and that distance was used to select the appropriate regions in these bones. Similarly, the size of the volume used to represent 2.5% of bone length was determined from the prior bone scans as well. For each bone, values were extrapolated linearly from the results mean results at -10N to determine the peak and mean strains at other load levels, and therefore, standard deviations were not included at the other load levels. Finite element data from the *in vivo* tibial axial compression models (Chapter 3) was extrapolated to a -10N load in order to compare peak and mean principal strains between a tibia loaded *in vivo* and the bone segments loaded *in vitro*. Additionally, modeled cross-sectional strain distributions for 50% and 37% VOIs from representative *in vivo* (Chapter 3) and *in vitro* models were included to qualitatively assess any changes in the neutral axis orientation between loading situations.

5.3 Results

5.3.1 Bone Cell Viability

LDH staining was completed to assess osteocyte viability in bone segments after five days in culture relative to positive control bones. The mean and standard deviation for the density of viable osteocytes were determined for each tibia from the cell counts from all sections (**Table 5.1**). Overall means and standard deviations for positive controls and cultured bones were based upon the individual mean values for each bone included in the two groups (n=3, n=6 respectively). Positive control bones, stained immediately after dissection, were used to determine the density of viable cells in fresh cortical bone. The average density of viable osteocytes in the cortical diaphysis of the control bones was 689 ± 72 cells/mm^2. For the cultured bones, the mean density of viable osteocytes was 539 ± 124 cells/mm^2. Although the two samples were not statistically different (p=0.10), the mean cultured bone cell density relative to the positive controls indicates an approximately 78% cell viability rate after five days in culture.

5.3.2 Tibial Bone Segment Strain during Axial Compression

For all bones and trials, measured peak strains on the medial midshaft surface were positive, indicating that this surface of the bone was consistently loaded in tension. Strains increased in magnitude as the applied load increased, as evidenced by the significant slopes of the linear regression for each bone (**Figure 5.6**). However, the differences in peak strains between separate trials for which the bone was repositioned between trials at the same load level ranged from 100με to 1500 με depending on the bone. For the left and right bones from the second mouse, trial replicates (when loading was repeated without repositioning the bone) had average standard deviations of ±15με and ±29με, respectively. For the greatest applied load (-13.5N), peak strains at the gauge location ranged from 400 to 1600 με for one bone in particular.

5.3.3 Finite Element Modeling

Absolute peak compressive principal strains were greater than peak tensile principal strains in both the 50% and 37% volumes of interest (**Table 5.2**). The greatest strains occurred in the 37% volume, although mean strains were similar across both VOIs. Standard deviations were less than 150 με and 55 με for peak and mean principal strains, respectively, for both VOIs, which indicates that predicted mean values across the four bone samples were similar despite the discrepancy in strains measured experimentally. Based on extrapolations of peak principal strains modeled at -10N to the highest load applied empirically (-14N), peak principal compressive strains as high as -2324 με and -2656 με were reached in the 50% and 37% VOIs, respectively, at sites remote to the gauge measures (**Figure 5.8**).

Comparatively, the finite element models showed that a -10N load induced greater principal strain magnitudes during *in vivo* tibial loading relative to the *in vitro* bone segment loading (**Table 5.3**). Peak and mean principal tensile strains were 1.8-2x greater in models of whole bone loading, while peak and mean principal compressive strains were 1.5-1.6x greater during whole bone compressive loading, suggesting that removing of the epiphyses likely reduces the amount of bending that occurs at a given load magnitude and effectively stiffening the bone. Cross-sectional strain distributions showed that, despite differences in stiffness, the neutral axis orientation is fairly consistent between the whole-bone and bone segments loaded in axial compression (**Figure 5.9**).

5.4 Discussion

5.4.1 Bone Cell Viability is Maintained during Organ Culture

Cortical bone segments in culture exhibited 78% osteocyte viability relative to the positive control bones after five days in culture. The LDH assay has previously been used to assess cell viability during embryonic bone organ cultures and cancellous bone explants [186, 191, 203]. Some studies using embryonic bone or cancellous bone explants have reported lower cell viabilities after their respective culture periods, but have successfully identified RNA and growth factor secretion responses to mechanical stimulation [186, 191], so we believe our osteocyte cell viability is sufficient for continued use of this model. Although we only quantitatively assessed osteocyte cell viability in cortical bone proximal to the TFJ and below any cancellous bone, qualitative observations of cortical bone areas both distal and proximal also showed good cell survival after five days in culture for all samples. Previous studies in mature cancellous bone explants have shown improved cell viability with mechanical loading [190, 191], so future mechanically loaded cortical bone segments in culture may retain even greater cell viability than 78% after five days, although this could affect results from the non-loaded control bones in future studies. Mechanical loading likely improves cell viability by increasing fluid flux through the lacunar-canalicular system to distribute nutrients and remove waste [204, 205].

While we completed the cell viability validation for the mouse tibia in culture, it seems reasonable to expect that other long bones could also be used successfully in this model. The murine tibia and the ulna have been used for the majority of *in vivo* studies likely because their position in the respective limbs allows load to be applied axially and non-invasively to the bone, which would not be possible with bones such as the femur or humerus. Ultimately, the only limitations to bone selection are length and cross-sectional diameter of the chosen segment, as the piston ends that hold the segment in place are 10 mm in diameter and the chamber length is 12.5 cm. It also seems possible that isolated trabecular bone segments could be used successfully in this model. Although some trabecular bone remains in the proximal and distal ends of our tibial segment, the majority is removed when the epiphyses are cut during the initial processing steps. Trabecular bone is often of significant interest to researchers since it is significantly impacted by osteoporosis [206-208]. This model could provide a new way to study isolated trabecular bone under various fluid flow, mechanical load, and media chemistry composition conditions.

5.4.2 Mechanical Loading of Cortical Bone Segments *In Vitro*

Tibial bone segments could successfully undergo axial compressive loading within the biodynamic chamber, and the induced strain environment was characterized via direct measurements (strain gauges) and finite element modeling. A concern prior to attempting to apply an axial compressive load to a murine tibial bone segment using the biodynamic chamber was that due to the shape of their tibiae, high loads would cause a bending moment significant enough that the bone would not stay secured between the platens. This problem was not realized for any of the bones tested up to a compressive load of -13.5N. A single user secured each bone between the platens for all tests with the intention to install the bone in the same position each time.

A novel benefit to using cortical bone segments compared to cancellous bone explants was the ability to directly measure strains induced to the bone segment during axial compressive loading in the culture chamber. Due to the shape of the tibia, imperceptible changes in the bone's orientation following repositioning did cause similar magnitudes of axially compressive load to induce strain ranges at the gauge position of up to ±625με from the mean at the highest load. The variability in orientation of the cut proximal and distal surfaces, as well as the uneven porous surfaces between which the bone is secured potentially also played a role in strain discrepancies between trials. Once a bone was secured between the platens though, strain magnitudes were repeatable for multiple trials, indicated by the low standard deviations within trial replicates for the second set of left and right tibial segments. During a culture period, the bone segments would not be re-orientated, so once a bone is initially secured between the platens, the resulting strain profile should not vary from day to day of applied loading.

Given some variability in how the tibiae may have been cut and positioned in the chamber fixtures, finite element models were validated individually in order to recreate the strain profile determined by the average stiffness measure for each bone across all load magnitudes and trials. Individual validations allowed assessment of the peak strain similarities across the four bones while accounting for variation in how each bone was oriented during experimental loading. The variation in the strains measured empirically across the four bones likely represents normal variation that would occur during future loaded bone organ culture experiments. Despite the variation in peak strains at the gauge location across the bones during experimental loading, the mean and peak principal strains at the 50% and 37% VOI's predicted by the models indicate that the gross strain profile was actually fairly repeatable across the sample size. It seems possible that the variation in longitudinal strains measured experimentally across bones was likely due to a combination of gauge position on the bone and small variations in the precise orientation of the bone between the platens. Validated computational characterization of the strain profile induced throughout the cortical bone segment will provide a significant advantage for this model compared to embryonic and cancellous bone cultures when it comes to relating the response to the stimulus in future studies.

5.4.3 Strain Induced *In Vivo* vs. *In Vitro* in the Murine Tibia under Axial Compressive Loading

Bone stiffness during axial compressive loading was higher in the bone segments compared to intact tibiae loaded *in vivo*, but the neutral axis positions were fairly similar between cases indicating that the overall bending orientations were similar. Removing the epiphyses shortens the whole bone and reduces the curvature primarily on the proximal 50% of the bone, which results in decreased load-induced bending and therefore, lower strains at a given load magnitude. An applied load between -16N and -18N would be necessary to induce peak strains in the bone segment similar to peak strains induced by a -10N load applied to an intact hind limb loaded *in vivo*. Maintaining a similar strain profile between axial compressive loading of the bone segment and of an intact hind limb *in vivo* is important because a bone's sensitivity and adaptive response to load is dependent on the change in strains induced by the experimentally applied load relative to the strains induced during physiologic activities [51]. Additionally, differences in strain profile would make interpretation of organ culture results relative to *in vivo* studies difficult. Based on modeling results for both cases though, it seems that increasing the load magnitude will effectively compensate for the increased stiffness of the bone segment while maintaining a similar strain profile, at least for the mouse tibia.

In vivo bone adaptation studies typically run 2-4 weeks in order for a tissue level response to occur that is significant enough to measure by microCT or histomorphometry, but studies have shown that *in vivo* and *in vitro* cellular responses to mechanical or chemical stimulation of a bone or bone cells can be detected as early as hours after a single load bout [74, 75, 118, 188, 189, 194, 195, 209]. Therefore, our five day survival time point is relevant for assessing a bone's response to a mechanical stimulus. Studies similar to those conducted *in vivo* could be repeated with this organ culture model to assess RNA expression and factor secretion into the media without the potentially confounding effects of systemic physiology. Although complete removal of systemic factors does not provide specific information about the effects of the systemic factors individually, future use of this organ culture system could also re-introduce controlled levels of hormones or growth factors to assess the effects of each on the skeletal response to mechanical stimuli independently. Furthermore, with this model, mechanical stimulation could include both axially compressive loads as well as changes in fluid flow rate. The biodynamic chamber interacts with the same mechanical loading device that has been used for my *in vivo* studies, so the same parameters can be adjusted including load magnitude, waveform, load rate, and cycle frequency.

In conclusion, we were able to validate adequate survival of osteocytes within the mineralized matrix of murine tibial bone segments for five days in culture, and successfully apply axial compressive load to the bone segment within the culture chamber as a preliminary mechanical characterization for future organ culture loading studies. Using cortical bone segments allowed us to fully characterize the strain environment induced using both experimental measurements and finite element models, something that has not been done with previously published embryonic and cancellous bone *in vitro* models. With the developed relationship between compressive loads applied to the bone segment and the resulting strain profile, bone segments can be stimulated similar to *in vivo* murine tibial loading studies while gaining more control over systemic chemical factors. While our interest in developing this model was to be able to compare the skeletal response to load across vertebrate species in a more controlled environment than *in vivo* studies allow, this validation opens the model up to a large variety of basic science and biomedically motivated experiments.

Table 5.1 Bone cell viability results for the positive controls and cultured bone segments. Total bone area analyzed (mm^2), total number of LDH+ cells counted, and the average number of LDH+ cells per mm^2 of cortical bone ± one standard deviation of are presented. For each set of samples, the mean number of LDH+ cells/mm^2 ± one standard deviation of the sample means are also shown in bold.

Sample Type	Sample	Total Bone Area Analyzed (mm^2)	Number of LDH+ cells counted	Cells/mm^2		
Cultured bones	1	0.970	502	513	±	123
	2	1.024	560	532	±	178
	3	1.034	492	498	±	126
	4	1.185	485	393	±	113
	5	0.846	600	769	±	383
	6	0.949	484	531	±	146
				539	±	**124**
Positive Controls	1	0.7	504	717	±	161
	2	0.841	483	607	±	137
	3	0.666	494	742	±	195
				689	±	**72**

Table 5.2 Modeled peak (represented by the 95th percentile) and mean principal strains (με) for volumes at 37% and 50% of anatomical bone length for a load of -10N.

Cortical Cross-Section Strains			
		37%	50%
Principal Tension	95th percentile	737 ± 97	841 ± 143
	Mean	407 ± 39	393 ± 44
Principal Compression	95th percentile	-1897 ± 143	-1659 ± 113
	Mean	-728 ± 43	-742 ± 52

Table 5.3 Modeled peak (represented by the 95th percentile) and mean principal strains (με) for volumes at 37% and 50% of anatomical bone length for a simulated load of -10N for the bone segments used for organ culture and the whole bone in vivo models presented in Chapter 1 of this thesis. Values were extrapolated for the *in vivo* models, and therefore standard deviations were not relevant; standard deviations were omitted for the bone segment results for clarity but can be found in Table x.

		37%		50%	
		Bone Segment	*In Vivo*	Bone Segment	*In Vivo*
Principal Tension	95th percentile	737	1529	841	1600
	Mean	407	800	393	707
Principal Compression	95th percentile	-1897	-3071	-1659	-2502
	Mean	-728	-1085	-742	-1037

\

Figure 5.1 Image showing the flow loop between the reservoir bottle and the chamber.

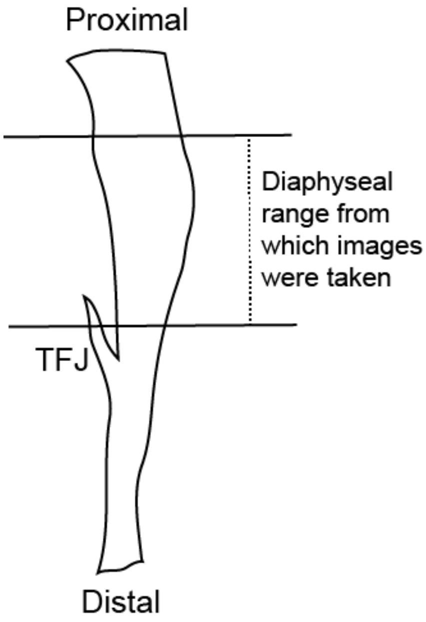

Figure 5.2 Diagram indicating the acceptable region around the midshaft from which cortical bone images were taken to assess cell viability via LDH+ staining.

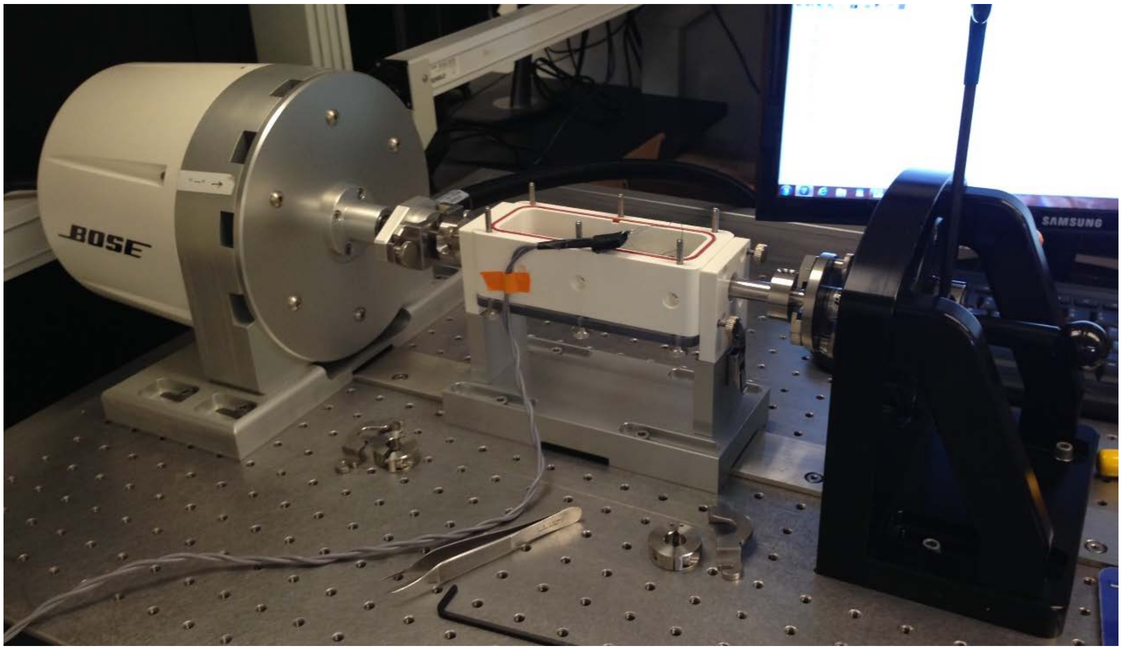

Figure 5.3 Image showing a biodynamic chamber interfaced with the Bose Testbench mechanical loading system. Prior to connecting each side of the chamber to the loading device, it is secured in a horizontal orientation to the breadboard so that the chamber itself remains stationary at all times. During loading, the shaft locks are removed on each side so that one shaft can be axially controlled by the actuator (left) and the other shaft can transmit load to the load cell (right).

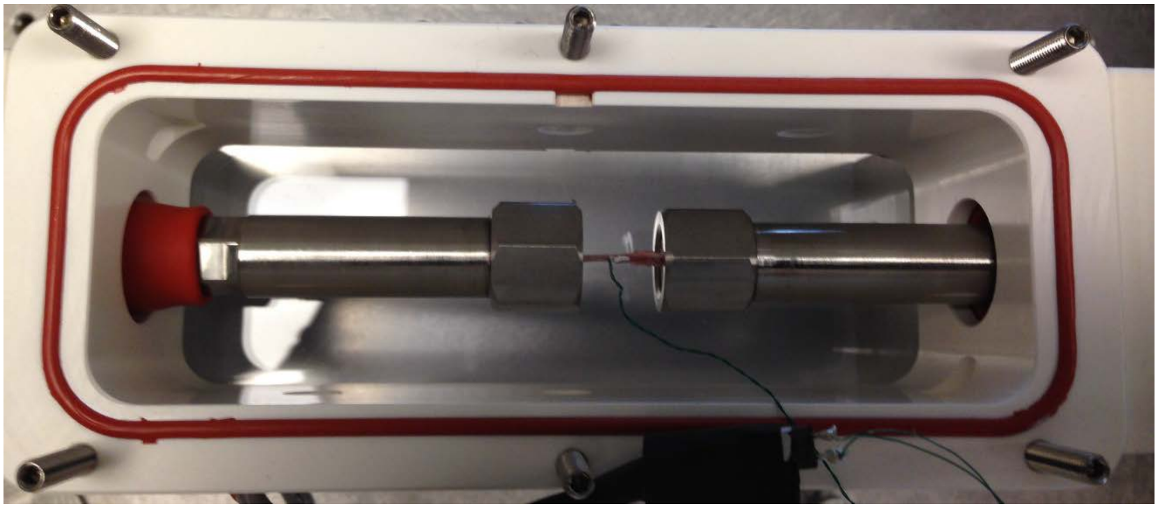

Figure 5.4 Image depicting a gauged bone segment being held in the biodynamic chamber.

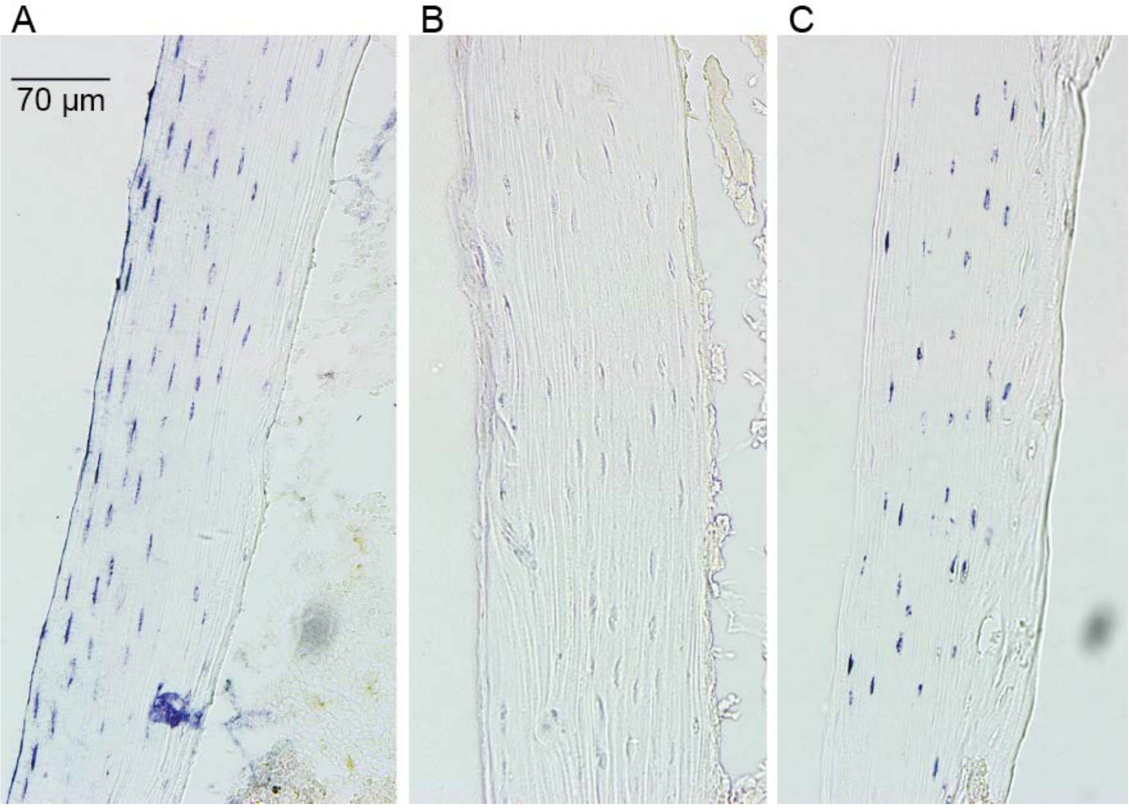

Figure 5.5 Representative images of LDH stained bone samples for a (A) positive control, (B) negative control, and (C) cultured bone segment. Purple/blue staining indicates a LDH+ cell. Scale bar shown in panel A applies to panels B and C as well.

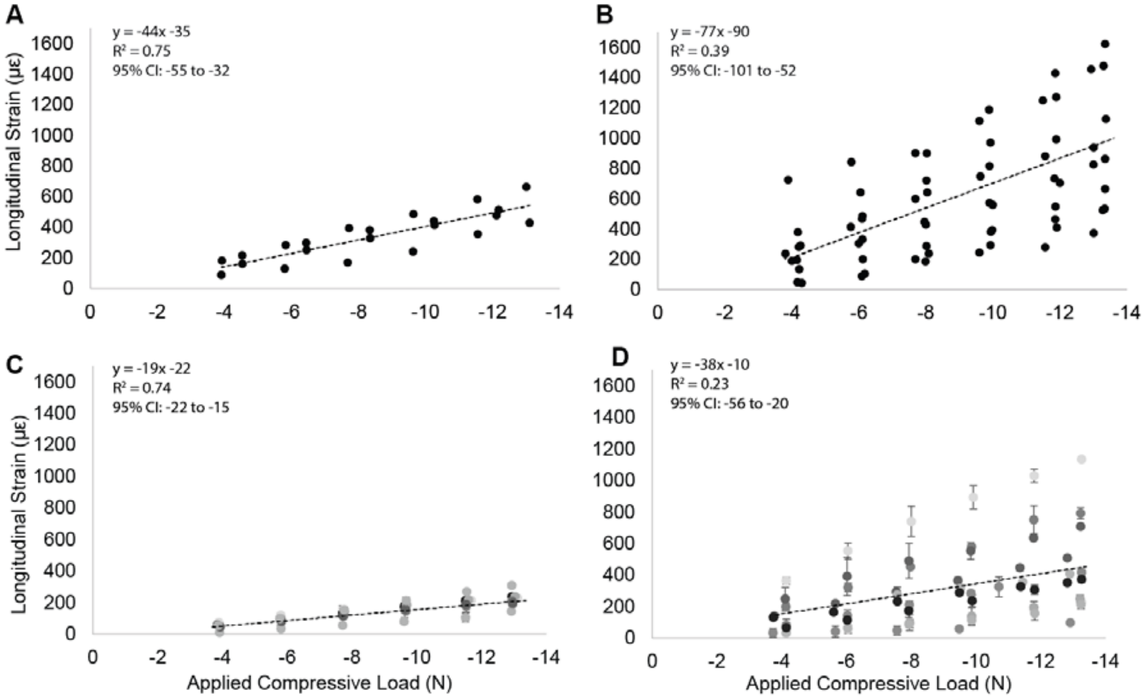

Figure 5.6 Longitudinal strains on the medial midshaft surface of left and right tibial bone segments under axial compression applied through the platens of the biodynamic chamber.Each plot represents a single bone and the trials performed (A: mouse 1-left, B: mouse 1-right, C: mouse 2-left, D: mouse 2-right). The linear regression, R^2, and 95% slope confidence interval values are shown in each subplot. For C and D, data points and error bars represent the mean ± standard deviation for the two replicates of each trial.

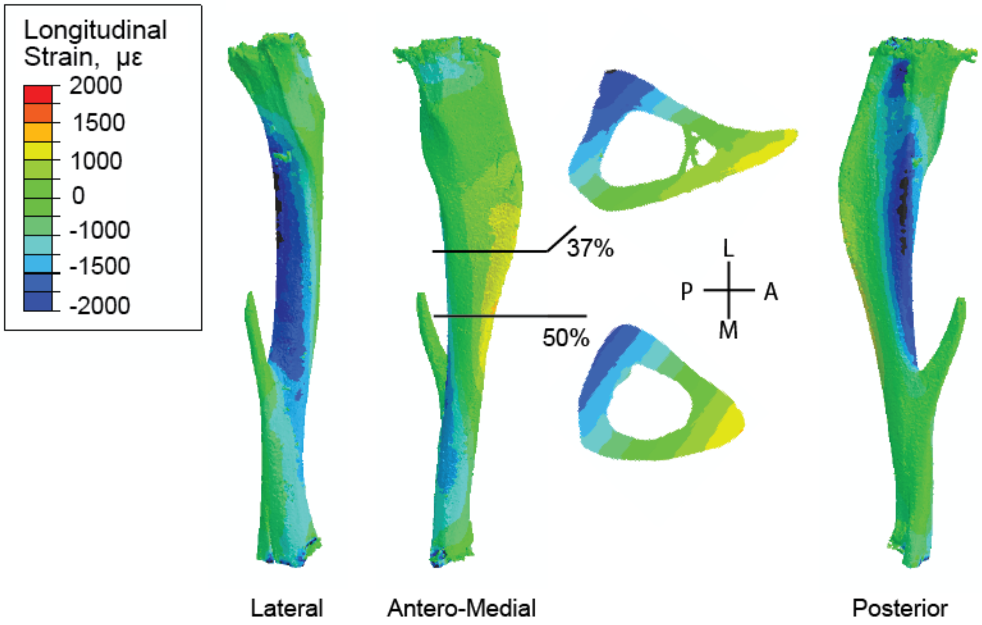

Figure 5.7 Representative finite element model images of the mouse tibial bone segment under a simulated -10N axial compressive load.Images depict longitudinal strain distributions (με) on the lateral, antero-medial, and posterior surfaces of the bone segment from left to right. Cross-sectional strain distributions at 37% and 50% relative to the proximal end of the bone are shown as well.

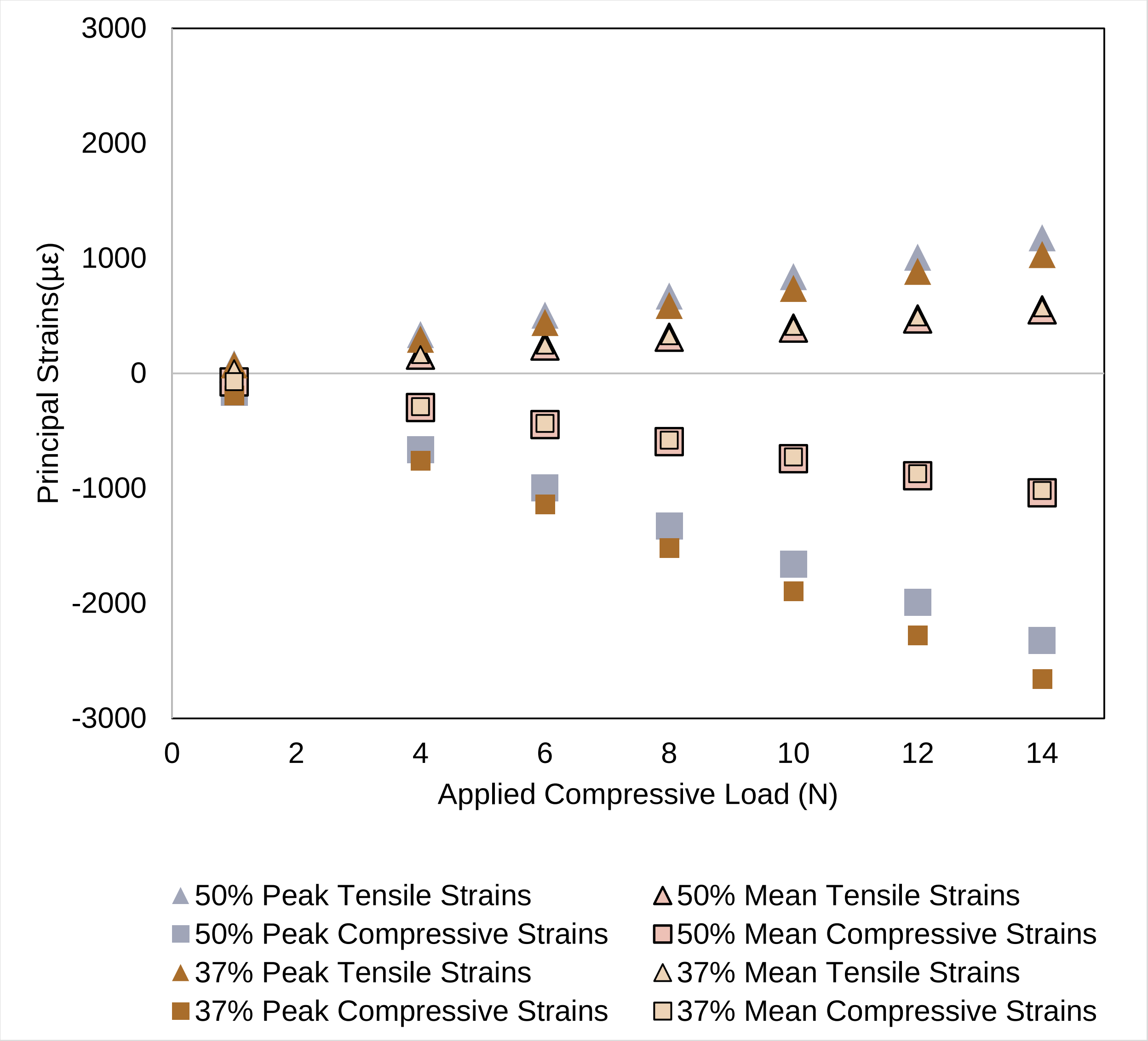

Figure 5.8 Plot indicating the finite element model-based extrapolated peak and mean principal tensile and compressive strains (με) for axial compressive loads ranging from -1N to -14N. Boxes represent compressive strains while triangles represent tensile strains. Green points indicate strains in the 37% VOI while blue points indicate strains in the 50% VOI.

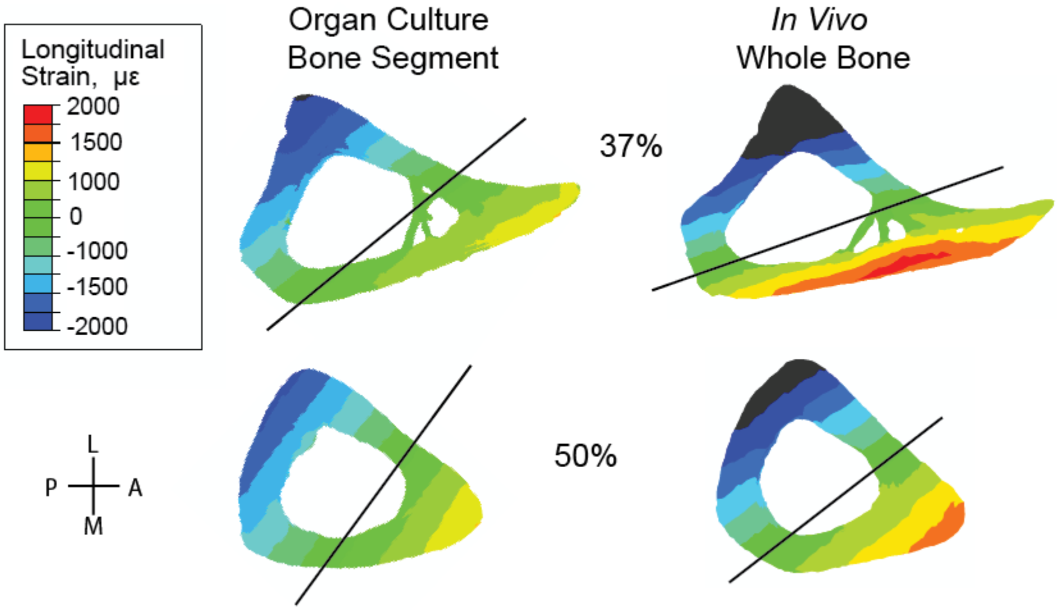

Figure 5.9 Finite element modeled representative cross-sectional longitudinal strain (με) distributions for a bone segment and for the tibia of an intact hind limb loaded in vivo, both with simulated compressive loads of -10N. Cross-sections are shown for VOIs at anatomical 37% and 50% of bone length relative to the proximal end of the bone. The black line over each cross-section represents the location and orientation of the neutral axis for each respective case.

6. CONCLUSIONS AND FUTURE DIRECTIONS

It has long been recognized that the healthy skeleton has mechanobiological mechanisms that self-regulate its mass and structure based on day-to-day mechanical input in order to minimize fracture risk. Failure of these mechanisms results in skeletal diseases, such as osteoporosis, that affect millions of people each year. Studying the skeletons anabolic response to mechanical stimuli using rodent models has significantly improved our ability to develop better preventative and remedial treatments. However, the rodent skeleton does not represent vertebrates as a whole (or even the human skeleton), and sole use of those models will continue to propagate a gap in our understanding of skeletal response to mechanical stimuli more broadly. The work in this dissertation was structured to validate biomechanical techniques (Chapter 2) and to develop new animal (Chapters 3 and 4) and *in vitro* models (Chapter 5) in order to begin addressing the large gap in the field regarding skeletal sensitivity and adaptation in vertebrate species beyond the common rodent models.

In chapter 2, we validated the use of planar strain theory (PST), which predicts cross-sectional strain distributions based on three longitudinal strain measures, for use on cortical bone. This theory has been used frequently to evaluate the diversity of skeletal loading regimes in vertebrate long bones during locomotion, but the application of this theory to skeletal mechanics had not been previously validated experimentally. PST assumes that cortical bone is linearly elastic, isotropic in the transverse plane of section, and has a perfectly cylindrical cross-section. To validate the use of PST on bone, emu tibiotarsi were instrumented with four rosette strain gauges and then loaded in four point bending *ex vivo*. Measures from three gauges were used to predict strains at the fourth gauge site, and each prediction was validated against the experimental measures. We found that for all four gauge sites tested, not only did measured and predicted longitudinal strains match closely, gauge distribution around the cross section had only a small effect on the confidence intervals of our predictions. Our results indicate that PST predictions appear to be relatively insensitive to the presence of a marrow canal and the bone tissue heterogeneity likely present in the bones we tested. Validating this technique was of interest for this thesis because we intended to use PST during the development of a new avian tibiotarsus loading model to determine the similarity of the cross-sectional strain distributions induced between experimentally applied loading conditions and locomotion. Unfortunately, due to size and cross-sectional geometry, this technique cannot be used on mouse tibiae *in vivo*. A limitation to this work was that we assessed PST in bones *ex vivo* under pure bending conditions, but it is likely that during locomotion, a bone is loaded in a combination of bending, compression and torsion, and it is unknown what effects combinations of those loads may have on PST predictions.

Chapters 3 and 4 were complementary in the development of our murine and novel avian skeletal loading models in that the former characterized the *in vivo* bone strains during locomotion and axial loading necessary to apply similar relative loads, and the later utilized those load levels to assess the multi-week cortical bone response for each species. In Chapter 3, *in vivo* bone strain measurements during locomotion and experimentally applied loading were complemented by specimen-specific finite element models. One of the prominent results of the comprehensive strain characterizations was how differences in whole-bone geometry between the mouse tibia and the chukar partridge TBT led to largely different strain profiles and peak strain locations under axial compressive loads. The diaphysis of the chukar TBT is relatively straight, with the most significant curvatures occurring at the metaphyses. Fracture failure occurred in multiple birds as we attempted to increase our load magnitude to achieve higher peak strains at the midshaft, so we were ultimately limited in the increase in strains we could achieve at the midshaft relative to peak strains during locomotion. Although loads up to -13N have been used successfully to generate a significant woven bone response for the mouse tibial loading model (previous unpublished results from author), our desire to compare the response between species ultimately limited our load magnitude for the mouse as well. In the end, we applied experimental loads inducing 2.5x peak strains during locomotion on the medial midshaft surface of the tibia/TBT for both species. The birds also experienced significant soft tissue damage at the knee and ankle as a result of daily loading, such that our planned four week study was cut short by one week.

Despite the issues we experienced while developing our avian loading model, our multi-week loading study results at the midshaft suggest that while the mouse tibia increased its bone mass in addition to changes in cross-sectional geometry in response to loading, the bird TBT only adapted its geometry and the load actually seemed to suppress natural endosteal growth. Based on the models though, despite similar relative increases in strain on the medial midshaft surface, peak principal compressive strains were approximately 400$\mu\varepsilon$ lower in the midshaft volume of interest for the bird compared to the mouse, so our assessment of the response is based solely on the increase in strain relative to during locomotion. The finite element models of the mouse tibia and the chukar TBT suggested that the volumes of bone with the most similar peak principal compressive strain magnitudes were the 37% volume for the mouse and the 90% volume for chukar, but at these regions, an increase in maximum moment of inertia was measured at 37% for the mouse, while no statistically significant response was measured at 90% for the chukar. In Chapter 4, we also used the CFU-OB assay to assess mineral production from similar starting volumes of marrow cells. While the biological significance of quantitative differences in mineral produced by 2 million but not 1 million starting cell volumes of marrow cells was not clear, the colonies that formed for each species were qualitatively quite different. These differences suggest that there were innate differences in the osteoblast progenitor cells before they were isolated from the animal, possibly indicating inherent cellular differences between the species.

In chapter 5, we developed and validated a novel *in vitro* model to culture murine tibial cortical bone segments that can be mechanically loaded in axial compression, similar to current popular *in vivo* tibial loading models. This model was designed so that future studies could assess the response to load of cortical bone from various vertebrate species while removed from potentially confounding systemic factors including metabolism, growth factors, hormones, etc. Currently available models include embryonic and cancellous explants, however both had limitations that would prevent a user from assessing a response relative to an applied load, a particularly important aspect to consider when the ultimate goal is comparing skeletal sensitivity across species. For mouse tibial segments, we validated osteocyte viability at 78% after five days in culture, and we suspect that future studies involving mechanical loading of the bones may help to retain even higher viability. Additionally, we used similar methods to Chapter 3 (strain gauge measurements, finite element models, and planar strain theory) to show that peak principal strains were repeatable across multiple bone segments in two volumes of interest, that a similar cross-sectional strain distribution relative to *in vivo* loading is retained, and that simply increasing the load magnitude will compensate for the increased stiffness of the mouse tibial segment loaded *in vitro* relative to the *in vivo* loading situation. Future studies could assess a bone’s response to load via genetic regulation, factors released in the media, or possibly even gross changes in tissue mass and geometry. While our interest in developing this model was to be able to compare the skeletal response to load across vertebrate species in a more controlled environment than *in vivo* studies allow, we foresee this model being relevant for a large variety of basic science and biomedically motivated experiments.

In general, the chukar partridge tibiotarsal loading model developed in these chapters represents a novel non-invasive loading model utilizing an avian species. The functionally isolated turkey ulnar loading model was used often back in the 1980s, but it is unclear how the invasiveness and non-physiologic loading pattern may have confounded any results. The size of the chukar TBT makes it possible to instrument with three strain gauges for *in vivo* characterizations, a significant benefit over the rodent models, who are typically only instrumented with one. Using planar strain theory, we were able to compare the cross-sectional strain distribution between locomotion and experimentally applied loads using *in vivo* measured values, something that has not been previously done for the rodent models. Not only do a minimum of three measurements allow cross-sectional strain characterizations, validations of finite element models are more comprehensive. The chukar partridge is also a bipedal animal model that exhibits haversian remodeling, making it more similar to humans than the rodents in at least a few known aspects.

Since the overarching goal of this work was to begin assessing skeletal sensitivity and response to load across vertebrate species, future studies should seek to increase the number of species assessed. Although determining the sensitivity of the skeleton to a specific increase in strain is of interest, which can be done if a specific bone region is selected (such as the midshaft), development of the bird model demonstrated that differences in whole-bone geometry could make achieving similar strains at a specific location difficult across multiple species. Ultimately, it may be more feasible to assess the adaptive response relative to the absolute strain stimuli predicted by the models at the various regions of the bone rather than relative to peak strains measured during physiologic activities. Alternatively, loading methods such as 4-point bending could be used to achieve more consistent strain distributions during experimental loading across species, but the potentially less physiologic strain distribution induced and the effects of the load contact points being close to the region of interest could confound any comparative assessments across the species. Therefore, investigators must carefully choose the loading method and magnitude depending on what outcomes they are hoping to assess across species, because the issues we experienced with the bird model could occur in other species as well.

In addition to assessing the tissue-level response to load across species, future studies should also delve into the cellular, genetic, and systemic mechanisms responsible for any differences seen across species. Our early work shows that there are differences in the skeleton's response to load across avian and rodent species, implying there must be mechanistic differences as well. We have set up a novel cortical bone organ culture model in which bone's response to mechanical load can be studied *in vitro* without the confounding effects of various levels of systemic factors. We believe this model will be very useful in determining how differences in innate cell populations and networks across vertebrate species may affect their ability to sense and respond to mechanical stimuli. Characterizing genetic regulation after varied amounts of loading could also provide insight into mechanistic variations and their tissue-level effect on the skeleton. Such insight could allow researchers to make more informed pharmaceutical targets to aid in preventing and treating skeletal diseases such as osteoporosis. Ultimately, we hope the work presented in this thesis grows the interest in studying skeletal adaptation in a variety of vertebrate species both to further enhance our basic understanding of skeletal biology as well as to better inform biomedical advancements for treating skeletal disease.

REFERENCES

[1] D.M. Cullinane, T.A. Einhorn, Biomechanics of bone, Principles of bone biology 1 (2002) 17-32.

[2] T. Katagiri, N. Takahashi, Regulatory mechanisms of osteoblast and osteoclast differentiation, Oral Dis 8(3) (2002) 147-59.

[3] S.P. Fritton, S. Weinbaum, Fluid and Solute Transport in Bone: Flow-Induced Mechanotransduction, Annu Rev Fluid Mech 41 (2009) 347-374.

[4] L.E. Lanyon, Osteocytes, strain detection, bone modeling and remodeling, Calcif Tissue Int 53 Suppl 1 (1993) S102-6; discussion S106-7.

[5] Osteoporosis Prevention, Diagnosis, and Therapy., NIH Consens Statement, 2000, pp. 1-36.

[6] National Institute of Arthritis and Musculoskeletal and Skin Diseases: "Osteoporosis.".

[7] L.J. Melton, Adverse outcomes of osteoporotic fractures in the general population, J Bone Miner Res 18(6) (2003) 1139-41.

[8] S. Khosla, S. Amin, E. Orwoll, Osteoporosis in men, Endocr Rev 29(4) (2008) 441-64.

[9] L. Vico, M.H. Lafage-Proust, C. Alexandre, Effects of gravitational changes on the bone system in vitro and in vivo, Bone 22(5 Suppl) (1998) 95S-100S.

[10] T. Lang, A. LeBlanc, H. Evans, Y. Lu, H. Genant, A. Yu, Cortical and trabecular bone mineral loss from the spine and hip in long-duration spaceflight, J Bone Miner Res 19(6) (2004) 1006-1012.

[11] J.E. Zerwekh, L.A. Ruml, F. Gottschalk, C.Y.C. Pak, The Effects of Twelve Weeks of Bed Rest on Bone Histology, Biochemical Markers of Bone Turnover, and Calcium Homeostasis in Eleven Normal Subjects, J Bone Miner Res 13(10) (1998) 1594-1601.

[12] H. Sievänen, Immobilization and bone structure in humans, Arch. Biochem. Biophys. 503(1) (2010) 146-152.

[13] G.D. Roodman, J.J. Windle, Paget disease of bone, J Clin Invest 115(2) (2005) 200-208.

[14] A. Morales-Piga, J. Rey-Rey, J. Corres-González, Í.S. Garc, G. LÓPez-Abente, Frequency and characteristics of familial aggregation of Paget's disease of bone, J Bone Miner Res 10(4) (1995) 663-670.

[15] T. Van Staa, P. Selby, H. Leufkens, K. Lyles, J. Sprafka, C. Cooper, Incidence and natural history of Paget's disease of bone in England and Wales, Journal of Bone and Mineral Research 17(3) (2002) 465-471.

[16] R.P. Heaney, Nutritional factors in osteoporosis, Annu. Rev. Nutr. 13(1) (1993) 287-316.

[17] J.R. Tucci, R.P. Tonino, R.D. Emkey, C.A. Peverly, U. Kher, A.C. Santora, U.A.P.I.O.T.S. Group, Effect of three years of oral alendronate treatment in postmenopausal women with osteoporosis, Am J Med 101(5) (1996) 488-501.

[18] S.R. Cummings, D.B. Karpf, F. Harris, H.K. Genant, K. Ensrud, A.Z. LaCroix, D.M. Black, Improvement in spine bone density and reduction in risk of vertebral fractures during treatment with antiresorptive drugs, Am J Med 112(4) (2002) 281-289.

[19] B. Ettinger, D.M. Black, B.H. Mitlak, R.K. Knickerbocker, T. Nickelsen, H.K. Genant, C. Christiansen, P.D. Delmas, J.R. Zanchetta, J. Stakkestad, Reduction of vertebral fracture risk in postmenopausal women with osteoporosis treated with raloxifene: results from a 3-year randomized clinical trial, Jama 282(7) (1999) 637-645.

[20] E.G. Lufkin, H.W. Wahner, W.M. O'Fallon, S.F. Hodgson, M.A. Kotowicz, A.W. Lane, H.L. Judd, R.H. Caplan, B.L. Riggs, Treatment of postmenopausal osteoporosis with transdermal estrogen, Ann. Intern. Med. 117(1) (1992) 1-9.

[21] P.D. Delmas, N.H. Bjarnason, B.H. Mitlak, A.-C. Ravoux, A.S. Shah, W.J. Huster, M. Draper, C. Christiansen, Effects of raloxifene on bone mineral density, serum cholesterol concentrations, and uterine endometrium in postmenopausal women, N Engl J Med 337(23) (1997) 1641-1647.

[22] A.B. Hodsman, D.C. Bauer, D.W. Dempster, L. Dian, D.A. Hanley, S.T. Harris, D.L. Kendler, M.R. McClung, P.D. Miller, W.P. Olszynski, Parathyroid hormone and teriparatide for the treatment of osteoporosis: a review of the evidence and suggested guidelines for its use, Endocr Rev 26(5) (2005) 688-703.

[23] J. Wolff, P. Maquet, R. Furlong, The law of bone remodelling, Springer-Verlag Berlin1986.

[24] C.T. Rubin, L.E. Lanyon, Regulation of bone mass by mechanical strain magnitude, Calcif Tissue Int 37(4) (1985) 411-7.

[25] A.A. Biewener, S.M. Swartz, J.E. Bertram, Bone modeling during growth: dynamic strain equilibrium in the chick tibiotarsus, Calcified Tissue International 39(6) (1986) 390-5.

[26] T.S. Gross, K.J. McLeod, C.T. Rubin, Characterizing bone strain distributions in vivo using three triple rosette strain gages, J Biomech 25(9) (1992) 1081-7.

[27] D.M. Nunamaker, D.M. Butterweck, M.T. Provost, Fatigue fractures in thoroughbred racehorses: relationships with age, peak bone strain, and training, J Orthop Res 8(4) (1990) 604-11.

[28] L.E. Lanyon, S. Bourn, The influence of mechanical function on the development and remodeling of the tibia. An experimental study in sheep, J Bone Joint Surg Am 61(2) (1979) 263-73.

[29] C.T. Rubin, L.E. Lanyon, Limb mechanics as a function of speed and gait: a study of functional strains in the radius and tibia of horse and dog, J Exp Biol 101 (1982) 187-211.

[30] J.R. Mosley, B.M. March, J. Lynch, L.E. Lanyon, Strain magnitude related changes in whole bone architecture in growing rats, Bone 20(3) (1997) 191-8.

[31] Y. Kodama, Y. Umemura, S. Nagasawa, W.G. Beamer, L.R. Donahue, C.R. Rosen, D.J. Baylink, J.R. Farley, Exercise and mechanical loading increase periosteal bone formation and whole bone strength in C57BL/6J mice but not in C3H/Hej mice, Calcif Tissue Int 66(4) (2000) 298-306.

[32] C.T. Rubin, L.E. Lanyon, Dynamic strain similarity in vertebrates; an alternative to allometric limb bone scaling, J Theor Biol 107(2) (1984) 321-7.

[33] S.P. Fritton, K.J. McLeod, C.T. Rubin, Quantifying the strain history of bone: spatial uniformity and self-similarity of low-magnitude strains, J Biomech 33(3) (2000) 317-25.

[34] R.L. De Souza, M. Matsuura, F. Eckstein, S.C. Rawlinson, L.E. Lanyon, A.A. Pitsillides, Non-invasive axial loading of mouse tibiae increases cortical bone formation and modifies trabecular organization: a new model to study cortical and cancellous compartments in a single loaded element, Bone 37(6) (2005) 810-8.

[35] M.E. Lynch, R.P. Main, Q. Xu, D.J. Walsh, M.B. Schaffler, T.M. Wright, M.C. van der Meulen, Cancellous bone adaptation to tibial compression is not sex dependent in growing mice, J Appl Physiol (1985) 109(3) (2010) 685-91.

[36] T.D. Brown, D.R. Pedersen, M.L. Gray, R.A. Brand, C.T. Rubin, Toward an identification of mechanical parameters initiating periosteal remodeling: a combined experimental and analytic approach, J Biomech 23(9) (1990) 893-905.

[37] G.H. van Lenthe, R. Müller, Prediction of failure load using micro-finite element analysis models: Toward in vivo strength assessment, Drug Discov Today Technol 3(2) (2006) 221-9.

[38] A. Torcasio, X. Zhang, J. Duyck, G.H. van Lenthe, 3D characterization of bone strains in the rat tibia loading model, Biomech Model Mechanobiol 11(3-4) (2012) 403-10.

[39] H. Yang, K.D. Butz, D. Duffy, G.L. Niebur, E.A. Nauman, R.P. Main, Characterization of Cancellous and Cortical Bone Strain in the in vivo Mouse Tibial Loading Model Using MicroCT-Based Finite Element Analysis, Bone (66) (2014) 131-139.

[40] M.P. Akhter, D.M. Raab, C.H. Turner, D.B. Kimmel, R.R. Recker, Characterization of in vivo strain in the rat tibia during external application of a four-point bending load, J Biomech 25(10) (1992) 1241-6.

[41] F.M. Lambers, G. Kuhn, C. Weigt, K.M. Koch, F.A. Schulte, R. Müller, Bone adaptation to cyclic loading in murine caudal vertebrae is maintained with age and directly correlated to the local micromechanical environment, J Biomech 48(6) (2015) 1179-1187.

[42] T.S. Gross, J.L. Edwards, K.J. McLeod, C.T. Rubin, Strain gradients correlate with sites of periosteal bone formation, J Bone Miner Res 12(6) (1997) 982-8.

[43] Y. Umemura, T. Ishiko, T. Yamauchi, M. Kurono, S. Mashiko, Five jumps per day increase bone mass and breaking force in rats, J Bone Miner Res 12(9) (1997) 1480-1485.

[44] K.J. Hart, J.M. Shaw, E. Vajda, M. Hegsted, S.C. Miller, Swim-trained rats have greater bone mass, density, strength, and dynamics, J Appl Physiol (1985) 91(4) (2001) 1663-8.

[45] R.K. Fuchs, J.J. Bauer, C.M. Snow, Jumping improves hip and lumbar spine bone mass in prepubescent children: a randomized controlled trial, J Bone Miner Res 16(1) (2001) 148-56.

[46] C. Snow, D. Williams, J. LaRiviere, R. Fuchs, T. Robinson, Bone gains and losses follow seasonal training and detraining in gymnasts, Calcif. Tissue Int. 69(1) (2001) 7-12.

[47] L.E. Lanyon, C.T. Rubin, Static vs dynamic loads as an influence on bone remodelling, Journal of Biomechanics 17(12) (1984) 897-905.

[48] A.G. Torrance, J.R. Mosley, R.F. Suswillo, L.E. Lanyon, Noninvasive loading of the rat ulna in vivo induces a strain-related modeling response uncomplicated by trauma or periostal pressure, Calcif Tissue Int 54(3) (1994) 241-7.

[49] Y.F. Hsieh, A.G. Robling, W.T. Ambrosius, D.B. Burr, C.H. Turner, Mechanical loading of diaphyseal bone in vivo: the strain threshold for an osteogenic response varies with location, J Bone Miner Res 16(12) (2001) 2291-7.

[50] C.T. Rubin, L.E. Lanyon, Regulation of bone formation by applied dynamic loads, J Bone Joint Surg Am 66(3) (1984) 397-402.

[51] T. Sugiyama, L.B. Meakin, W.J. Browne, G.L. Galea, J.S. Price, L.E. Lanyon, Bones' adaptive response to mechanical loading is essentially linear between the low strains associated with disuse and the high strains associated with the lamellar/woven bone transition, Journal of Bone and Mineral Research 27(8) (2012) 1784-93.

[52] J.R. Mosley, L.E. Lanyon, Strain rate as a controlling influence on adaptive modeling in response to dynamic loading of the ulna in growing male rats, Bone 23(4) (1998) 313-8.

[53] C.H. Turner, I. Owan, Y. Takano, Mechanotransduction in bone: role of strain rate, Am J Physiol 269(3 Pt 1) (1995) E438-42.

[54] Y.F. Hsieh, C.H. Turner, Effects of loading frequency on mechanically induced bone formation, J Bone Miner Res 16(5) (2001) 918-24.

[55] A.G. Robling, D.B. Burr, C.H. Turner, Recovery periods restore mechanosensitivity to dynamically loaded bone, J Exp Biol 204(Pt 19) (2001) 3389-99.

[56] A.G. Robling, D.B. Burr, C.H. Turner, Partitioning a daily mechanical stimulus into discrete loading bouts improves the osteogenic response to loading, J Bone Miner Res 15(8) (2000) 1596-602.

[57] S. Srinivasan, D.A. Weimer, S.C. Agans, S.D. Bain, T.S. Gross, Low-magnitude mechanical loading becomes osteogenic when rest is inserted between each load cycle, J Bone Miner Res 17(9) (2002) 1613-20.

[58] S. Srinivasan, S.C. Agans, K.A. King, N.Y. Moy, S.L. Poliachik, T.S. Gross, Enabling bone formation in the aged skeleton via rest-inserted mechanical loading, Bone 33(6) (2003) 946-55.

[59] C.H. Turner, Y. Takano, I. Owan, Aging changes mechanical loading thresholds for bone formation in rats, J Bone Miner Res 10(10) (1995) 1544-9.

[60] C.T. Rubin, S.D. Bain, K.J. McLeod, Suppression of the osteogenic response in the aging skeleton, Calcif Tissue Int 50(4) (1992) 306-13.

[61] L.B. Meakin, G.L. Galea, T. Sugiyama, L.E. Lanyon, J.S. Price, Age-Related Impairment of Bones' Adaptive Response to Loading in Mice Is Associated With Sex-Related Deficiencies in Osteoblasts but No Change in Osteocytes, J Bone Miner Res 29(8) (2014) 1859-1871.

[62] A.M. Parfitt, M.K. Drezner, F.H. Glorieux, J.A. Kanis, H. Malluche, P.J. Meunier, S.M. Ott, R.R. Recker, Bone histomorphometry: standardization of nomenclature, symbols, and units: report of the ASBMR Histomorphometry Nomenclature Committee, J Bone and Miner Res 2(6) (1987) 595-610.

[63] M.R. Forwood, Inducible cyclo-oxygenase (COX-2) mediates the induction of bone formation by mechanical loading in vivo, J Bone Miner Res 11(11) (1996) 1688-93.

[64] J. Li, D.B. Burr, C.H. Turner, Suppression of prostaglandin synthesis with NS-398 has different effects on endocortical and periosteal bone formation induced by mechanical loading, Calcif Tissue Int 70(4) (2002) 320-9.

[65] V. Krishnan, H.U. Bryant, O.A. MacDougald, Regulation of bone mass by Wnt signaling, J Clin Invest 116(5) (2006) 1202-1209.

[66] J.A. Robinson, M. Chatterjee-Kishore, P.J. Yaworsky, D.M. Cullen, W. Zhao, C. Li, Y. Kharode, L. Sauter, P. Babij, E.L. Brown, A.A. Hill, M.P. Akhter, M.L. Johnson, R.R. Recker, B.S. Komm, F.J. Bex, Wnt/beta-catenin signaling is a normal physiological response to mechanical loading in bone, J Biol Chem 281(42) (2006) 31720-8.

[67] L.K. Saxon, B.F. Jackson, T. Sugiyama, L.E. Lanyon, J.S. Price, Analysis of multiple bone responses to graded strains above functional levels, and to disuse, in mice in vivo show that the human Lrp5 G171V High Bone Mass mutation increases the osteogenic response to loading but that lack of Lrp5 activity reduces it, Bone 49(2) (2011) 184-93.

[68] K. Sawakami, A. Robling, N. Pitner, S. Warden, J. Li, M. Ai, M. Warman, C. Turner, Site-specific osteopenia and decreased mechanoreactivity in Lrp5-mutant mice, J Bone Miner Res, AMER SOC BONE & MINERAL RES, 2004, pp. S38-S38.

[69] D.G. Winkler, M.K. Sutherland, J.C. Geoghegan, C. Yu, T. Hayes, J.E. Skonier, D. Shpektor, M. Jonas, B.R. Kovacevich, K. Staehling- Hampton, Osteocyte control of bone formation via sclerostin, a novel BMP antagonist, EMBO J. 22(23) (2003) 6267-6276.

[70] X. Li, Y. Zhang, H. Kang, W. Liu, P. Liu, J. Zhang, S.E. Harris, D. Wu, Sclerostin binds to LRP5/6 and antagonizes canonical Wnt signaling, J. Biol. Chem. 280(20) (2005) 19883-19887.

[71] T.A. Burgers, B.O. Williams, Regulation of Wnt/β-catenin signaling within and from osteocytes, Bone 54(2) (2013) 244-249.

[72] M. Watanuki, A. Sakai, T. Sakata, H. Tsurukami, M. Miwa, Y. Uchida, K. Watanabe, K. Ikeda, T. Nakamura, Role of inducible nitric oxide synthase in skeletal adaptation to acute increases in mechanical loading, J Bone Miner Res 17(6) (2002) 1015-25.

[73] S.W. Fox, T.J. Chambers, J.W. Chow, Nitric oxide is an early mediator of the increase in bone formation by mechanical stimulation, Am J Physiol 270(6 Pt 1) (1996) E955-60.

[74] D.M. Raab-Cullen, M.A. Thiede, D.N. Petersen, D.B. Kimmel, R.R. Recker, Mechanical loading stimulates rapid changes in periosteal gene expression, Calcif Tissue Int 55(6) (1994) 473-8.

[75] S.M. Mantila Roosa, Y. Liu, C.H. Turner, Gene expression patterns in bone following mechanical loading, J Bone Miner Res 26(1) (2011) 100-112.

[76] X. Tu, J. Delgado-Calle, K.W. Condon, M. Maycas, H. Zhang, N. Carlesso, M.M. Taketo, D.B. Burr, L.I. Plotkin, T. Bellido, Osteocytes mediate the anabolic actions of canonical Wnt/β-catenin signaling in bone, Proc. Natl. Acad. Sci. USA 112(5) (2015) E478-E486.

[77] D.J. Hadjidakis, I.I. Androulakis, Bone remodeling, Ann. N. Y. Acad. Sci. 1092(1) (2006) 385-396.

[78] C.H. Kim, E. Takai, H. Zhou, D. Von Stechow, R. Müller, D.W. Dempster, X.E. Guo, Trabecular bone response to mechanical and parathyroid hormone stimulation: the role of mechanical microenvironment, J Bone Miner Res 18(12) (2003) 2116-2125.

[79] L. Qin, L.J. Raggatt, N.C. Partridge, Parathyroid hormone: a double-edged sword for bone metabolism, Trends Endocrinol Metab 15(2) (2004) 60-65.

[80] T. Sugiyama, L.K. Saxon, G. Zaman, A. Moustafa, A. Sunters, J.S. Price, L.E. Lanyon, Mechanical loading enhances the anabolic effects of intermittent parathyroid hormone (1-34) on trabecular and cortical bone in mice, Bone 43(2) (2008) 238-48.

[81] L.I. Plotkin, R.S. Weinstein, A.M. Parfitt, P.K. Roberson, S.C. Manolagas, T. Bellido, Prevention of osteocyte and osteoblast apoptosis by bisphosphonates and calcitonin, J Clin Invest 104(10) (1999) 1363-1374.

[82] T. Chambers, C. Magnus, Calcitonin alters behaviour of isolated osteoclasts, J. Pathol. 136(1) (1982) 27-39.

[83] C.A. O'Brien, D. Jia, L.I. Plotkin, T. Bellido, C.C. Powers, S.A. Stewart, S.C. Manolagas, R.S. Weinstein, Glucocorticoids act directly on osteoblasts and osteocytes to induce their apoptosis and reduce bone formation and strength, Endocrinology 145(4) (2004) 1835-1841.

[84] E. Canalis, G. Mazziotti, A. Giustina, J.P. Bilezikian, Glucocorticoid-induced osteoporosis: pathophysiology and therapy, Osteoporosis International 18(10) (2007) 1319-1328.

[85] R.S. Weinstein, R.L. Jilka, A.M. Parfitt, S.C. Manolagas, Inhibition of osteoblastogenesis and promotion of apoptosis of osteoblasts and osteocytes by glucocorticoids. Potential mechanisms of their deleterious effects on bone, J Clin Invest 102(2) (1998) 274.

[86] E. Spencer, C. Liu, E. Si, G. Howard, In vivo actions of insulin-like growth factor-I (IGF-I) on bone formation and resorption in rats, Bone 12(1) (1991) 21-26.

[87] J.K. Yeh, J.F. Aloia, M. Chen, N. Ling, H. Koo, W.J. Millard, Effect of growth hormone administration and treadmill exercise on serum and skeletal IGF-I in rats, Am J Physiol Endocrinol Metab 266(1) (1994) E129-E135.

[88] T. Kameda, H. Mano, T. Yuasa, Y. Mori, K. Miyazawa, M. Shiokawa, Y. Nakamaru, E. Hiroi, K. Hiura, A. Kameda, Estrogen inhibits bone resorption by directly inducing apoptosis of the bone-resorbing osteoclasts, The Journal of experimental medicine 186(4) (1997) 489-495.

[89] L. Montes, N. Le Roy, M. Perret, V. De Buffrenil, J. Castanet, J. Cubo, Relationships between bone growth rate, body mass and resting metabolic rate in growing amniotes: a phylogenetic approach, Biol J Linnean Soc 92(1) (2007) 63-76.

[90] R.W. Blob, A.A. Biewener, In vivo locomotor strain in the hindlimb bones of Alligator mississippiensis and Iguana iguana: implications for the evolution of limb bone safety factor and non-sprawling limb posture, J Exp Biol 202(9) (1999) 1023-1046.

[91] A. Casinos, J. Cubo, Avian long bones, flight and bipedalism, Comp Biochem Physiol A Mol Integr Physiol 131(1) (2001) 159-167.

[92] J. Cubo, A. Casinos, Incidence and mechanical significance of pneumatization in the long bones of birds, Zoological Journal of the Linnean Society 130(4) (2000) 499-510.

[93] E.R. Dumont, Bone density and the lightweight skeletons of birds, Proceedings of the Royal Society of London B: Biological Sciences (2010) rspb20100117.

[94] J. Currey, The many adaptations of bone, J Biomech 36(10) (2003) 1487-1495.

[95] J. Currey, The evolution of the mechanical properties of amniote bone, J Biomech 20(11) (1987) 1035-1044.

[96] K. Simkiss, Calcium metabolism and avian reproduction, Biological Reviews 36(3) (1961) 321-359.

[97] C. Dacke, S. Arkle, D. Cook, I. Wormstone, S. Jones, M. Zaidi, Z. Bascal, Medullary bone and avian calcium regulation, Journal of Experimental Biology 184(1) (1993) 63-88.

[98] S.C. Miller, B.M. Bowman, Medullary bone osteogenesis following estrogen administration to mature male Japanese quail, Developmental biology 87(1) (1981) 52-63.

[99] J. Pritchard, A. Ruzicka, Comparison of fracture repair in the frog, lizard and rat, Journal of anatomy 84(Pt 3) (1950) 236.

[100] M.P. Akhter, D.M. Cullen, E.A. Pedersen, D.B. Kimmel, R.R. Recker, Bone response to in vivo mechanical loading in two breeds of mice, Calcif Tissue Int 63(5) (1998) 442-9.

[101] R.P. Main, A.A. Biewener, Skeletal strain patterns and growth in the emu hindlimb during ontogeny, J Exp Biol 210(Pt 15) (2007) 2676-90.

[102] R.W. Blob, A.A. Biewener, In vivo locomotor strain in the hindlimb bones of Alligator mississippiensis and Iguana iguana: implications for the evolution of limb bone safety factor and non-sprawling limb posture, Journal of Experimental Biology 202(9) (1999) 1023-1046.

[103] A. Biewener, K. Dial, In vivo strain in the humerus of pigeons (Columba livia) during flight, Journal of Morphology 225(1) (1995) 61-75.

[104] M.T. Butcher, B.J. White, N.B. Hudzik, W.C. Gosnell, J.H. Parrish, R.W. Blob, In vivo strains in the femur of the Virginia opossum (Didelphis virginiana) during terrestrial locomotion: testing hypotheses of evolutionary shifts in mammalian bone loading and design, The Journal of experimental biology 214(15) (2011) 2631-2640.

[105] M.T. Butcher, N.R. Espinoza, S.R. Cirilo, R.W. Blob, In vivo strains in the femur of river cooter turtles (Pseudemys concinna) during terrestrial locomotion: tests of force-platform models of loading mechanics, Journal of Experimental Biology 211(15) (2008) 2397-2407.

[106] A. Biewener, In vivo measurement of bone strain and tendon force, Biomechanics–Structures and Systems: A Practical Approach (1992) 123-147.

[107] D. Carter, W. Harris, R. Vasu, W. Caler, The mechanical and biological response of cortical bone to in vivo strain histories, Mechanical properties of bone 45 (1981) 81-92.

[108] D.E. Lieberman, J.D. Polk, B. Demes, Predicting long bone loading from cross-sectional geometry, American Journal of Physical Anthropology 123(2) (2004) 156-171.

[109] D.R. Carter, Anisotropic analysis of strain rosette information from cortical bone, Journal of biomechanics 11(4) (1978) 199-202.

[110] R.P. Main, Ontogenetic relationships between in vivo strain environment, bone histomorphometry and growth in the goat radius, Journal of anatomy 210(3) (2007) 272-293.

[111] R.P. Main, A.A. Biewener, Ontogenetic patterns of limb loading, in vivo bone strains and growth in the goat radius, Journal of Experimental Biology 207(15) (2004) 2577-2588.

[112] M.T. Butcher, R.W. Blob, Mechanics of limb bone loading during terrestrial locomotion in river cooter turtles (Pseudemys concinna), J Exp Biol 211(8) (2008) 1187-1202.

[113] M.T. Butcher, B.J. White, N.B. Hudzik, W.C. Gosnell, J.H. Parrish, R.W. Blob, In vivo strains in the femur of the Virginia opossum (Didelphis virginiana) during terrestrial locomotion: testing hypotheses of evolutionary shifts in mammalian bone loading and design, J Exp Biol 214(15) (2011) 2631-2640.

[114] K.A. Metzger, W.J. Daniel, C.F. Ross, Comparison of beam theory and finite-element analysis with in vivo bone strain data from the alligator cranium, The Anatomical Record Part A: Discoveries in Molecular, Cellular, and Evolutionary Biology 283(2) (2005) 331-348.

[115] O. Panagiotopoulou, S. Wilshin, E. Rayfield, S. Shefelbine, J. Hutchinson, What makes an accurate and reliable subject-specific finite element model? A case study of an elephant femur, Journal of The Royal Society Interface 9(67) (2012) 351-361.

[116] C.H. Turner, Three rules for bone adaptation to mechanical stimuli, Bone 23(5) (1998) 399-407.

[117] L.E. Lanyon, Control of bone architecture by functional load bearing, Journal of Bone and Mineral Research 7(S2) (1992).

[118] M. Pead, T. Skerry, L. Lanyon, JBMR Anniversary Classic, JOURNAL OF BONE AND MINERAL RESEARCH 3(6) (1988).

[119] T. Sugiyama, J.S. Price, L.E. Lanyon, Functional adaptation to mechanical loading in both cortical and cancellous bone is controlled locally and is confined to the loaded bones, Bone 46(2) (2010) 314-321.

[120] C.T. Rubin, K.J. McLeod, S.D. Bain, Functional strains and cortical bone adaptation: epigenetic assurance of skeletal integrity, Journal of Biomechanics 23 (1990) 4351-4954.

[121] A.L. Huddleston, D. Rockwell, D.N. Kulund, R.B. Harrison, Bone mass in lifetime tennis athletes, Jama 244(10) (1980) 1107-1109.

[122] H. Haapasalo, P. Kannus, H. Sievänen, M. Pasanen, K. Uusi-Rasi, A. Heinonen, P. Oja, I. Vuori, Effect of long-term unilateral activity on bone mineral density of female junior tennis players, Journal of Bone and Mineral Research 13(2) (1998) 310-319.

[123] S.J. Warden, E.D. Bogenschutz, H.D. Smith, A.R. Gutierrez, Throwing induces substantial torsional adaptation within the midshaft humerus of male baseball players, Bone 45(5) (2009) 931-941.

[124] P.C. Rambaut, R.S. Johnston, Prolonged weightlessness and calcium loss in man, Acta astronautica 6(9) (1979) 1113-1122.

[125] J.D. Sibonga, H.J. Evans, H. Sung, E. Spector, T. Lang, V. Oganov, A. Bakulin, L. Shackelford, A. LeBlanc, Recovery of spaceflight-induced bone loss: bone mineral density after long-duration missions as fitted with an exponential function, Bone 41(6) (2007) 973-978.

[126] C.H. Turner, M.R. Forwood, J.Y. Rho, T. Yoshikawa, Mechanical loading thresholds for lamellar and woven bone formation, J Bone Miner Res 9(1) (1994) 87-97.

[127] M.R. Forwood, C.H. Turner, Skeletal adaptations to mechanical usage: results from tibial loading studies in rats, Bone 17(4 Suppl) (1995) 197S-205S.

[128] K.C. Lee, A. Maxwell, L.E. Lanyon, Validation of a technique for studying functional adaptation of the mouse ulna in response to mechanical loading, Bone 31(3) (2002) 407-12.

[129] D. Cullen, R. Smith, M. Akhter, Bone-loading response varies with strain magnitude and cycle number, Journal of Applied Physiology 91(5) (2001) 1971-1976.

[130] P. Sztefek, M. Vanleene, R. Olsson, R. Collinson, A.A. Pitsillides, S. Shefelbine, Using digital image correlation to determine bone surface strains during loading and after adaptation of the mouse tibia, J Biomech 43(4) (2010) 599-605.

[131] A. Moustafa, T. Sugiyama, J. Prasad, G. Zaman, T.S. Gross, L.E. Lanyon, J.S. Price, Mechanical loading-related changes in osteocyte sclerostin expression in mice are more closely associated with the subsequent osteogenic response than the peak strains engendered, Osteoporos Int 23(4) (2012) 1225-34.

[132] B.M. Willie, A.I. Birkhold, H. Razi, T. Thiele, M. Aido, B. Kruck, A. Schill, S. Checa, R.P. Main, G.N. Duda, Diminished response to in vivo mechanical loading in trabecular and not cortical bone in adulthood of female C57Bl/6 mice coincides with a reduction in deformation to load, Bone 55(2) (2013) 335-46.

[133] T.K. Patel, M.D. Brodt, M.J. Silva, Experimental and finite element analysis of strains induced by axial tibial compression in young-adult and old female C57Bl/6 mice, J Biomech 47(2) (2014) 451-7.

[134] E.S. Orwoll, J.K. Belknap, R.F. Klein, Gender specificity in the genetic determinants of peak bone mass, Journal of Bone and Mineral Research 16(11) (2001) 1962-1971.

[135] B.T. Kim, L. Mosekilde, Y. Duan, X.Z. Zhang, L. Tornvig, J.S. Thomsen, E. Seeman, The structural and hormonal basis of sex differences in peak appendicular bone strength in rats, Journal of Bone and Mineral Research 18(1) (2003) 150-155.

[136] P. Zioupos, J. Currey, Changes in the stiffness, strength, and toughness of human cortical bone with age, Bone 22(1) (1998) 57-66.

[137] X. Wang, X. Shen, X. Li, C.M. Agrawal, Age-related changes in the collagen network and toughness of bone, Bone 31(1) (2002) 1-7.

[138] L.B. Meakin, T. Sugiyama, G.L. Galea, W.J. Browne, L.E. Lanyon, J.S. Price, Male mice housed in groups engage in frequent fighting and show a lower response to additional bone loading than females or individually housed males that do not fight, Bone 54(1) (2013) 113-117.

[139] R. Fleming, C. Whitehead, D. Alvey, N. Gregory, L. Wilkins, Bone structure and breaking strength in laying hens housed in different husbandry systems, British poultry science 35(5) (1994) 651-662.

[140] C. Rubin, T. Gross, Y.X. Qin, S. Fritton, F. Guilak, K. McLeod, Differentiation of the bone-tissue remodeling response to axial and torsional loading in the turkey ulna, J Bone Joint Surg Am 78(10) (1996) 1523-33.

[141] J.E. Bertram, S.M. Swartz, The 'law of bone transformation': a case of crying Wolff?, Biol Rev Camb Philos Soc 66(3) (1991) 245-73.

[142] R.P. Main, A.A. Biewener, Skeletal strain patterns and growth in the emu hindlimb during ontogeny, Journal of Experimental Biology 210(Pt 15) (2007) 2676-90.

[143] A.A. Biewener, C.R. Taylor, Bone strain: a determinant of gait and speed?, Journal of Experimental Biology 123(1) (1986) 383-400.

[144] M.J. Silva, M.D. Brodt, W.J. Hucker, Finite element analysis of the mouse tibia: Estimating endocortical strain during three-point bending in SAMP6 osteoporotic mice, Anat Rec A Discov Mol Cell Evol Biol 283(2) (2005) 380-390.

[145] Q. Fang, D.A. Boas, Tetrahedral mesh generation from volumetric binary and grayscale images, Biomedical Imaging: From Nano to Macro, 2009. ISBI'09. IEEE International Symposium on, Ieee, 2009, pp. 1142-1145.

[146] S.K. Easley, M.G. Jekir, A.J. Burghardt, M. Li, T.M. Keaveny, Contribution of the intra-specimen variations in tissue mineralization to PTH-and raloxifene-induced changes in stiffness of rat vertebrae, Bone 46(4) (2010) 1162-1169.

[147] J. Bertram, Y. Polevoy, D. Cullinane, Mechanics of avian fibrous periosteum: tensile and adhesion properties during growth, Bone 22(6) (1998) 669-675.

[148] A. Matson, N. Konow, S. Miller, P.P. Konow, T.J. Roberts, Tendon material properties vary and are interdependent among turkey hindlimb muscles, Journal of Experimental Biology 215(20) (2012) 3552-3558.

[149] K.A. Verner, M. Lehner, L.P. Lamas, R.P. Main, Experimental tests of planar strain theory for predicting bone cross-sectional longitudinal and shear strains, Journal of Experimental Biology 219(19) (2016) 3082-3090.

[150] A.A. Biewener, Biomechanics-- structures and systems: a practical approach, IRL Press at Oxford University Press1992.

[151] D.B. Burr, C. Milgrom, D. Fyhrie, M. Forwood, M. Nyska, A. Finestone, S. Hoshaw, E. Saiag, A. Simkin, In vivo measurement of human tibial strains during vigorous activity, Bone 18(5) (1996) 405-410.

[152] J. Prasad, B.P. Wiater, S.E. Nork, S.D. Bain, T.S. Gross, Characterizing gait induced normal strains in a murine tibia cortical bone defect model, Journal of biomechanics 43(14) (2010) 2765-2770.

[153] A.A. Biewener, J.E. Bertram, Structural response of growing bone to exercise and disuse, Journal of Applied Physiology 76(2) (1994) 946-955.

[154] L. Rowland, J.L. Fry, R. Christmas, A. O'Steen, R. Harms, Differences in tibia strength and bone ash among strains of layers, Poultry Science 51(5) (1972) 1612-1615.

[155] N. Rath, G. Huff, W. Huff, J. Balog, Factors regulating bone maturity and strength in poultry, Poultry Science 79(7) (2000) 1024-1032.

[156] M.R. Forwood, M.B. Bennett, A.R. Blowers, R.L. Nadorfi, Modification of the in vivo four-point loading model for studying mechanically induced bone adaptation, Bone 23(3) (1998) 307-10.

[157] T.S. Gross, S. Srinivasan, C.C. Liu, T.L. Clemens, S.D. Bain, Noninvasive loading of the murine tibia: an in vivo model for the study of mechanotransduction, J Bone Miner Res 17(3) (2002) 493-501.

[158] L.E. Lanyon, C.T. Rubin, Static vs dynamic loads as an influence on bone remodelling, J Biomech 17(12) (1984) 897-905.

[159] M.E. Lynch, R.P. Main, Q. Xu, T.L. Schmicker, M.B. Schaffler, T.M. Wright, M.C. van der Meulen, Tibial compression is anabolic in the adult mouse skeleton despite reduced responsiveness with aging, Bone 49(3) (2011) 439-46.

[160] K.C. Lee, H. Jessop, R. Suswillo, G. Zaman, L.E. Lanyon, The adaptive response of bone to mechanical loading in female transgenic mice is deficient in the absence of oestrogen receptor-alpha and -beta, J Endocrinol 182(2) (2004) 193-201.

[161] A. Morse, M. McDonald, N. Kelly, K. Melville, A. Schindeler, I. Kramer, M. Kneissel, M. van der Meulen, D. Little, Mechanical Load Increases in Bone Formation Via a Sclerostin-Independent Pathway, J Bone Miner Res (2014).

[162] S. Harris, J. Gluhak-Heinrich, M. Harris, W. Yang, L. Bonewald, D. Riha, P. Rowe, A. Robling, C. Turner, J. Feng, M. McKee, D. Nicollela, DMP1 and MEPE expression are elevated in osteocytes after mechanical loading in vivo: Theoretical role in controlling mineral quality in the perilacunar matrix, Journal of Musculoskeletal Neuronal Interactions 7(4) (2007) 313-5.

[163] R.L. Jilka, The Relevance of Mouse Models for Investigating Age-Related Bone Loss in Humans, The Journals of Gerontology: Series A 68(10) (2017) 1209-1217.

[164] A.A. Biewener, Safety factors in bone strength, Calcified Tissue International 53 (1993) S68-S74.

[165] H. Yang, R.E. Embry, R.P. Main, Effects of Loading Duration and Short Rest Insertion on Cancellous and Cortical Bone Adaptation in the Mouse Tibia, PloS one 12(1) (2017) e0169519.

[166] D.W. Dempster, J.E. Compston, M.K. Drezner, F.H. Glorieux, J.A. Kanis, H. Malluche, P.J. Meunier, S.M. Ott, R.R. Recker, A.M. Parfitt, Standardized nomenclature, symbols, and units for bone histomorphometry: a 2012 update of the report of the ASBMR Histomorphometry Nomenclature Committee, Journal of Bone and Mineral Research 28(1) (2013) 2-17.

[167] C.A. Gregory, W. Grady Gunn, A. Peister, D.J. Prockop, An Alizarin red-based assay of mineralization by adherent cells in culture: comparison with cetylpyridinium chloride extraction, Analytical Biochemistry 329(1) (2004) 77-84.

[168] H.M. Frost, S.C.C. Department of Orthopaedic Surgery, Pueblo, CO 81004, Skeletal structural adaptations to mechanical usage (SATMU): 1. Redefining Wolff's Law: The bone modeling problem, The Anatomical Record 226(4) (2017) 403-413.

[169] A.G. Robling, A.B. Castillo, C.H. Turner, Biomechanical and molecular regulation of bone remodeling, Annu Rev Biomed Eng 8 (2006) 455-98.

[170] M.C.H.v.d. Meulen, mcv3@cornell.edu, C.U. Sibley School of Mechanical and Aerospace Engineering, Ithaca, NY, USA, R.D. Biomechanics and Biomaterials Section, Hospital for Special Surgery, New York, NY, USA, K.J. Jepsen, M.S.S.o.M. Department of Orthopedics, New York, NY, USA, B. Mikić, S.C. Picker Engineering Program, Northampton, MA, USA, Understanding bone strength: size isn’t everything, Bone 29(2) (2001) 101-104.

[171] R.L. Jilka, K. Takahashi, M. Munshi, D.C. Williams, P.K. Roberson, S.C. Manolagas, Loss of estrogen upregulates osteoblastogenesis in the murine bone marrow. Evidence for autonomy from factors released during bone resorption, Journal of Clinical Investigation 101(9) (1998) 1942.

[172] J.E. Aubin, Bone stem cells, Journal of Cellular Biochemistry 72(S30–31) (1998) 73-82.

[173] N. Giuliani, M. Pedrazzoni, G. Negri, G. Passeri, M. Impicciatore, G. Girasole, Bisphosphonates Stimulate Formation of Osteoblast Precursors and Mineralized Nodules in Murine and Human Bone Marrow Cultures In Vitro and Promote Early Osteoblastogenesis in Young and Aged Mice In Vivo, Bone 22(5) (1998) 455-461.

[174] A. Peister, J.A. Mellad, B.L. Larson, B.M. Hall, L.F. Gibson, D.J. Prockop, Adult stem cells from bone marrow (MSCs) isolated from different strains of inbred mice vary in surface epitopes, rates of proliferation, and differentiation potential, Blood 103(5) (2004) 1662-1668.

[175] D.W. Dempster, F. Cosman, M. Parisien, V. Shen, R. Lindsay, Anabolic actions of parathyroid hormone on bone, Endocrine reviews 14(6) (1993) 690-709.

[176] L.G. Raisz, Physiology and pathophysiology of bone remodeling, Clinical chemistry 45(8) (1999) 1353-1358.

[177] R.L. Duncan, C.H. Turner, Mechanotransduction and the functional response of bone to mechanical strain, Calcif Tissue Int 57(5) (1995) 344-58.

[178] E.F. Eriksen, Cellular mechanisms of bone remodeling, Rev Endocr Metab Disord 11(4) (2010) 219-227.

[179] S. Fukumoto, T.J. Martin, Bone as an endocrine organ, Trends Endocrinol Metab 20(5) (2009) 230-236.

[180] M. Kassem, W. Blum, J. Ristelli, L. Mosekilde, E. Eriksen, Growth hormone stimulates proliferation and differentiation of normal human osteoblast-like cells in vitro, Calcified Tissue International 52(3) (1993) 222-226.

[181] E. Canalis, M. Centrella, T. McCarthy, Effects of basic fibroblast growth factor on bone formation in vitro, Journal of Clinical Investigation 81(5) (1988) 1572.

[182] E. Canalis, J. Lian, Effects of bone associated growth factors on DNA, collagen and osteocalcin synthesis in cultured fetal rat calvariae, Bone 9(4) (1988) 243-246.

[183] H. Stracke, A. Schulz, D. Moeller, S. Rossol, H. Schatz, Effect of growth hormone on osteoblasts and demonstration of somatomedin-C/IGF I in bone organ culture, Acta endocrinologica 107(1) (1984) 16-24.

[184] G.A. Howard, B.L. Bottemiller, R.T. Turner, J.I. Rader, D.J. Baylink, Parathyroid hormone stimulates bone formation and resorption in organ culture: evidence for a coupling mechanism, Proceedings of the National Academy of Sciences 78(5) (1981) 3204-3208.

[185] A.H. Tashjian, J.E. Tice, K. Sides, Biological activities of prostaglandin analogues and metabolites on bone in organ culture, Nature 266(5603) (1977) 645-647.

[186] M.M. Saunders, L.A. Simmerman, G.L. Reed, N.A. Sharkey, A.F. Taylor, Biomimetic bone mechanotransduction modeling in neonatal rat femur organ cultures: structural verification of proof of concept, Biomech Model Mechanobiol 9(5) (2010) 539-550.

[187] S.L. Dallas, G. Zaman, M.J. Pead, L.E. Lanyon, Early strain-related changes in cultured embryonic chick tibiotarsi parallel those associated with adaptive modeling in vivo, Journal of Bone and Mineral Research 8(3) (1993) 251-259.

[188] G. Zaman, S.L. Dallas, L.E. Lanyon, Cultured embryonic bone shafts show osteogenic responses to mechanical loading, Calcified tissue international 51(2) (1992) 132-136.

[189] S.C. Rawlinson, A.J. El-Haj, S.L. Minter, I.A. Tavares, A. Bennett, L.E. Lanyon, Loading-related increases in prostaglandin production in cores of adult canine cancellous bone in vitro: A role for prostacyclin in adaptive bone remodeling?, Journal of bone and mineral research 6(12) (1991) 1345-1351.

[190] M.E. Chan, X.L. Lu, B. Huo, A.D. Baik, V. Chiang, R.E. Guldberg, H.H. Lu, X.E. Guo, A Trabecular Bone Explant Model of Osteocyte–Osteoblast Co-Culture for Bone Mechanobiology, Cellular and Molecular Bioengineering 2(3) (2009) 405-415.

[191] V. Mann, C. Huber, G. Kogianni, D. Jones, B. Noble, The influence of mechanical stimulation on osteocyte apoptosis and bone viability in human trabecular bone, Journal of musculoskeletal & neuronal interactions 6(4) (2006) 408.

[192] C. Davies, D. Jones, M. Stoddart, K. Koller, E. Smith, C. Archer, R. Richards, Mechanically loaded ex vivo bone culture system 'Zetos': systems and culture preparation, Eur Cell Mater 11 (2006) 57-75.

[193] E. Takai, R.L. Mauck, C.T. Hung, X.E. Guo, Osteocyte viability and regulation of osteoblast function in a 3D trabecular bone explant under dynamic hydrostatic pressure, Journal of bone and mineral research 19(9) (2004) 1403-1410.

[194] A.J.E. Haj, S.L. Minter, S.C. Rawlinson, R. Suswillo, L.E. Lanyon, Cellular responses to mechanical loading in vitro, Journal of Bone and Mineral Research 5(9) (1990) 923-932.

[195] N. Kelly, J. Schimenti, F.P. Ross, M. Van Der Meulen, RNA Seq-based Gene Expression in Mouse Cortical and Cancellous Bone, J Bone Miner Res, 2014, pp. S459-S459.

[196] C. Rubin, A. Turner, C. Mallinckrodt, C. Jerome, K. McLeod, S. Bain, Mechanical strain, induced noninvasively in the high-frequency domain, is anabolic to cancellous bone, but not cortical bone, Bone 30(3) (2002) 445-452.

[197] Y.H. Gao, M. Yamaguchi, Anabolic effect of daidzein on cortical bone in tissue culture: comparison with genistein effect, Molecular and cellular biochemistry 194(1) (1999) 93-98.

[198] S.Y. Wong, C. Dunstan, R. Evans, E. Hills, The determination of bone viability: a histochemical method for identification of lactate dehydrogenase activity in osteocytes in fresh calcified and decalcified sections of human bone, Pathology 14(4) (1982) 439-442.

[199] S. Wong, J. Kariks, R. Evans, C. Dunstan, E. Hills, The effect of age on bone composition and viability in the femoral head, JBJS 67(2) (1985) 274-283.

[200] R. Rumney, A. Sunters, G. Reilly, A. Gartland, Application of multiple forms of mechanical loading to human osteoblasts reveals increased ATP release in response to fluid flow in 3D cultures and differential regulation of immediate early genes, Journal of biomechanics 45(3) (2012) 549-554.

[201] A. Sittichockechaiwut, A.M. Scutt, A.J. Ryan, L.F. Bonewald, G.C. Reilly, Use of rapidly mineralising osteoblasts and short periods of mechanical loading to accelerate matrix maturation in 3D scaffolds, Bone 44(5) (2009) 822-829.

[202] Z. Kong, J. Li, Q. Zhao, Z. Zhou, X. Yuan, D. Yang, X. Chen, Dynamic compression promotes proliferation and neovascular networks of endothelial progenitor cells in demineralized bone matrix scaffold seed, Journal of Applied Physiology 113(4) (2012) 619-626.

[203] C.E. Hoffler, K.D. Hankenson, J.D. Miller, S.K. Bilkhu, S.A. Goldstein, Novel explant model to study mechanotransduction and cell–cell communication, Journal of orthopaedic research 24(8) (2006) 1687-1698.

[204] C. Price, X. Zhou, W. Li, L. Wang, Real-time measurement of solute transport within the lacunar-canalicular system of mechanically loaded bone: Direct evidence for load- induced fluid flow, Journal of Bone and Mineral Research 26(2) (2017) 277-285.

[205] C. Ciani, D. Sharma, S.B. Doty, S.P. Fritton, Ovariectomy enhances mechanical load-induced solute transport around osteocytes in rat cancellous bone, Bone 59(Supplement C) (2014) 229-234.

[206] P. Mc Donnell, P. Mc Hugh, D. O'mahoney, Vertebral osteoporosis and trabecular bone quality, Annals of biomedical engineering 35(2) (2007) 170-189.

[207] E.F. Eriksen, S.F. Hodgson, R. Eastell, B.L. RIGGS, S.L. Cedel, W.M. O'Fallon, Cancellous bone remodeling in type I (postmenopausal) osteoporosis: quantitative assessment of rates of formation, resorption, and bone loss at tissue and cellular levels, Journal of Bone and Mineral Research 5(4) (1990) 311-319.

[208] B. Li, R.M. Aspden, Composition and mechanical properties of cancellous bone from the femoral head of patients with osteoporosis or osteoarthritis, Journal of Bone and Mineral Research 12(4) (1997) 641-651.

[209] W. Xing, D. Baylink, C. Kesavan, Y. Hu, S. Kapoor, R.B. Chadwick, S. Mohan, Global gene expression analysis in the bones reveals involvement of several novel genes and pathways in mediating an anabolic response of mechanical loading in mice, Journal of cellular biochemistry 96(5) (2005) 1049-1060.